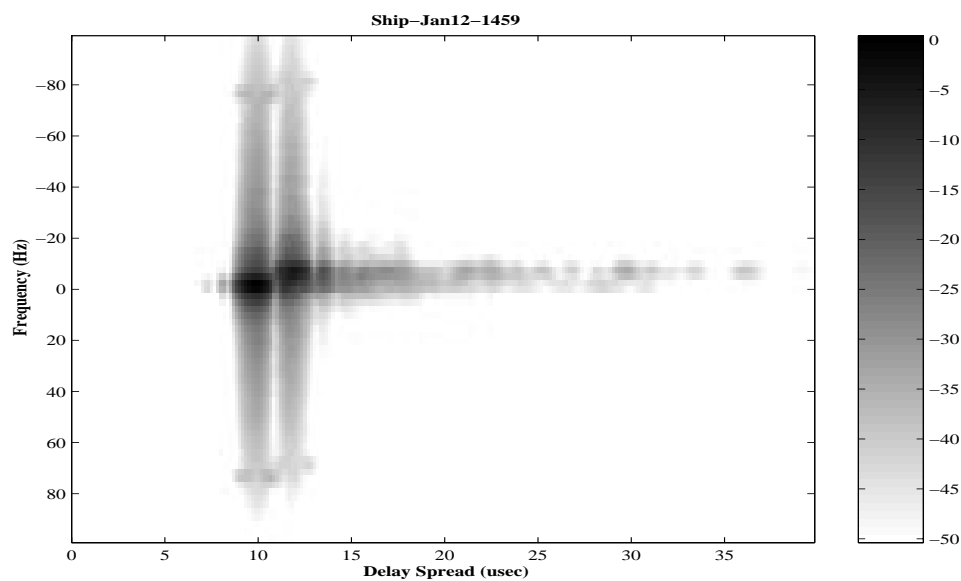


RF Channel Characterization & Estimation: Sequence-Based Methods (Phase I)



Jeffery C. Allen Michael Reuter

Richard C. North

Naval Command, Control & Ocean Surveillance Center
San Diego, CA

April 16, 1998

Contents

Preface	iv
1 Channel Estimation: Background	1
1.1 Document Outline	2
1.2 Recent Channel Estimation Literature	4
1.3 Notation	6
2 Time-Varying Channels: Baseband PMFS	8
2.1 Channel Functions	10
2.2 Phase-Modulation Fading Simulator	12
2.3 Covariance Functions	13
2.4 Delay & Doppler Spread	16
2.5 Baseband PMFS	19
2.6 Digital Baseband PMFS	20
2.7 Digital Channel Functions	22
2.8 PMFS Simulation Issues	24
3 Time-Varying Channels: Baseband QMFS	28
3.1 Quadrature-Modulation Fading Simulator (QMFS)	28
3.2 Channel Functions	29
3.3 Covariance Functions	29
3.4 Digital Baseband QMFS	31
3.5 Digital Channel Functions	33
3.6 QMFS Simulation Issues	34
4 A Surface Scatter Channel	38
4.1 Additive Channel Noise	40

4.2	Free-Space Path Loss	41
4.3	The Flat-Terrain Path-Loss Model	42
4.4	Multiplicative Noise	45
4.5	Ship-to-Shore	47
4.6	Propagation Issues: Ship-to-Shore	50
5	Channel Estimation: Sequence Methods	54
5.1	PN Processing	56
5.2	Gauss-Markov Processing	65
5.3	Minimum-Variance Processing	74
5.4	Review of the Sequence Literature	77
6	Channel Estimation: System Identification	81
6.1	The Discrete Channel	82
6.2	A Filterbank Approach	83
6.3	Residual Carrier Recovery	84
6.4	Implementation: Filterbanks & Carrier Recovery	86
6.5	Linking the Filter to the Channel	87
6.6	Setting the Adaptive Filter Parameters	88
7	Naval Communication Channel Datasets	91
7.1	Multipath Emulated Data Files	91
7.2	HMMWV Data Files	98
7.3	Navy Ship Data Files	104
8	Emulated & Over-the-Air Channel Estimates	110
8.1	Spurious-Free Dynamic Range (SFDR)	112
8.2	Distortion of the Raised Cosine	117
8.3	TAS4500: SFDR & Pulse Distortion	119
8.4	TAS4500_13: Amplitude Calibration	122
8.5	TAS4500_11: Amplitude Calibration	125
8.6	TAS4500_18: Amplitude Calibration	128
8.7	TAS4500_19: Time-Variant Channel	132
8.8	TAS4500_24: Time-Variant Channel	134
8.9	HMMWV	136
8.10	Ship-to-Shore	139

9	Future Directions	142
A	Generalized Random Processes	154
B	Baseband Error Bounds	156
C	Gauss-Markov Theorems	160
D	Receiver Noise Computations	162

Preface

The design of reliable communications requires that modulation and demodulation techniques compensate for the deleterious effects of the communication channel. Thus, one of the most important steps in the design of a reliable communication system is a careful characterization of the communication channel.

This document describes a general digital baseband channel model and its realization with respect to the UHF line-of-sight communication channel. It then develops several channel estimation techniques useful in estimating the parameters of the channel model. Each of these channel estimation models is analyzed and applied to both emulated laboratory data and to over-the-air data. The over-the-air data includes measurements from a mobile US Marine Corps HMMWV operating in an urban environment and a mobile US Naval ship (USS Princeton) operating in the littoral environment. All data was collected at San Diego, California during January and February of 1998 using 1 Mbps in the 225-400 MHz military UHF band.

Channel estimation by an adaptive filter technique includes a demodulation scheme robust to multipath fading and performed exceptionally well in all scenarios. In contrast, conventional baseband channel estimation techniques — that require a separate and blind demodulator — were sometimes stymied by multipath.

This document illustrates the performance of these channel estimators by comparing the estimated power delay profiles, delay-spread functions, and scattering functions for numerous data sets. The results are that the mobile HMMWV operating in an urban environment can have a large number of multiple propagation paths typically with delay spreads less than 7 microseconds but with the possibility of a few paths with delay spreads up to 17 microseconds. Fading is typically rapid (20-30 Hz). The mobile ship

operating off the coast typically has a single resolvable path with very slow fading (less than 5 Hz). However, both the number of paths and the fade rate increased when the ship was in transit in and around the city and its bridges.

This research was sponsored by Drs. Neil Gerr, Rabinder Madan, and Sherman Gee from the Office of Naval Research, Code 313.

Chapter 1

Channel Estimation: Background

The problem is to estimate an RF channel from a transmitted sequence known to the user. Because of the number of details and assumptions that constitute the radio setup and the processing, this chapter provides the reader with a “top-down” orientation to this problem.

Figure 1.1 shows a schematic of the transmitter, channel, and receiver. In this case, a pseudorandom (PN) sequence is transmitted — essentially a Bernoulli or $\{0, 1\}$ “coin flipping” sequence. It is encoded into a (complex-valued) sequence. This sequence modulates a pulse train — typical pulses are the square-root raised cosine. After D/A, this analog signal mixed to RF band and amplified for transmission through the RF environment. The RF environment is usually considered to be a linear but time-varying filter. For example, a ship-to-shore link may have the signal arriving along a direct line-of-sight (LOS) path and a delayed version arriving from the path reflecting off the time-varying surface of the water. At the receiver, Figure 1.1 shows this process is reversed.

The problem is that received sequence may not match the transmitted sequence. Although distortion and timing errors are present in the radio, we assume the major source of error is due to the channel. For example, the ship-to-shore link will have the transmitted sequence and a delayed copy present — both corrupted by additive and multiplicative channel noise. If the channel were known, then some of its effects could be canceled and signal error reduced. Accordingly, our focus is on the channel. Our goal is to

capture channel effects in selected mathematical models, to offer researchers a collection of real-world channel measurements, and to make side-by-side comparisons of selected channel estimation schemes.

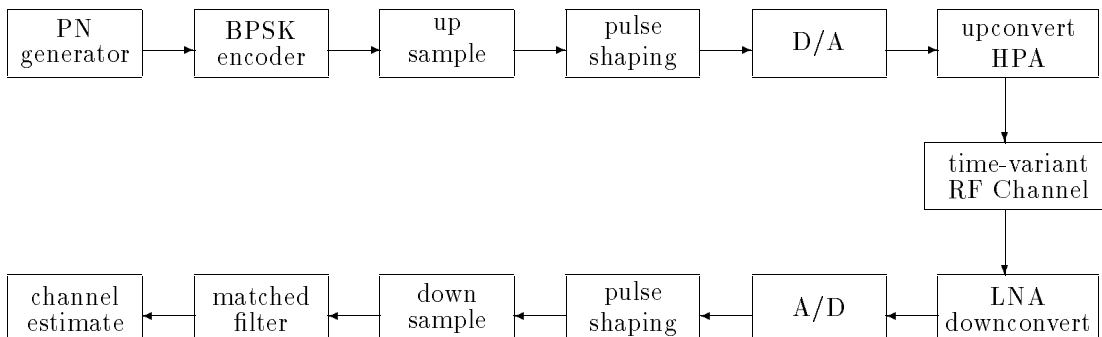


Figure 1.1: Block diagram for estimating the channel using PN sequences. PN=pseudonoise; D/A=digital-to-analog; HPA=high-power amplifier; LNA=low-noise amplifier.

1.1 Document Outline

We start with two common channel models. Chapters 2 and 3 review the *Phase-Modulation Fading Simulator* (PMFS) and the *Quadrature-Modulation Fading Simulator* (QMFS), respectively. The PMFS is an excellent analytical model that provides a slick treatment of the mathematical framework. The reader should be pleasantly surprised by the ease which channel concepts are handled by this model. The developments readily extend to the QMFS and also permit a rapid treatment of that model. However, PMFS requires additional “tricks” to overcome its ergodic properties. Thus, we use the QMFS to handle the actual simulations in this report.

Because our focus is on the channel, both chapters work from their respective baseband models. We make explicit the baseband assumptions and offer error bounds when practical. Baseband assumptions require that the modulation — as implemented in the receiver and transmitter — be linear. This linearity depends mostly on the quality and operation of the transmitter’s

high-power amplifier. For this reason, care was taken that the high-quality amplifier (See Chapter 7) used to make the real-world channel measurements were operated in their linear region. Recent work has shown how to design transmission sequences which mitigate amplifier non-linearities [21], [23], [22]. This passband modeling makes an excellent starting point for future developments.

Both the PMFS and the QMFS are general channels models that require some work to specialize to a specific transmission and receiver setup. Chapter 4 undertakes this task and develops a ship-to-shore QMFS using the standard two-path model. Propagation losses for this two-path model are compared against a sophisticated propagation code [70]. Although both models generally agree in regions away from the ground, surface wave and terrain cause major differences. Because these phenomena are not in the path model, proper use of such path models should be limited to setting the time delays and general power levels for the paths in the QFMS.

Chapter 5 makes the first comparisons between selected channel estimators. Our benchmark channel estimator is the matched filter. In this case, it simply convolves the PN sequence with its reversion to estimate the channel. This simple and robust estimator serves as a handy yardstick to assess more sophisticated schemes. The Gauss-Markov estimator is commonly used but does not account for the power level of uncorrelated noise. The Minimum-Variance or Wiener filter does handle such noise — provided the SNR is known. Recent work on regularization by Hansen [32], [33], [34] — specifically his theory of L -curves — makes this estimator practical. Comparisons on a variety of channels show the limitations of these methods and provide a guide for channel estimation when applied to real data.

Chapter 6 reviews a system identification approach to channel estimation. The transmitted sequence is input to an adaptive filter which is then forced to approximate the received sequence. The claim is that this adaptive filter then approximates the unknown channel. Comparisons on a variety of channels show the validity of this approach and lay the foundation for a future work for maritime channel modeling by a tapped delay line.

Chapter 7 collects measurements from laboratory emulations and on-site measurements. The laboratory emulations are valuable because they permit various calibrations and take the step from the “toy” data of simulations to the level of a controlled RF experiment. For example, a researcher developing channel estimation schemes can get a feel for model sensitivity by

migrating to these laboratory measurements. The on-site measurements are collections of transmissions from scenarios of interest to the US Navy. These measurements are available to researchers.¹ Extending these measurements to additional transmission scenarios is underway.

Chapter 8 gathers the preceding work to evaluate channel estimators on selected maritime channels. Evaluation of time-invariant channels is straightforward: The channel estimates produce both the Power-Delay profile and the Input Delay-Spread function. These estimates are laid side-by-side to let the reader make a quick graphical comparison. More demanding is the estimation of time-variant channels. The Input Delay-Spread functions are now random so the displays are realizations drawn from the underlying ensemble. For example, the maritime channels are typically modeled as a collection of a few fading reflectors. Again, laying the estimates side-by-side permits graphical comparisons regarding the position and fading of these reflectors.

Chapter 9 concludes this effort by summarizing the “lessons learned” and the plans for Phase II.

1.2 Recent Channel Estimation Literature

What are future candidates for channel estimation algorithms? Table 1.1 provides a partial answer by laying out recent channel estimate schemes. The columns tabulate the transmission scheme, the channel model, the processing, and the references. It appears that each transmission scheme has its suite of channel estimators. For example, OFDM admits several fascinating schemes using pilot symbols. The comparative study of Sandell & Edfors [72] is a fine example of this pilot-based channel estimation using 2D interpolation. Relevant to the setup used in this report, the subspace methods are the next set of target algorithms.

The recent dates on these references demonstrate that channel estimation is a huge and active field. To write a chapter on every combination of transmission scheme, time-variant channel, and channel estimator makes an interesting combinational problem — not to mention actually carrying out the analysis. Thus, the long-term value of this report is that it keeps to the foundations for a particular transmission scheme and offers real-world measurements to the research community.

¹Contact Rich North at rnorth@spawar.navy.mil.

Table 1.1: Channel Estimation: FS = frequency selective fading; FF = flat fading; MP = multipath; CCSE = combined channel and sequence estimation.

Signal	Channel	Channel Estimation	Reference
OFDM	—	SVD	[1996] Edfors
OFDM	FS	CD3	[1996] Mignone
OFDM	FF	MMSE	[1995] van de Beek
OFDM	FF	LS	[1995] van de Beek
OFDM	—	pilot block subchannels	[1995] Bossert
OFDM	FS	—	[1995] Classen
CDMA	FS	antenna diversity	[1996] Zvonar
CDMA	MP	subspace	[1996] Bensley
CDMA	MP	pilot symbol	[1995] Papproth
CDMA	—	subspace	[1994] Bensley
TDMA	FS	MAPSD	[1996] Giridhar
TDMA	FS	dual	[1996] Baccarelli
TDMA	FS	interpolated training segments	[1995] Pechtel
TDMA	MP	CCSE	[1995] Ranta
TDMA	—	CCSE	[1994] Lin
—	—	HOS	[1996] Tugnait
—	—	HOS	[1995] El-Khamy
CPM	FS	pilot symbol	[1995] Kim
CPM	FF	pilot symbol	[1996] Ho
OFDM-CDMA	FS	pilot symbol	[1995] Mueller
—	FS	spatial	[1995] Raleigh
DS-CDMA	MP	pilot signal	[1996] Krenz
DS-CDMA	MP	adaptive gradient	[1996] Krenz
DS-CDMA	MP	pilot symbol	[1996] Andoh
—	FS	Taylor's expansion	[1995] Guanghua
—	—	Per-survivor processing	[1995] Polydoros
—	MP	pilot signal	[1996] Fukasawa
—	HF	probe	[1996] Willink
—	FS	CCSE	[1995] Forest
—	—	CCSE	[1995] Kuor-Hsin
—	MP	Combined RAKE and antenna	[1995] Khalaj
—	MP	Per-survivor processing	[1996] Hamied
DPSK	FF	adaptive symbol-aided	[1996] Kong
BPSK	—	subchannel response matching	[1995] Goeckell
CPFSK	—	reduced state sequence est.	[1995] Poo

1.3 Notation

The notation was selected to be consistent with as much of the literature as possible and to permit the reader to “drop in” on an equation without a lot of notational baggage. We follow Staley’s notation in his excellent thesis [82] wherein the subscripts “ T ” and “ R ” denote the transmitter and receiver. Table 1.2 was designed with this rule in mind and with an effort to reduce notational collisions.

Table 1.2: Table of Notation

Symbol	Description
β	roll-off factor
D	divergence factor
ϵ	complex permittivity
f	frequency (Hertz)
f_c	carrier frequency (Hertz)
f_D	maximal Doppler frequency or fate rate (Hertz)
Γ	reflection coefficient
G_T	gain of transmitter’s antenna
G_R	gain of receiver’s antenna
G_0	free-space propagation gain
h_T	transmitter’s antenna height (feet)
h_R	receiver’s antenna height (feet)
$h(t, \tau)$	Input Delay-Spread function
$h_B(t, \tau)$	baseband Input Delay-Spread function
$H(f, \nu)$	Output Doppler-Spread function
O_s	oversampling factor
λ	wave length (meters)
$p_f(f)$	Doppler scattering function
$p_\tau(\tau)$	power delay profile
$p_T(t)$	transmitter’s pulse-shaping filter
$p_R(t)$	receiver’s matching filter
P_T	transmitter’s power (Watts)
P_R	receiver’s power (Watts)
P_0	free-space power (Watts)
$P_{xx}(f)$	power spectrum of $\{x(t)\}$
\mathcal{R}	roughness coefficient
$R_{xx}(t_1, t_2)$	covariance of $\{x(t)\}$
R_b	symbol rate (Hertz)
t	time (seconds)
T	symbol duration (seconds)
τ	delay (seconds)
θ_g	grazing angle (radians)
$T(t, f)$	Time-Variant Transfer function
$S_{xx}(f_1, f_2)$	two-dimensional spectrum of $\{x(t)\}$
$U(f, \tau)$	Doppler-Delay function
$x_{RC}(t)$	Raised cosine filter

The Fourier transform of a signal $s(t)$ is

$$\hat{s}(f) = \int_{-\infty}^{\infty} e^{-j2\pi ft} s(t) dt.$$

The convolution of $s(t)$ with a filter $h(t)$ is

$$h * s(t) = \int_{-\infty}^{\infty} h(t - \tau) s(\tau) d\tau.$$

A random process is denoted by $\{x(t)\}$. The covariance of $\{x(t)\}$ is

$$R_{xx}(t_1, t_2) = E[x(t_1)\overline{x(t_2)}],$$

where the complex conjugate is denoted by the overline. If $\{x(t)\}$ is harmonizable then it admits a representation by a stochastic Fourier measure

$$x(t) = \int_{-\infty}^{\infty} e^{+j2\pi ft} dX(f).$$

Equivalently, $R_{xx}(t_1, t_2)$ admits a representation as the 2D Fourier transform of the covariance of $X(f)$:

$$R_{xx}(t_1, t_2) = \int_{-\infty}^{\infty} \int_{-\infty}^{\infty} e^{+j2\pi\{f_1 t_1 - f_2 t_2\}} dS_{xx}(f_1, f_2),$$

where $S_{xx}(f_1, f_2) = E[X(f_1)\overline{X(f_2)}]$. If $\{x(t)\}$ is *wide-sense stationary* (WSS) then it is standard to write

$$R_{xx}(t_1, t_2) = R_{xx}(t_1 - t_2).$$

This is equivalent that the 2D spectrum is supported on the main diagonal in the frequency plane:

$$S_{xx} = P_{xx}(f_1) \delta(f_1 - f_2),$$

where $P_{xx}(f)$ is the usual power spectrum.

Matrix and vector notation is standard: Vectors are bold lower case \mathbf{x} and assumed to be in column form:

$$\mathbf{x} \sim N_{\mathbf{x}} \times 1,$$

where $N_{\mathbf{x}}$ denotes the number of rows of \mathbf{x} . Matrices are upper case A with dimensions indicated as

$$A \sim M \times N.$$

The matrix transpose is A^T and the conjugate transpose is A^H .

Chapter 2

Time-Varying Channels: Baseband PMFS

The communication literature uses two basic channel models [39]: the *phase-modulation fading simulator* (PMFS) and the *quadrature-modulation fading simulator* (QMFS). The PMFS provides a clean analytical model that beautifully illustrates the fundamental channel functions. It also subsumes, via the theory of harmonizable processes, the QMFS. However, the QMFS permits a more compact and flexible implementation. This report exploits the strong points of both models. This chapter uses the PMFS to obtain a clean and efficient coverage of channel concepts, statistical issues, and modeling techniques. The next chapter uses this groundwork for a rapid treatment of the QMFS which is used for the simulations.

An end-to-end wireless channel simulation requires that the channel model be imbedded between a simulated transmitter and receiver. There are two approaches to simulate such a wireless setup on a computer [91]: Either a passband simulation or a baseband simulation. The passband simulation includes the high-frequency modulation and requires a correspondingly high sample rate. The baseband simulation needs only to model at the symbol rate but requires assumptions about the passband processing. This report uses baseband simulation. We make explicit the modeling assumptions. Figure 2.1 illustrates the setup for a baseband simulation. A complex sequence $\{s_k\}$ is to be transmitted. In the “D/A” block, $\{s_k\}$ modulates a sequence of impulses that are then filtered by the transmitter’s pulse-shaping filter $p_T(t)$.

The baseband transmission is then

$$s(t) = \sum_{k=-\infty}^{\infty} s_k p_T(t - kT).$$

After passing through the baseband time-varying channel, the signal at the receiver's antenna $e(t)$ is corrupted by additive noise $\{\eta(t)\}$, and matched by the receiver's filter $p_R(t)$. The baseband signal at the input of the receiver's A/D is

$$y(t) = p_R * e(t) + p_R * \eta(t).$$

After sampling, the received sequence $\{y(t_m)\}$ will then be used for channel estimation in the subsequent chapters. For now, we focus on modeling the channel in the context of this digital baseband simulation.

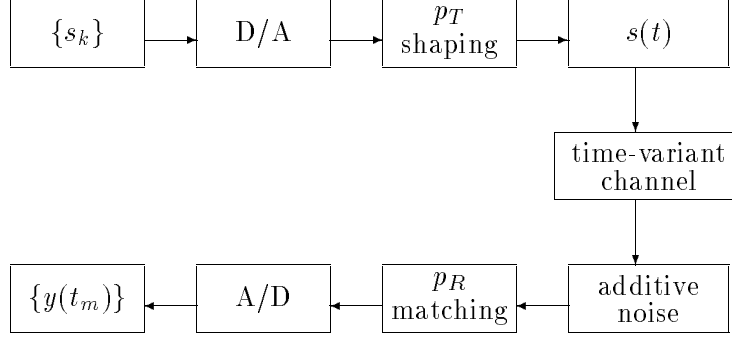


Figure 2.1: Block diagram of the baseband transmitter, time-varying channel, and receiver

Section 2.1 reviews the basic channel functions. Section 2.2 treats the PMFS and introduces a model for the delay and Doppler. Section 2.3 shows how the channel functions and their covariances explicitly reveal the delay and Doppler model. Because delay and Doppler “spreads” are important for estimating system performance, recent results on these channel statistics are covered in Section 2.4. The preceding developments are gathered in an implementation for use in the subsequent chapters. Section 2.5 presents the necessary assumptions for a linear baseband model of a PMFS. Section 2.6 “digitizes” the baseband model for a digital PMFS. Section 2.7 presents the resulting digital channel functions.

2.1 Channel Functions

Bello's seminal 1963 paper established the nomenclature and analysis for stochastic time-variant linear channels [3]. The *kernel system* is based on the *Time-Variant Impulse Response* $K_1(t, \tau)$ mapping an input $s(t)$ to an output $e(t)$:

$$e(t) = \int_{-\infty}^{\infty} K_1(t, \tau) s(\tau) d\tau.$$

This kernel admits a straight-forward correspondence with matrix operators and an immediate time-to-frequency conversion using the Fourier transform. However, Bello observed that these kernels “do not readily allow one to grasp by inspection the way in which the time-variant filter affects input signals to produce output signals.” He introduces the following four channel functions via a simple change of basis.¹ The Fourier transform links between each channel function are illustrated in Figure 2.2.

Input Delay-Spread Function [3, Eq. 9]

$$h(t, \tau) = K_1(t, t - \tau)$$

with output [3, Eq. 8]

$$e(t) = \int_{-\infty}^{\infty} h(t, t - \tau) s(\tau) d\tau.$$

This “leads to a physical picture of the channel as a continuum of nonmoving scintillating scatterers” [3].

Delay-Doppler-Spread Function [3, Eq. 28]

$$U(f, \tau) = \int_{-\infty}^{\infty} e^{-j2\pi f t} h(t, \tau) dt$$

with output [3, Eq. 29]

$$e(t) = \int_{-\infty}^{\infty} \int_{-\infty}^{\infty} U(f, \tau) e^{+j2\pi f t} s(t - \tau) d\tau df.$$

¹This change of basis rotates the diagonal supports due to each reflector in $K_1(t, \tau)$ into vertical supports in $h(t, \tau)$. This permits separability of the delay and Doppler.

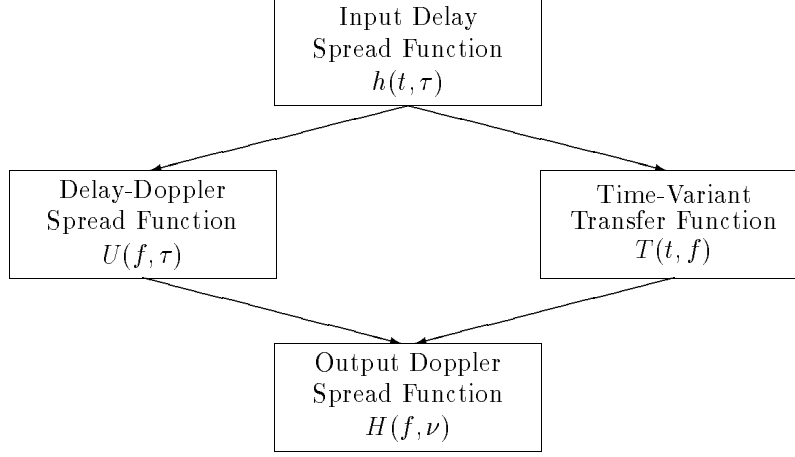


Figure 2.2: Fourier transform mappings between the channel functions (From Bello [1963])

Time-Variant Transfer Function [3, Eq. 18]

$$T(t, f) = \int_{-\infty}^{\infty} e^{-j2\pi f\tau} h(t, \tau) d\tau$$

with output [3, Eq. 19]

$$e(t) = \int_{-\infty}^{\infty} T(t, f) e^{+j2\pi ft} \hat{s}(f) df.$$

Output Doppler-Spread Function [3, Eq. 36]

$$H(f, \nu) = \int_{-\infty}^{\infty} \int_{-\infty}^{\infty} e^{-j2\pi\{ft+\nu\tau\}} h(t, \tau) dt d\tau$$

with output [3, Eq. 14]

$$\hat{e}(f) = \int_{-\infty}^{\infty} H(f, \nu) \hat{s}(f - \nu) d\nu.$$

With each channel function, Bello associates the corresponding covariance. Under various assumptions on the channel, these covariance functions admit simple forms. For example, we will see that the covariance of the Delay-Doppler-Spread Function under WSSUS assumptions takes the form:

$$R_{UU}(f, \tau; f', \tau') = E[U(\tau, f) \overline{U(\tau', f')}] = P(f, \tau) \delta(f - f') \delta(\tau - \tau'),$$

where $P(f, \tau)$ is called the *scattering function*. So which covariance function to use? The answer depends on the channel — certain channel statistics become wonderfully transparent when viewed with the right covariance function. For this reason, we turn to our channel models and then analyze them using a covariance function best suited for the model.

2.2 Phase-Modulation Fading Simulator

Hoeher [39] and Sandell & Edell [72] model a channel as a *phase-modulation fading simulator* (PMFS):

$$h(t, \tau) = \frac{1}{\sqrt{N}} \sum_{n=1}^N a_n e^{+j2\pi f_n t} \delta(\tau - \tau_n). \quad (2.1)$$

Thus, the signal received at the antenna $e(t)$ is determined from the transmitted signal $s(t)$ as:

$$\begin{aligned} e(t) &= \int_{-\infty}^{\infty} h(t, \tau) s(t - \tau) d\tau \\ &= \frac{1}{\sqrt{N}} \sum_{n=1}^N a_n e^{+j2\pi f_n t} s(t - \tau_n). \end{aligned}$$

Thus, $e(t)$ follows Bello's observations in Section 2.1 — that the Input Delay-Spread Function $h(t, \tau)$ models a collection of reflectors where each reflector delays and Doppler shifts the signal. We will see that the PMFS is a general channel model that subsumes several channel models with appropriate statistical assumptions. It also admits a particularly straight-forward covariance analysis. These topics will be explored in Sections 2.3 and 2.4. However, any implementation of the PMFS requires explicit consideration of ergodicity for practical use. This is tackled in later sections. The baseline assumptions invoked for the PMFS are from Hoeher and made explicit as follows [39]:

PMFS-1 The (a_n, f_n, τ_n) 's are IID.

PMFS-2 The a_n 's have zero mean.

PMFS-3 The a_n 's are independent from the f_n 's and the τ_n 's.

PMFS-1 makes explicit that there exists a density $p_{a,f,\tau}(a, f, \tau)$. PMFS-2 “uncorrelates” each path that endows the PMFS with strong stationarity properties. PMFS-3 separates the density $p_a(a)$ of the a_n 's from the Doppler and delay:

$$p_{a,f,\tau}(a, f, \tau) = p_a(a) p_{f,\tau}(f, \tau).$$

The Delay-Doppler Spread Function takes the elegant form showing that the signal is “spread” in time and frequency:

$$U(f, \tau) = \frac{1}{\sqrt{N}} \sum_{n=1}^N a_n \delta(f - f_n) \delta(\tau - \tau_n). \quad (2.2)$$

Assumptions PMFS-1, PMFS-2, and PMFS-3 make $U(f, \tau)$ a generalized random field. Handy computational tricks for generalized random processes and fields are given in Appendix A. With these tools, it is immediate that both $E[h(t, \tau)]$ and $E[U(f, \tau)]$ are zero and

$$\begin{aligned} R_{UU}(f, \tau; f', \tau') &= E[U(f, \tau) \overline{U(f', \tau')}] \\ &= \frac{1}{N} \sum_{n=1}^N \sum_{n'=1}^N E[a_n \bar{a}_{n'}] E[\delta(f - f_n) \delta(\tau - \tau_n) \delta(f' - f_{n'}) \delta(\tau' - \tau_{n'})] \\ &= \frac{1}{N} \sum_{n=1}^N \sigma_a^2 \delta(f' - f) \delta(\tau' - \tau) p_{f, \tau}(f, \tau) \\ &= \sigma_a^2 p_{f, \tau}(f, \tau) \delta(f - f') \delta(\tau - \tau'). \end{aligned} \quad (2.3)$$

Thus, the PMFS gives a straight-forward derivation that the scattering function is proportional to the probability distribution of the Doppler and delays.

2.3 Covariance Functions

For the purpose of comparing the covariance functions, we will make the additional assumption that the Doppler and delays are independent. Formally,

PMFS-4 The f_n ’s and the τ_n ’s are independent.

This is equivalent that the probability distribution $p_{f, \tau}(f, \tau)$ is separable:

$$p_{f, \tau}(f, \tau) = p_f(f) p_\tau(\tau).$$

Then the covariance of the Input Delay-Spread Function is

$$R_{hh}(t, \tau; t', \tau') = \sigma_a^2 \widehat{p}_f(t - t') p_\tau(\tau) \delta(\tau - \tau')$$

and is called the *tap-gain correlation function* [81], the *path-gain correlation function* [5], or the *space-time cross-covariance* [77]. The Time-Variant Transfer Function is

$$T(t, f) = \frac{1}{\sqrt{N}} \sum_{n=1}^N a_n e^{+j2\pi f_n t} e^{-j2\pi f \tau_n}$$

with covariance

$$R_{TT}(t, f; t', f') = \sigma_a^2 \widehat{p}_f^{-1}(t - t') \widehat{p}_\tau(f - f')$$

called the *time-frequency correlation function* [81], [5], the *spaced-frequency, spaced-time correlation function* [63], or the *frequency-time cross-variance* [77]. The Output Doppler-Spread Function is

$$H(f, \nu) = \frac{1}{\sqrt{N}} \sum_{n=1}^N a_n \delta(f - f_n) e^{-j2\pi \nu \tau_n}$$

with covariance

$$R_{HH}(f, \nu; f', \nu') = \sigma_a^2 p_f(f - f') \widehat{p}_\tau^{-1}(\nu - \nu').$$

The simple forms of the covariance functions are due to Bello's adroit change of variables and his Fourier transform relations.

So what is the effect of the channel on the signal? More precisely, how does the delay-Doppler density $p_{f,\tau}(f, \tau)$ affect $e(t)$? The answer depends on the signal $s(t)$ and what "ensemble" information we have. When we have access to the expectation operator, the following result is obtained for a stochastic signal.

Lemma 2.3.1 *Assume PMFS-1, PMFS-2, and PMFS-3 hold. Assume $\{s(t)\}$ is a strongly harmonizable signal independent of the channel. Then the received signal*

$$e(t) = \frac{1}{\sqrt{N}} \sum_{n=1}^N a_n e^{+j2\pi f_n t} s(t - \tau_n)$$

is also strongly harmonizable with stochastic Fourier representation

$$\widehat{e}(f) = \frac{1}{\sqrt{N}} \sum_{n=1}^N a_n e^{-j2\pi f \tau_n} \widehat{s}(f - f_n).$$

Its covariance is

$$R_{ee}(t_1, t_2) = \sigma_a^2 \int_{-\infty}^{\infty} \int_{-\infty}^{\infty} e^{+j2\pi f\{t_1-t_2\}} R_{ss}(t_1 - \tau, t_2 - \tau) dp_{f,\tau}(f, \tau).$$

Its two-dimensional (2D) spectrum is

$$R_{\hat{e}\hat{e}}(f_1, f_2) = \sigma_a^2 \int_{-\infty}^{\infty} \int_{-\infty}^{\infty} e^{+j2\pi\{f_1-f_2\}\tau} S_{ss}(f_1 - f, f_2 - f) dp_{f,\tau}(f, \tau),$$

where $S_{ss}(f_1, f_2)$ denotes the 2D spectrum of $\{s(t)\}$. If $\{s(t)\}$ is WSS then $\{e(t)\}$ is also WSS with covariance

$$R_{ee}(t_1, t_2) = \sigma_a^2 \widehat{p_f}^{-1}(t_1 - t_2) R_{ss}(t_1 - t_2)$$

and spectrum

$$R_{\hat{e}\hat{e}}(f_1, f_2) = \sigma_a^2 p_f * P_{ss}(f_1) \delta(f_1 - f_2),$$

where $P_{ss}(f)$ denotes the power spectrum of $\{s(t)\}$.

Lemma 2.3.1 shows that the Doppler density alone affects a WSS signal — the delay density has no effect — on the average. This phenomenon will be present in the other channel models. It is due to the WSS assumption of the signal or, more generally, that we have access to the ensembles of the signal and channel. In practice, we will only have the result of passing a signal through a *single* realization of the channel. The next result is more in line with this information limit.

Lemma 2.3.2 *Assume PMFS-1, PMFS-2, and PMFS-3 hold. Assume $s(t)$ deterministic with $s \in L^2(\mathbb{R}) \cap L^1(\mathbb{R})$. Then the received signal $\{e(t)\}$ is strongly harmonizable with*

$$E[|e(t)|^2] = \sigma_a^2 |s|^2 * p_\tau(t)$$

and

$$E[|\hat{e}(f)|^2] = \sigma_a^2 |\hat{s}|^2 * p_f(f).$$

Lemma 2.3.2 shows that a deterministic input gives a stochastic output whose second moments are governed by the distribution of the delays and Doppler. Because of the practical importance of this delay and Doppler “spread”, recent results on these estimates are covered in the next section.

2.4 Delay & Doppler Spread

The delay and Doppler “spread” — the second moments of $p_{f,\tau}(f, \tau)$ — are useful for characterizing wireless system performance [61, page 184–185], [85]. Not surprisingly, applications have given rise to competing nomenclatures and “rules-of-thumb” for system design. In contrast, recent work by Fleury provides an excellent synthesis of theory and applications [25], [26], [24]. Therefore, Fleury’s approach to the delay and Doppler spread is reviewed here and applied in the subsequent simulations.

There are four functions to discuss: the marginals of the delay and Doppler $p_\tau(\tau)$, $p_f(f)$ and their Fourier transforms $\widehat{p}_f^{-1}(\tau)$, $\widehat{p}_\tau(f)$. Each function has a “spread” that satisfies an uncertainty relation with its Fourier transform. The trick is to define the spread. Table 2.1 summarizes the necessary notation. Also needed is the notion of a coherence interval. If $R(x)$ is a covariance function, then the *coherence interval at level c* [25]:

$$D_c[R] = \inf\{x : |R(x)| < cR(0)\}.$$

Table 2.1: Delay and Doppler Nomenclature

Symbol	Description
$p_\tau(\tau)$	power delay profile [60], multipath intensity profile [63, page 762], delay scattering function [25]
$\mu_\tau = E[\tau]$	mean delay [93, page 129], mean excess delay [60]
$\sigma_\tau = E[(\tau - \mu_\tau)^2]^{1/2}$	delay spread [60], [25]
T_M	multipath spread [63, page 763], [49]
$\widehat{p}_\tau(f)$	frequency correlation function [25]
$D_c[\widehat{p}_\tau]$	coherence bandwidth at level c [25]
$p_f(f)$	Doppler scattering function [25]
$\mu_f = E[f]$	mean Doppler
$\sigma_f = E[(f - \mu_f)^2]^{1/2}$	Doppler spread [25]
B_D	Doppler spread [63, page 765], [85]
$\widehat{p}_f^{-1}(\tau)$	time correlation function [25]
$D_c[\widehat{p}_f^{-1}]$	coherence time at level c [25]

Remarks: (i) Bello uses [4]: $T_M = 2\sigma_\tau$ and $B_D = 2\sigma_f$. (ii) A rule of thumb [60]: A channel can be considered flat when σ_τ/T is less than 0.1. (iii) Limited bandwidth may be overcome by using a Prony algorithm [45].

Applications: The value of knowing these spreads is given by Stein with immediate applications to our PN processing [85]: “to process a symbol waveform with a filter matched to the waveform as transmitted, two separate criteria must be satisfied: one, that there be essentially no loss of coherence as received [$T \ll 1/B_D$]; the other, that there be essentially no frequency-selective distortion of the symbol [$T \gg T_M$]; this leads to the double inequality $T_M \ll T \ll 1/B_D$ ”.

Theory: Fleury’s uncertainty relation part of the general moment theory of covariance functions [24]. We adapt the following special case from [25].

Theorem 2.4.1 *Let p denote a probability measure on \mathbb{R} with characteristic function*

$$\hat{p}^{-1}(x) = \int_{-\infty}^{\infty} e^{+j2\pi xy} dp(y).$$

Assume p has a finite second moment:

$$E[y^2] = \int_{-\infty}^{\infty} y^2 dp(y) < \infty.$$

Then the variance exists: $\sigma_y^2 = E[(y - E[y])^2]$. Define

$$D_c[\hat{p}^{-1}] = \inf \{x : |\hat{p}^{-1}(x)| < c\}.$$

Then for all $c \in [0, 1]$

$$\sigma_y D_c[\hat{p}^{-1}] \geq \frac{\arccos(c)}{2\pi}.$$

Example 2.4.1 (Exponential Delay) A common model for the delay profile is [93, page 130]

$$p_\tau(\tau) = 1_{[0, \infty)}(\tau) \frac{1}{\sigma_\tau} e^{-\tau/\sigma_\tau}.$$

Then the frequency correlation function is

$$\widehat{p}_\tau(f) = \frac{1}{1 + j2\pi f\sigma_\tau},$$

so that

$$D_c[\widehat{p}_\tau] = \frac{1}{2\pi\sigma_\tau} \sqrt{c^{-2} - 1}.$$

It can be verified that $\sigma_\tau D_c[\widehat{p}_\tau]$ satisfies the inequality of Theorem 2.4.1 for $c \in [0, 1]$. Figure 2.3 illustrates the uncertainty relation from Theorem 2.4.1. \square

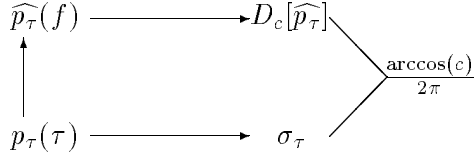


Figure 2.3: Uncertainty relation for the delay spread σ_τ and the coherence bandwidth $D_c[\widehat{p}_\tau]$.

Example 2.4.2 (Gaussian Doppler) A model for the Doppler scattering function is [6]

$$p_f(f) = \frac{1}{\sqrt{2\pi}\sigma_f} e^{-f^2/2\sigma_f^2}.$$

Then the time correlation function is

$$\widehat{p}_f^{-1}(\tau) = \exp(-2(\pi\sigma_f\tau)^2),$$

so that

$$D_c[\widehat{p}_f^{-1}] = \frac{1}{\pi\sigma_f} \sqrt{-\log(c)/2}.$$

Again, it can be verified that $\sigma_f D_c[\widehat{p}_f^{-1}]$ satisfies the inequality of Theorem 2.4.1 for $c \in [0, 1]$. Figure 2.4 illustrates the uncertainty relation from Theorem 2.4.1. \square

Measurements: Fleury [25], [26] presents an impressive scatter plot of measured delay spread versus coherence bandwidth ($\sigma_\tau, D_{0.5}[\widehat{p}_\tau]$) closely bounded by the theoretical hyperbola $\sigma D \geq \arccos(0.5)/2\pi$. What is also impressive is Fleury's verification of empirical approximations of Gans' "1/8 rule" for $c=3/4$ [28]. Fleury obtains [25]

$$\sigma_\tau D_{3/4}[\widehat{p}_\tau] \geq \frac{1}{8.694}.$$

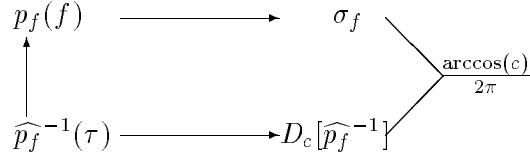


Figure 2.4: Uncertainty relation for the Doppler spread σ_f and the coherence time $D_c[\widehat{p}_f^{-1}]$.

No measurements assessing the theory for Doppler spread versus time correlation ($\sigma_f, D_c[\widehat{p}_f^{-1}]$) have been located to date. No work taking this same approach to the joint distribution $p_{f,\tau}(f, \tau)$ has been found. Measurements have been made that show the variations in the measured delay profiles are log-normal [79]. No work exploiting such *a priori* models for improving the estimates of the delay profile have been found.

2.5 Baseband PMFS

The preceding sections covered the PMFS and the channel functions. The remainder of this chapter will put these concepts in the context of a baseband simulation as illustrated in Figure 2.1. Start with the following assumptions:

B-1: Linear Modulation The signal $s_{\text{RF}}(t)$ transmitted at RF is obtained from the baseband signal $s(t)$ as

$$s_{\text{RF}}(t) = e^{+j2\pi f_c t} s(t).$$

B-2: Linear Demodulation The received baseband signal $e(t)$ is demodulated from the RF signal as

$$e(t) = e^{-j2\pi f_c t} \int_{-\infty}^{\infty} h_{\text{RF}}(t, \tau) s_{\text{RF}}(t - \tau) d\tau,$$

where $h_{\text{RF}}(t, \tau)$ denotes the RF Input Delay-Spread function.

B-3: Perfect Synchronization The receiver and transmitter operate from a master clock.

Both B-1 and B-2 require that the modulation be linear in both the transmitter and receiver. See Felhauer [21], [22], [23] for processing that can handle

non-linearities in the amplifiers. For brevity, set $\Delta f = f_c - f'_c$. Then B-1, B-2, and Equation 2.1 give the baseband PMFS as

$$\begin{aligned} h(t, \tau) &= e^{+j2\pi\Delta f t} h_{\text{RF}}(t, \tau) e^{-j2\pi f_c \tau} \\ &= \frac{1}{\sqrt{N}} \sum_{n=1}^N \left\{ a_n e^{-j2\pi f_c \tau_n} \right\} e^{+j2\pi\{\Delta f + f_n\}t} \delta(\tau - \tau_n). \end{aligned} \quad (2.4)$$

That is, the a_n 's are rotated and the Doppler frequencies are shifted but the form of the phase-modulation fading simulator is unchanged. Assumptions B-1, B-2, and B-3 are fundamental to any baseband simulation. To go further requires a model of the receiver.

2.6 Digital Baseband PMFS

Following [58] and [40], the baseband channel input has the complex baseband form

$$s(t) = \sum_{k=-\infty}^{\infty} s_k p_T(t - kT). \quad (2.5)$$

B-1 and B-2 give the baseband antenna input as

$$e(t) = \int_{-\infty}^{\infty} h(t, \tau) s(t - \tau) d\tau.$$

The baseband receiver input is [93, Eq. 8.3]

$$x(t) = e(t) + \eta(t), \quad (2.6)$$

where $\{\eta(t)\}$ is a complex-valued, zero-mean, Gaussian random process with spectrum determined by the IF filter. We assume the receiver filter $p_R(t)$ is matched to the transmitter filter $p_T(t)$:

B-4 Matched Filter The convolution of the transmitter filter $p_T(t)$ and the receiver filter $p_R(t)$ is the raised cosine filter [64, pages 63–65]: $p_R * p_T(t) = x_{\text{RC}}(t)$.

With the baseband channel given by Equation 2.1 and the baseband signal given by Equation 2.5, the baseband input to the receiver's detector due to the signal is

$$p_R * e(t) = \frac{1}{\sqrt{N}} \sum_{n=1}^N \sum_{k=-\infty}^{\infty} s_k a_n \int_{-\infty}^{\infty} p_R(u) e^{+j2\pi f_n\{t-u\}} p_T(t - u - \tau_n - kT) du.$$

To numerically implement such integrals, we invoke a *slow-fading* assumption:

B-5 Slow Fading The distribution of the f_n 's are “small” with respect to the bandwidth of the receiver filter $p_R(t)$.

Appendix B shows that B-4 and B-5 give the approximation:

$$\begin{aligned} & \int_{-\infty}^{\infty} p_R(u) e^{+j2\pi f_n \{t-u\}} p_T(t-u) du \\ & \approx e^{+j2\pi f_n t} \int_{-\infty}^{\infty} p_R(u) p_T(t-u) du \\ & = e^{+j2\pi f_n t} x_{RC}(t) \end{aligned}$$

with a mean-square error bounded by $6f_n T^2$. Typical values for this report are $T \approx 10^{-6}$ seconds and $|f_n| < 25$ Hertz. Thus, the approximation error — for each pulse — is deemed negligible. By B-3, synchronized sampling is possible. That is, the receiver may sample $y(t)$ at instants $t_m = mT/O_s$, where O_s denotes the oversampling factor. A typical value is $O_s = 2$. Then the detector input is well approximated as:

$$\begin{aligned} y(t_m) &= p_R * e(t) + p_R * \eta(t)|_{t=t_m} \\ &\approx \frac{1}{\sqrt{N}} \sum_{k=-\infty}^{\infty} \sum_{n=1}^N e^{+j2\pi f_n t_m} a_n x_{RC}(t_m - kT - \tau_n) s_k \\ &\quad + p_R * \eta(t_m). \end{aligned} \tag{2.7}$$

This is the foundational equation for the PMFS. It will be implemented in the simulations and used to define the *digital* channel functions. The digital channel functions are the discrete analogs of the continuous channel functions. However, the mismatch between the sampling rate O_s/T and the symbol rate $1/T$ prevents an immediate correspondence between the continuous convolution and the discrete convolution. There are two approaches to work around this mismatch: (i) Zero-fill the input sequence $\{s_k\}$; (ii) Vectorize the output. This chapter zero-fills while vectorization is naturally discussed in the subspace methods.

The problem is to write Equation 2.7 using a digital convolution. To do this, zero-fill $\{s_k\}$ as

$$\tilde{s}_l = \begin{cases} s_{l/O_s} & \text{rem}(l, O_s) = 0 \\ 0 & \text{otherwise} \end{cases}. \tag{2.8}$$

Set $\tilde{T} = T/O_s$. Then the business part of Equation 2.7 may be written as the discrete convolution

$$\begin{aligned} e(t_m) &\approx \frac{1}{\sqrt{N}} \sum_{k=-\infty}^{\infty} \sum_{n=1}^N e^{+j2\pi f_n m \tilde{T}} a_n x_{\text{RC}}(k\tilde{T} - \tau_n) \tilde{s}_{m-k} \\ &= \sum_{k=-\infty}^{\infty} h_B(m, k) \tilde{s}_{m-k}, \end{aligned}$$

where $h_B(m, k)$ denotes (an approximation to) the *baseband digital Input Delay-Spread Function*:

$$h_B(m, k) = h *_{\tau} x_{\text{RC}}(m\tilde{T}, k\tilde{T}) = \frac{1}{\sqrt{N}} \sum_{n=1}^N a_n e^{+j2\pi f_n m \tilde{T}} x_{\text{RC}}(k\tilde{T} - \tau_n). \quad (2.9)$$

Approximation and Convolution: Appendix B shows that $h_B(m, k)$ is an approximation obtained by commuting a multiplication and a convolution operator. This form of $h_B(m, k)$ permits a straight-forward MATLAB implementation using convolution functions.

Sampling: Equation 2.9 reveals the sampling requirements for channel estimation (See Staley [82] for an in-depth treatment of this topic). Resolution of the Doppler frequencies requires $1/\tilde{T} > 2 \max |f_n|$. Resolution of the raised-cosine filter requires $1/\tilde{T}$ exceed $(1 + \beta)/T$, where β is the *rolloff factor* [63, page 553]. Thus, the sampling rate should exceed

$$\frac{1}{\tilde{T}} = \frac{O_s}{T} \geq \max \left\{ \frac{1 + \beta}{T}, 2|f_n| \right\}. \quad (2.10)$$

2.7 Digital Channel Functions

We have access to only the digital channel functions but want to estimate the continuous channel functions. Therefore, we seek the relation between the two classes of channel functions. This section computes the digital Input Delay-Doppler function $U_B(f, k)$ and its covariance. Start from the digital Input Delay-Spread function $h_B(m, k)$ of Equation 2.9. Apply the Fourier

transform along the columns to obtain the digital Input Delay-Doppler function:

$$\begin{aligned} U_B(f, k) &= \sum_{m=-\infty}^{\infty} e^{-j2\pi f m \tilde{T}} h_B(m, k) \\ &= \frac{1}{\sqrt{N}} \sum_{n=1}^N a_n \delta(f - f_n) x_{\text{RC}}(k\tilde{T} - \tau_n). \end{aligned}$$

Then $U_B(f, k)$ is related to $U(f, \tau)$ by the convolution along the delay:

$$U_B(f, k) = U *_{\tau} x_{\text{RC}}(f, kT).$$

This result and Equation 2.3 show that the covariance of the digital Input Delay-Doppler function is the covariance of the Input Delay-Doppler function observed through the raised cosine filter:

$$\begin{aligned} R_{U_B U_B}(f, k; f', k') &= E[U_B(f, k) \overline{U_B(f', k')}] \\ &= \delta(f - f') \int_{-\infty}^{\infty} x_{\text{RC}}(k\tilde{T} - \tau) x_{\text{RC}}(k'\tilde{T} - \tau) p_{\tau, f}(\tau, f) d\tau. \end{aligned}$$

With the standard abuse of notation, the digital scattering function is related to the scattering function as:

$$\begin{aligned} E[|U_B(f, k)|^2] &= \int_{-\infty}^{\infty} x_{\text{RC}}^2(k\tilde{T} - \tau) p_{\tau, f}(\tau, f) d\tau \\ &= x_{\text{RC}}^2 *_{\tau} p_{\tau, f}(k\tilde{T}, f). \end{aligned} \tag{2.11}$$

The right-hand side Equation 2.11 is the true scattering function convolved with the raised-cosine pulse. This implies any estimation scheme for digital scattering function can be “boosted” by exploiting this convolution structure. In this regard, David Thompson’s approach for spectral estimation should apply for estimating the channel and scattering functions [88]. The left-hand side of Equation 2.11 requires the expectation operator or access to the ensemble. This impossibility for real-world measurements is either evaded or ignored in the literature. In rare cases, ergodicity is invoked. That is, time averages can approximate the ensemble averages. Unfortunately, the PMFS does not have this critical ergodic property. This defect is the topic of the next section.

2.8 PMFS Simulation Issues

There are issues for the simulation of a PMFS that need to be discussed apart from actual channel estimation problems. For concreteness, we start with an implementation of a baseband PMFS and then move to the simulation issues. The PMFS simulation is built around the digital baseband Input Delay-Spread function $h_B(m, k)$ of Equation 2.9. Assumptions B-1, B-2, B-3, B-4, and B-5 are in force.

Transmit Sequence: The following MATLAB fragment generates the sequence $\{s_k\}$ of length K to be pushed through the channel. Chapter 5 discusses PN sequences and the call to `pn_src(9,1041,K,1)` generating K samples of the CCITT 0.153 standard 511 PN sequence.

```
% Generate the PN sequence
K = input('Enter the number of symbols <128>: ');
if isempty(K); K = 128; end
s = pn_src(9,1041,K,1);
```

Zero-Fill: This sequence is zero-filled to give $\{\tilde{s}_k\}$ for convolution processing (Section 2.6).

```
% Generate zero-filled PN sequence for convolution
Os = input('Enter the oversample factor <2>: ');
if isempty(Os); Os = 2; end
sExt = [s zeros(K,Os-1)].';
sExt = sExt(:);
```

Channel and Receiver Times: We will need two time vectors: The first is `tC` which is the extent of the channel delays or the k 's. Here the extent is the time interval $[0, KT]$. The second is `tR` which is the extent of the receiver or the m 's. Here the extent is the time interval $[0, MT/O_s]$.

```
% 2.3 Generate the time vectors
tC = (T/Os)*([1:(K*Os)]-1).';          % Channel's time extent
NtC = length(tC);
M = length(tC) + length(sExt) - 1;      % Receiver's time extent
tR = (T/Os)*([1:M]-1).';
```

PMFS Parameters: The delay for each path is drawn from the uniform distribution $U[0, KT]$ for the extent of the channel: $\tau_n \sim U[0, KT]$. The Doppler frequency for each path is drawn from the Gaussian distribution: $f_n \sim N(0, \sigma_f^2)$. Thus, the scattering function is proportional to $p_{f,\tau}(f, \tau) = \mathcal{N}(0, \sigma_f^2) \times U[0, KT]$.

```
% Phase-Modulation Fading Simulator: Paths not scaled by sqrt(N)
N = input('Enter the number of paths <3>: ');
if isempty(N); N = 3; end
a = exp( +j*2*pi*rand(N,1) ); % Uniform Phases
tau = rand(N,1)*K*T; % Uniform Time Delays (sec)
fD = randn(N,1)*10 % Gaussian Doppler (Hertz)
```

Transmission through the PMFS: The zero-filled sequence is pushed through each path. Here `rcosplt(t,T,beta)` is a function call to the raised cosine filter $x_{RC}(t)$. A loop is used to save memory.

```
y = zeros(M,1);
for n=1:N
    y = y + a(n)*exp(+j*2*pi*fD(n)*tR) ...
        .*conv2(rcosplt(tC-tau(n),T,beta),sExt);
end
```

Additive Noise: Equation 2.7 shows the additive noise is colored by the square-root raised cosine filter. The call to `srcnoise(M,0s,T,beta)` returns a complex-valued, zero-mean, unit variance, Gaussian time series with the square-root raised cosine power spectrum. The SNR we use is the ratio of the minimum peak value of the matched pulses to the variance of the noise.

$$\text{SNR} = \frac{\min\{|s_k x_{RC}(0)|^2\}}{\sigma_\eta^2} = \frac{1}{\sigma_\eta^2}. \quad (2.12)$$

```
% Channel Noise: Scaled at the receiver
SNR_dB = input('Enter SNR <20 dB>: ');
if isempty(SNR_dB); SNR_dB = 20; end
SNR = 10^(SNR_dB/10);
nu = srcnoise(M,0s,T,beta);
```

```
% Detector input: Unit variance noise is scaled to the SNR
y = y + nu/sqrt(SNR);
```

This completes the treatment of the PMFS and an elementary MATLAB implementation. What are the statistical issues? That is, the preceding implementation of the PMFS “rolls the dice” to draw N samples of the (a_n, f_n, τ_n) ’s. Once these channel parameters are selected, they are held constant over the simulation. The consequences of this approach are addressed next:

How many paths N ? Hoeher avoids this issue by claiming the PMFS is an approximation to the limiting case as $N \rightarrow \infty$ but for simulations used $N = 500$ with no justification [39]. He does state [39] “for small N , it is advisable to compute new random variables [the (a_n, f_n, τ_n) ’s] from time-to-time, because this improves the statistic.” Mathematically, Hoeher is attempting to estimate the probability density $p_{f,\tau}(f, \tau)$ from N samples (f_n, τ_n) . The number of samples and the shape of the density determine the accuracy of the estimated density. Indeed, the 1979 paper by Hashemi [36] attacks this very problem by modeling the number of paths in each time bin. This “packing of the paths” in each time gives a proper statistical counting for estimating the delay density $p_\tau(\tau)$. Also, recent results from Multivariate Density Estimation provide asymptotic estimates of this “histogram” error [78]. However, it is beyond the scope of this effort to push either theory through to obtain such a “patch” to the PMFS. More critical issues await as hinted by Hoeher’s recommendation to draw a new channel from “time-to-time.”

What are the ergodic properties of the PMFS? Hoeher makes the claim that [39] “[T]he realization of the random process has to be computed before the simulation starts. It contains, on the average, the same statistics as any other realization of possible outcomes because of ergodicity.” A classic result is that the Time-Variant Transfer function $T(f, t)$ is mean ergodic but not correlation ergodic [68]. Specifically, it is impossible to get that the a_n ’s are uncorrelated from a single random draw. Consequently, Hoeher’s recommendation that new channels be drawn from “time-to-time” is not an off-hand remark but absolutely critical — the user must have an ensemble of channels for the estimation of second-order statistics. But if a new channel

is to be drawn from “time-to-time”, should not the reflectors evolve in a physically plausible sense? More generally, the question to ask is:

How well does the PMFS model the time-evolution of the channel? Because we are going to be drawing a new channel from “time-to-time”, there arise the mundane questions on the speed of the update: Does it make physical sense to update a channel between every sounding pulse? Should we update during a sounding? More problematic is updating the channel while running a “Kalman filter” channel estimation scheme. That is, a channel estimate is based on the previous channel estimate and new observations. For a credible simulation, the channel parameters should evolve according to a proper physical model. Hoeher’s simple random draw model implies that the channel parameters are independent between soundings. So a physically plausible argument is needed to establish the time gap between observations.

The preceding remarks demonstrate that the PMFS has non-trivial implementation problems. It goes without saying that the hapless reader who has gotten this far will question the worth of the PMFS. The value of the PMFS is that it provides a simple and elegant treatment of the channel functions and their covariances. The problems with the implementation of the PMFS are non-trivial but are overcome by the QMFS discussed in the next chapter.

Chapter 3

Time-Varying Channels: Baseband QMFS

The preceding chapter used the phase-modulation fading simulator for rapid access to the channel functions, digital channel functions, and simulations. This chapter uses these developments for a quick review of the quadrature-modulation fading simulator (QMFS), its channel functions, their covariances, the digital QMFS, and a QMFS simulation.

3.1 Quadrature-Modulation Fading Simulator (QMFS)

North & Zeidler [59], Crohn & Bonek [14], Proakis & Salehi [65, pages 697–703] model a channel with the *quadrature modulation fading simulator*:

$$h(t, \tau) = \sum_{n=1}^N a_n(t) \delta(\tau - \tau_n). \quad (3.1)$$

Typically, the $\{a_n(t)\}$'s are complex-valued, jointly wide-sense stationary (JWSS), uncorrelated Gaussian random processes with mean and spectral shape determined by the propagation environment (See Chapter 4). The channel of Equation 3.1 acts on an input signal as

$$e(t) = \int_{-\infty}^{\infty} h(t, \tau) s(t - \tau) d\tau = \sum_{n=1}^N a_n(t) s(t - \tau_n).$$

3.2 Channel Functions

The Delay-Doppler Spread function is

$$U(f, \tau) = \sum_{n=1}^N \widehat{a}_n(f) \delta(\tau - \tau_n). \quad (3.2)$$

The Time-Variant transfer function is

$$T(t, f) = \sum_{n=1}^N a_n(t) e^{-j2\pi f \tau_n}.$$

The Output Doppler-Spread function is

$$H(f, \nu) = \sum_{n=1}^N \widehat{a}_n(f) e^{-j2\pi \nu \tau_n}.$$

3.3 Covariance Functions

Section 2.2 showed that the scattering function $P(f, \tau) = E[|U(f, \tau)|^2]$ was proportional to the probability density $p_{f,\tau}(f, \tau)$ of the delay and Doppler — assuming the PMFS. Given the importance of the scattering function for characterizing channels from real data (See Chapter 8), it is worthwhile to ask: *How does the scattering function link to $p_{f,\tau}(f, \tau)$ under the QMFS?* The answer depends on the assumptions regarding the delays τ_n 's and the fading processes $\{a_n(t)\}$'s. This section works through a few examples for use in Chapter 8.

Example 3.3.1 The following list is rigged to give a separable scattering function:

QMFS-1 The $\{a_n(t)\}$'s are JWSS and uncorrelated.

QMFS-2 The τ_n 's are IID.

QMFS-3 The τ_n 's are independent from the $\{a_n(t)\}$'s.

Then the covariance of the Delay-Doppler-Spread function may be computed using the tools of Appendix A:

$$R_{UU}(f, \tau; f', \tau') = \delta(f - f')\delta(\tau - \tau') p_\tau(\tau) \sum_{n=1}^N P_{a_n a_n}(f),$$

where $p_\tau(\tau)$ is the density of the delays. Thus, the scattering function $P(f, \tau)$ is separable and given by the product of the delay density $p_\tau(\tau)$ and the sum of the power spectrums of the multiplicative noises. Additional assumptions bring us to the PMFS results. Suppose the $\{a_n(t)\}$'s are narrow-band FM processes with identical spectra. Adding the strict-sense stationarities of Woodward's Theorem [68, page 321-324] permits the approximation:

$$R_{UU}(f, \tau; f', \tau') \approx N \delta(f - f')\delta(\tau - \tau') p_\tau(\tau) p_f(f).$$

That is, $P(f, \tau)$ registers the delay-Doppler distribution. \square

Example 3.3.2 Applicable to slowly moving or stationary transmitters and receivers is the following:

QMFS-1 The $\{a_n(t)\}$'s are JWSS and uncorrelated.

QMFS-2 The τ_n 's are fixed.

Then the covariance of the Delay-Doppler-Spread function is

$$R_{UU}(f, \tau; f', \tau') = \delta(f - f')\delta(\tau - \tau') \sum_{n=1}^N P_{a_n a_n}(f)\delta(\tau - \tau_n).$$

In contrast to Example 3.3.1, the scattering function $P(f, \tau)$ registers the spectral type at each delay. \square

Example 3.3.3 With more freedom in the delays, we get

QMFS-1 The $\{a_n(t)\}$'s are JWSS and uncorrelated.

QMFS-2 The τ_n 's are independent but not identically distributed.

QMFS-3 The τ_n 's are independent from the $\{a_n(t)\}$'s.

Then

$$R_{UU}(f, \tau; f', \tau') = \delta(f - f')\delta(\tau - \tau') \sum_{n=1}^N P_{a_n a_n}(f) p_{\tau_n}(\tau).$$

That is, each path registers its local delay and Doppler distribution. \square

For applications, suppose an estimate $\tilde{P}(f, \tau)$ was obtained from real data. Then Examples 3.3.1, 3.3.2, and 3.3.3, show that an estimate of the power-delay profile $p_\tau(\tau)$ may be obtained by averaging $\tilde{P}(f, \tau)$ over frequency. For the Doppler distribution $p_f(f)$, the sum of the power spectrums in Example 3.3.1 precludes the association of specific spectral types to a particular delay. Unless the power spectrums are identical, the Doppler distribution is lost. In contrast, Examples 3.3.2 and 3.3.3 show that each path registers a local delay and Doppler distribution in $P(f, \tau)$. Chapter 8 invokes a belief system that permits the converse: Well-separated “blobs” in $P(f, \tau)$ register the local delay and Doppler distribution. Thus, the claims such as “the first path is Ricean and the subsequent paths are Rayleigh” can be tested by the resolvable paths in scattering function estimates. Because this estimate is obtained from sampled data, Section 3.4 models digital baseband QMFS. Section 3.5 uses this model to determine the digital channel functions.

3.4 Digital Baseband QMFS

Assumptions B-1, B-2, B-3, and B-4 from Chapter 2 are in force. Following [58] and [40], the channel input has the complex baseband form

$$s(t) = \sum_{k=-\infty}^{\infty} s_k p_T(t - kT).$$

Then Assumptions B-1 and B-2 determine the baseband received antenna input as [93, Eq. 8.3]:

$$x(t) = e(t) + \eta(t),$$

where

$$e(t) = \int_{-\infty}^{\infty} h(t, \tau) s(t - \tau) d\tau,$$

and the noise $\{\eta(t)\}$ is complex-valued, zero-mean Gaussian with spectrum flat over the width of $p_R(t)$. Assumption B-4 and $h(t, \tau)$ of Equation 3.1 give the input to the receiver's detector as

$$\begin{aligned} y(t) &= p_R * x(t) \\ &= \sum_{k=-\infty}^{\infty} s_k \int_{-\infty}^{\infty} \int_{-\infty}^{\infty} p_R(\zeta) h(t - \zeta, t - \zeta - \tau) p_T(\tau - kT) d\zeta d\tau + p_R * \eta(t) \\ &= \sum_{n=1}^N \sum_{k=-\infty}^{\infty} s_k \int_{-\infty}^{\infty} p_R(\zeta) a_n(t - \zeta) p_T(t - \zeta - \tau_n - kT) d\zeta + p_R * \eta(t). \end{aligned}$$

We modify the slow-fading assumption B-5:

B-5' Slow Fading The maximal spectral extent f_D of the $\{a_n(t)\}$'s is “small” with respect to the spectral extent of the receiver filter $p_R(t)$.

Mathematically, we claim the following [63]

$$\begin{aligned} &\int_{-\infty}^{\infty} p_R(\zeta) a_n(t - \zeta) p_T(t - \zeta - \tau_n) d\zeta \\ &\approx a_n(t) \int_{-\infty}^{\infty} p_R(\zeta) p_T(t - \zeta - \tau_n) d\zeta \\ &= a_n(t) x_{\text{RC}}(t - \tau_n). \end{aligned}$$

By B-3, synchronized sampling at time instants $t_m = m\tilde{T}$ is possible. Here $\tilde{T} = T/O_s$ where O_s is the oversampling factor. Thus, Assumptions B-1, B-2, B-3, B-4, and B-5' give the approximation to the digital detector input as:

$$\begin{aligned} y(t_m) &= p_R * e(t) + p_R * \eta(t)|_{t=t_m} \\ &\approx \sum_{k=-\infty}^{\infty} \sum_{n=1}^N a_n(m\tilde{T}) x_{\text{RC}}((m - k)\tilde{T} - \tau_n) \tilde{s}_k + p_R * \eta(m\tilde{T}), \quad (3.3) \end{aligned}$$

where $\{\tilde{s}_k\}$ denotes the zero-filled symbol sequence of Equation 2.8. This is the foundational equation for the QMFS. It is implemented in the simulations. It determines what estimates of the channel functions are possible. To this end, observe the business part of Equation 3.3 may be written as a

discrete convolution

$$\begin{aligned}
e(t_m) &\approx \sum_{k=-\infty}^{\infty} \sum_{n=1}^N a_n(m\tilde{T}) x_{\text{RC}}((m-k)\tilde{T} - \tau_n) \tilde{s}_k \\
&= \sum_{k=-\infty}^{\infty} h_B(m, k) \tilde{s}_{m-k}.
\end{aligned}$$

Thus, the *baseband digital Input Delay-Spread function* for the QMFS is

$$h_B(m, k) = \sum_{n=1}^N a_n(m\tilde{T}) x_{\text{RC}}(k\tilde{T} - \tau_n). \quad (3.4)$$

Sampling: Equation 3.4 shows the sampling requirements for channel estimation (See Staley [82] for an in-depth treatment of this topic). Resolution of the Doppler frequencies requires $1/\tilde{T} > 2f_D$, where f_D denotes the maximal spectral extent of the $\{a_n(t)\}$'s. Resolution of the raised-cosine filter requires $1/\tilde{T}$ exceed $(1 + \beta)/T$, where β denotes the *rolloff factor* [63, page 553]. Thus, the sampling rate should exceed

$$\frac{1}{\tilde{T}} = \frac{O_s}{T} \geq \max \left\{ \frac{1 + \beta}{T}, 2f_D \right\}. \quad (3.5)$$

3.5 Digital Channel Functions

At best, we will only have the digital channel functions in our hands but want the continuous channel functions and their covariances. This section uses the digital Input Delay-Spread function $h_B(m, k)$ to estimate the scattering function. Apply the Fourier transform along the columns of Equation 3.4 to get the digital Delay-Doppler function

$$\begin{aligned}
U_B(f, k) &= \sum_{m=-\infty}^{\infty} e^{-j2\pi f m \tilde{T}} h_B(m, k) \\
&= \sum_{n=1}^N x_{\text{RC}}(k\tilde{T} - \tau_n) \sum_{m=-\infty}^{\infty} e^{-j2\pi f m \tilde{T}} a_n(m\tilde{T}) \\
&= \sum_{n=1}^N x_{\text{RC}}(k\tilde{T} - \tau_n) \hat{a}_n(f).
\end{aligned}$$

The last equality follows from the sampling requirements of Equation 3.5. Comparing with $U(f, \tau)$ in Equation 3.2, this result shows that $U_B(f, k)$ is smeared by the raised cosine filter:

$$U_B(f, k) = x_{\text{RC}} *_{\tau} U(f, k\tilde{T}).$$

Its covariance is likewise smeared by a 2D raised cosine filter:

$$\begin{aligned} R_{U_B U_B}(f, k; f', k') &= E[U_B(f, k) \overline{U_B(f', k')}] \\ &= \sum_{n=1}^N \sum_{n'=1}^N x_{\text{RC}}(k\tilde{T} - \tau_n) x_{\text{RC}}(k'\tilde{T} - \tau_{n'}) E[\hat{a}_n(f) \overline{\hat{a}_{n'}(f')}] \\ &= \sum_{n=1}^N x_{\text{RC}}(k\tilde{T} - \tau_n) x_{\text{RC}}(k'\tilde{T} - \tau_n) P_{a_n a_n}(f) \delta(f - f') \\ &= x_{\text{RC}} \otimes x_{\text{RC}} * R_{UU}(f, k\tilde{T}; f', k'\tilde{T}). \end{aligned}$$

3.6 QMFS Simulation Issues

The QMFS simulation is built around the digital baseband Input Delay-Spread function $h_B(m, k)$ of Equation 3.1. Assumptions B-1, B-2, B-3, B-4, and B-5' are in force. For simplicity, only two paths are used.

Transmit Sequence: The following MATLAB fragment generates a PN sequence $\{s_k\}$ of length K to be pushed through the channel. Chapter 5 discusses PN sequences.

```
% RF setup
Rb    = 4*64.e+003;    % Symbol Rate (bits/sec)
T      = 1/Rb;         % Symbol Duration (sec)
beta   = 0.5;          % Rolloff factor

% Generate PN sequence
K = input('Enter the number of symbols <128>: ');
if isempty(K); K = 128; end
s = pn_src(9,1041,1024,1);
s = s( 512 + [1:K] );
```


Zero-Fill: This sequence is zero-filled to give $\{\tilde{s}_k\}$ for convolution processing (Section 2.6).

```
% Generate zero-filled PN sequence for convolution
Os = input('Enter the oversample factor <2>: ');
if isempty(Os); Os = 2; end
sExt = [s zeros(K,Os-1)].';
sExt = sExt(:);
```

Channel and Receiver Times: We will need two time vectors: The first is `tC` which is the extent of the channel delays or the k 's. Here the extent is the time interval $[0, KT]$. The second is `tR` which is the extent of the receiver or the m 's. Here the extent is the time interval $[0, MT/O_s]$.

```
% Generate the time vectors
tC = (T/Os)*([1:(K*Os)]-1).';          % Channel's time extent
NtC = length(tC);
M = length(tC) + length(sExt) - 1;    % Receiver's time extent
tR = (T/Os)*([1:M]-1).';
```

QMFS Parameters: Two fading paths are simulated. Their delays τ_1 and τ_2 are listed in `tau`. Both $\{a_1(t)\}$ and $\{a_2(t)\}$ are generated by `fade01` discussed in Chapter 4. This function simulators a complex-valued, zero-mean, unit variance, Gaussian time series. Its power spectrum is Gaussian-shaped with equivalent with the maximal Doppler f_D .

```
% QMFS: Fading
tau = K*T[ 0.1; 0.3];                  % Time Delays (sec)
fD = [10; 10]                          % Gaussian Doppler (Hertz)
N = length(tau);                       % Number of paths
for n=1:N
    a(:,n) = fade01(M,fD(n),Rb);
end
a = detrend(a,0);
```

Transmission through the QMFS: The zero-filled sequence is pushed through each path. Here `rcosplt(t,T,beta)` is a function call to the raised cosine filter $x_{RC}(t)$. A loop is used to save memory.

```

y = zeros(M,1);
for n=1:N
    y = y + a(:,n) .* conv2(rcosplt(tC-tau(n),T,beta),sExt);
end

```

Additive Noise: Equation 2.7 shows the additive noise is colored by the square-root raised cosine filter. The call to `srcnoise(M,0s,T,beta)` returns a complex-valued, zero-mean, unit variance, Gaussian time series with the square-root raised cosine power spectrum. The SNR we use is the ratio of the minimum peak value of the matched pulses to the variance of the noise.

$$\text{SNR} = \frac{\min\{|s_k x_{\text{RC}}(0)|^2\}}{\sigma_\eta^2} = \frac{1}{\sigma_\eta^2}.$$

```

% Channel Noise: Scaled at the receiver
SNR_dB = input('Enter SNR <20 dB>: ');
if isempty(SNR_dB); SNR_dB = 20; end
SNR      = 10^(SNR_dB/10);
nu        = srcnoise(M,0s,T,beta);

```

```

% Detector input: Unit variance noise is scaled to the SNR
y = y + nu/sqrt(SNR);

```

This completes the treatment of the QMFS and an elementary MATLAB implementation. *So what else does the user need to be aware of to setup a QMFS and make channel estimates?*

Mean, Variance, & Spectral Shape of $\{a_n(t)\}$: Covered in Chapter 4 for selected maritime channels.

Symbol & Fade Rates: The symbol rate must be at least the Nyquist rate of the fading process [13], [82]:

$$\frac{1}{T} \geq 2f_D.$$

Sequence & Channel Length: Standard estimators typically require at least as many symbols (length of **s**) as the channel (length of **h**). Longer soundings can reduce the noise and bias for a particular channel estimate but then run afoul of the time-varying channel.

Physical Arguments for selecting PMFS or QMFS: There are two main causes of fading in a wireless communication channel. First, of importance to mobile communications, is the fading caused by Doppler. Doppler fading is induced by changes in the relative path lengths of the multipath components. This type of fading is most directly described by the PMFS. That is, once the physical propagation environment is defined by the multipath structure given by the (a_n, f_n, τ_n) 's, the Doppler frequencies f_n are caused by the temporal deviation of the path lengths from the nominal values τ_n . This fading model describes a collection of stationary but scintillating reflectors. Once this environment is defined, the fading process develops in a deterministic fashion.

The second cause of fading is the time-varying nature of the propagation environment. For instance, as a receiver moves, a direct path may become obstructed and undergo severe diffraction loss or be shadowed completely. Likewise, a previously shadowed path may contribute significantly to the field if the receiver enters its line of sight. This type of fading also can occur if the transmitter and receiver are stationary and the propagation medium itself is varying, such as in an urban environment with automobile traffic or in an indoor scenario with moving people. The obstacles causing reflection and diffraction are constantly moving. This type of fading process is more adequately described by the QMFS. This model not only accommodates Doppler-induced fading, but also additional variations in the propagation environment through the random temporal variation of the $\{a_n(t)\}$'s. Consequently, the model choice should be determined from the physical RF environment. A maritime RF environment is the subject of the next chapter.

Chapter 4

A Surface Scatter Channel

The preceding chapters treated the two basic channel models. Chapter 2 showed that the phase-modulation fading simulator (PMFS) is specified by the distribution of the Doppler frequencies and the delays. Chapter 3 showed that the quadrature-modulation fading simulator (QMFS) is specified by the multiplicative noise $\{a_n(t)\}$ and delay τ_n for each path. For practical use, both models require an analysis of a communications channel to specify realistic distributions of the delays and Dopplers. This chapter adapts Bello's *surface scatter channel* to handle our needs for RF communications over water as shown in Figure 4.1.

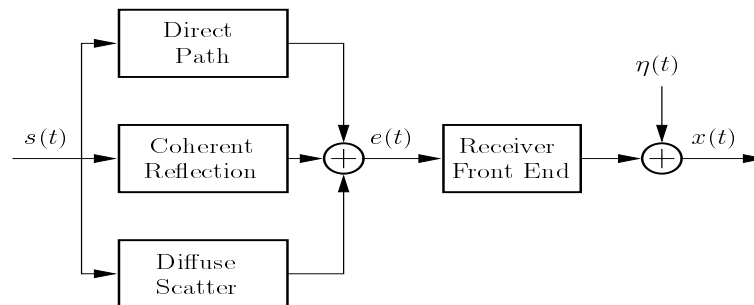


Figure 4.1: The subsystems modeling of the multiplicative noise for a surface scatter channel. From Bello (1973).

Bello's surface scatter channel is basic to over-the-water communications and also handles land mobile communications. It determines the Input Delay-Spread function $h(t, \tau)$ as [48], [8], [53]:

$$h(t, \tau) = \sqrt{P_0} \{L\delta(\tau - \tau_1) + \Gamma\delta(\tau - \tau_2) + g(t)\delta(\tau - \tau_3)\}. \quad (4.1)$$

Direct Path: The free-space power P_0 is reviewed in Section 4.2. Additional losses on the direct path are modeled by L . The line-of-sight (LOS) simulations take $L = 1$ although spherical diffraction simulations predict $L \ll 1$. The delay τ_1 is the time delay between the transmitter and the receiver.

Coherent Reflection: The coherent reflection coefficient Γ models the amplitude and phase modulation when a plane wave is reflected in the specular direction. The delay τ_2 is determined by the geometry of the transmitter and receiver. Both are reviewed in Section 4.3.

Diffuse Scatter: The multiplicative noise $\{g(t)\}$ models the diffuse scatter. It is a zero-mean, complex-valued Gaussian random process with spectral shape determined by the scattering and antennas. Its variance will be determined by the surface roughness. These are reviewed in Section 4.4.

Other Forms: This form of $h(t, \tau)$ in Equation 4.1 extends to other communication models. $\Gamma = 0$ is a common model for land-mobile communications or basic diffraction loss [9]. Loo & Secord [48] extend L to a log-normal process $\{L(t)\}$ which models fast fading due to foliage. North [56] extends L to include multiplicative noise on the direct and specular paths. Bello [6] remarks that Γ extends to a phase modulation process $\{\Gamma(t)\}$ to model fast specular fading.

Receiver Input: The input to the antenna due to the signal is

$$e(t) = \int_{-\infty}^{\infty} h(t, \tau)s(t - \tau)d\tau$$

and is scaled by the antenna gain and cable losses in the receiver's front end. The additive noise $\{\eta(t)\}$ is assumed be Gaussian with a flat spectrum over the bandwidth of the receiver's matched filter $p_R(t)$. Thus, $\{\eta(t)\}$ is determined by its variance σ_η^2 . Section 4.1 estimates σ_η^2 from standard RF noise sources.

This chapter is written so that a user can implement the model in Figure 4.1. To this end, we march through the parameters of Equation 4.1.

The receiver and transmitter geometry and the flat-earth propagation give general formulas for these parameters. These are specialized to a generic ship-to-shore simulation. Once this simulation is in place, we can ask the question: *How well does this model compare with more sophisticated propagation effects?* Indeed, some readers might find the surface-scatter model of Figure 4.1 too limiting. The final section of this chapter compares the propagation factor of the flat-earth model at $f_c=300$ MHz over water with a well-established PDE code. Both models agree in free space but boundary effects, such as the surface wave over water and local reflectors, are simply not included in the simpler flat-earth model.

4.1 Additive Channel Noise

Figure 4.2 presents a simplified front end of the receiver. The signal at the antenna $e(t)$ is scaled by the receiver's antenna gain G_R and cable losses at the receiver input. The additive channel noise $\{\eta(t)\}$ is attributed to the RF background and system noise at the receiver input. Thus, the receiver input is:

$$x(t) = G_R e(t) / L_{\text{cable}} + \eta(t).$$

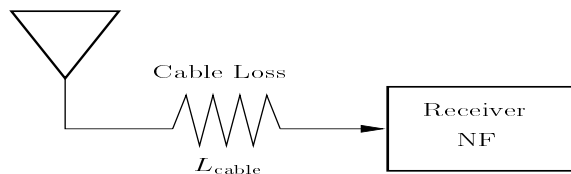


Figure 4.2: Receiver front end.

The noise is attributed to the RF background noise and system noise. It is generally taken to be zero-mean white Gaussian noise with flat spectrum [73, 236–257], [93, page 310], [8], [89], [17], [87]. By Baseband Assumption B-2, this channel noise is linearly demodulated, shaped by the receiver's matched filter $p_R(t)$, and then presented to the detector. Thus, the baseband noise $\{\eta(t)\}$ is complex-Gaussian with flat spectrum across the support of $p_R(t)$.

So only the variance σ_η^2 or in-band background noise power $P_\eta = \sigma_\eta^2$ is needed to completely specify $\{\eta(t)\}$. From [44, page 76]

$$P_\eta = \sigma_\eta^2 = kT_{\text{op}}B, \quad (4.2)$$

where k is Boltzmann's constant (1.38×10^{-23} W K⁻¹ Hz⁻¹), T_{op} denotes the effective operating temperature (K), and B is the bandwidth of $p_R(t)$ (Hz).

Bandwidth B : Baseband Assumption B-4 takes $p_R(t)$ to be the square-root raised cosine filter with roll-off factor β . In the frequency domain, $|\widehat{p_R}(f)|^2$ has support in the frequency interval [63, page 546]: $\pm(1 + \beta)/(2T)$. Then $B = (1 + \beta)/T$. Although the 3 dB bandwidth is $1/T$, we use the full frequency interval to measure noise power.

Equivalent Operating Temperature T_{op} : The literature on T_{op} is extensive and the excellent review by Pritchard [62] is adapted as follows. With respect to the input to the receiver, a simplified model for a whip antenna is

$$T_{\text{op}} = \{G_R T_{\text{sky}} + T_{\text{ant}}\}/L_{\text{cable}} + T_{\text{cable}}(1 - 1/L_{\text{cable}}) + T_{\text{rcr}}.$$

The thermal noise sources are the equivalent temperatures of the antenna T_{ant} , the cable T_{cable} , and the receiver T_{rcr} . The receiver's antenna gain G_R amplifies the RF noise from the sky T_{sky} . Figure 4.3 is adapted from Kim & Muehldorf [44, page 74] and gives T_{sky} as a function of frequency for RF noise sources.

4.2 Free-Space Path Loss

Basic to propagation is the *Friis free-space transmission formula*. Mathematically, we set $L = 1$, $\Gamma = 0$, and $\sigma_g^2 = 0$ in Equation 4.1. Physically, a transmitter with input power P_T and antenna gain G_T is broadcasting into free-space at wavelength λ . At a distance r , the receiver intercepts the radiated power with antenna gain G_R equal to the directivity. The ratio of the received free-space power P_0 to the transmitted power P_T is [12], [93, page 68], [9, page 26], [44, page 239]

$$G_0 = \frac{P_0}{P_T} = G_T G_R \left(\frac{\lambda}{4\pi r} \right)^2. \quad (4.3)$$

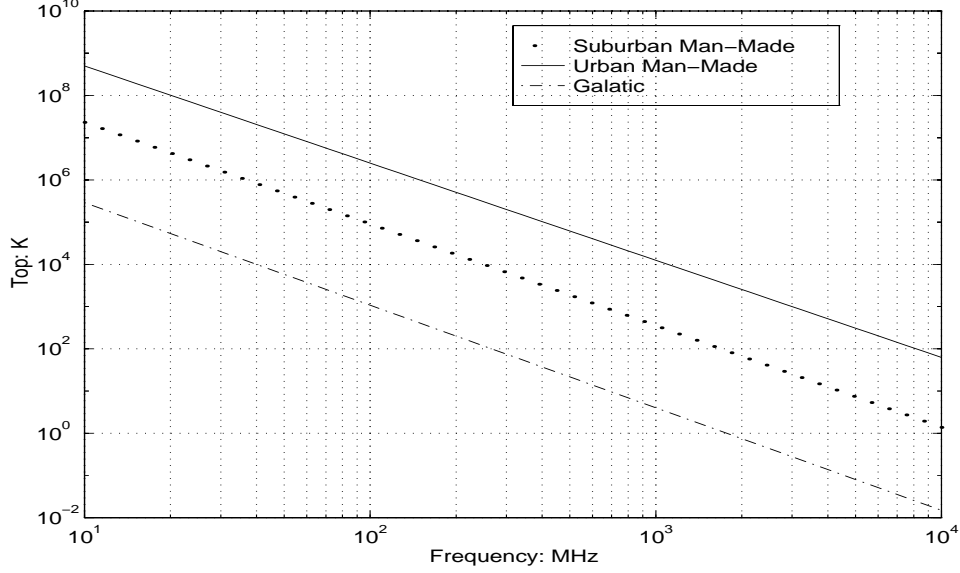


Figure 4.3: Sky temperatures T_{sky} (Kelvins) due to background noise sources. From Kim & Muehldorf (1995).

4.3 The Flat-Terrain Path-Loss Model

Figure 4.4 illustrates the setup for the Flat-Terrain Path Loss Model [93]. A transmitter with antenna height h_T and antenna gain G_T is separated by distance d from the receiver with antenna height h_R and antenna gain G_R . Two paths are to carry the signal: (i) The direct path which follows the free-space model. (ii) The coherent or indirect path with reflection coefficient Γ relating terrain “smoothness” and the wavelength λ . A standard factorization for Γ is [6], [61, pages 19–22], [93, pages 69–71] [47, page 95–125]

$$\Gamma = \Gamma_0 D \mathcal{R}. \quad (4.4)$$

Divergence: The divergence D is [47, page 98] “equivalent to a purely geometric factor that describes additional spreading of a beam of rays due to reflection from a spherical surface” and has values between 0 and 1. A flat earth sets $D = 1$.

Plane Surface Reflection Coefficient: Γ_0 denotes the reflection coefficient for a plane surface of the same material. For vertical polarization, [47, page 99],

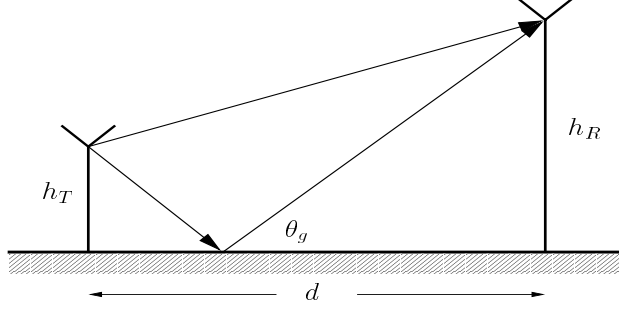


Figure 4.4: Direct and reflected path in the Flat-Terrain Path Loss Model. The grazing angle is denoted by θ_g .

[9, page 53]

$$\Gamma_0 = \frac{\epsilon \sin(\theta_g) - \sqrt{\epsilon - \cos(\theta_g)^2}}{\epsilon \sin(\theta_g) + \sqrt{\epsilon - \cos(\theta_g)^2}}, \quad (4.5)$$

where the grazing angle is

$$\theta_g = \arctan\left(\frac{h_T + h_R}{d}\right), \quad (4.6)$$

and ϵ is the complex permittivity of the terrain. Figure 4.5 plots Γ_0 for sea water and vertical polarization as a function of the grazing angle.

Roughness Coefficient: The roughness coefficient \mathcal{R} was developed from experimental observations of Beard, Katz, and Spetner [2], [42], [1] and compares well with other work [47, page 122–125]. We use the modified version [9, Equation 2.62]

$$\mathcal{R} = e^{-\mathbf{g}^2/2} I_0(\mathbf{g}^2/2), \quad (4.7)$$

where \mathbf{g} is the “electrical roughness parameter” [6]

$$\mathbf{g} = \frac{4\pi\Delta h \sin(\theta_g)}{\lambda}, \quad (4.8)$$

and Δh denotes the standard deviation of the height fluctuation of the surface. Parsons [61, page 59] tabulates Δh for selected terrains. Long [47, page 50–54] tabulates the (peak-to-peak) wave heights for various sea states and conveniently relates Δh to the various wave-height measurements.

Time Delays: With the speed of propagation given by c , the direct path’s time delay is

$$\tau_1 = c^{-1} \sqrt{d^2 + (h_R - h_T)^2}. \quad (4.9)$$

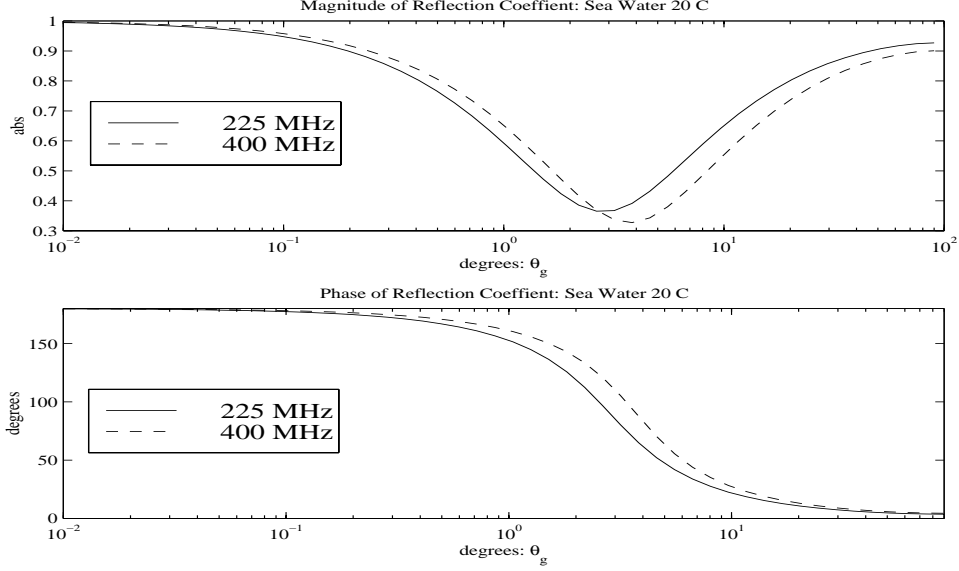


Figure 4.5: Magnitude and phase of the reflection coefficient Γ_0 for sea water at 20° C and vertical polarization as a function of the grazing angle θ_g . Here $\epsilon = 70 - j300/\lambda$.

The reflected path's time delay is

$$\tau_2 = c^{-1} \sqrt{d^2 + (h_R + h_T)^2}. \quad (4.10)$$

Phase Delays: For each frequency, the direct and reflected signals combine at the receiver. The longer path of the reflected signal induces a phase delay $\Delta\phi$ given by [93, page 70]:

$$\Delta\phi = 2\pi f_c(\tau_2 - \tau_1) \quad (4.11)$$

or to avoid subtractive cancellation,

$$\Delta\phi = \frac{2\pi}{\lambda} \frac{4h_T h_R}{\sqrt{d^2 + (h_T + h_R)^2} + \sqrt{d^2 + (h_T - h_R)^2}}.$$

For narrow-band signals, it is standard to approximate the effect of the direct and reflected paths with a phase delay. Mathematically, the claim is [93]

$$h(t, \tau) = \sqrt{P_0} \{ \delta(\tau - \tau_1) + \Gamma_0 \delta(\tau - \tau_2) \} \approx \sqrt{P_0} \{ 1 + \Gamma_0 e^{+j\Delta\phi} \} \delta(\tau - \tau_1).$$

4.4 Multiplicative Noise

This section presents straight-forward implementations of a few well-known stochastic models for the diffuse scattering or the fast fading process $\{g(t)\}$. These models are appropriate for narrow-band systems such as military communication channels. The random processes $\{g(t)\}$ is typically a narrow-band Gaussian random process with *spectral shape* determined by the antennas and multipath and *spectral extent* determined by the maximum Doppler frequency f_D .

This process arises because the channel between the source and receiver is time-variant. For example, consider the LOS propagation model in Section 4.3. Suppose a ground vehicle is situated in an urban coastal region and transmitting to a ship or surveillance aircraft. Transmissions from its whip antenna radiate uniformly in azimuth and strike a number of nearby reflectors. Some of these reflectors bounce the signal to the distant ship or aircraft. The geometry of the vehicle, the reflectors, and the receivers determine the multiple paths for the signal to arrive at the receiver. The variable path lengths induce relative phase delays which may cause signal cancellation [61, page 111]: “when either the transmitter or the receiver is in motion, we have a ‘dynamic multipath’ situation in which there is a continuous change in the electrical length of every propagation path and thus the relative phase shifts between them change as a function of spatial location . . . the space-selective fading which exists as a result of multipath propagation is experienced as time-selective fading by a mobile receiver which travels through the field.” Table 4.1 lists M files which simulate $\{g(t)\}$. We make explicit that `fade02.m` and `fade03.m` have been adapted from Richard North’s *NRaD’s Communication Toolbox* [55].

Table 4.1: Narrow-Band Gaussian Processes

M file	$R_{gg}(\tau)$	Application	References
<code>fade01.m</code>	Gaussian	air-to-air, air-to-satellite	[6], [8], [35] [53] [89]
<code>fade02.m</code>	Bessel	land mobile whip antenna	[93, page 150], [61, page 177]
<code>fade03.m</code>	Butterworth	land mobile satellite	[48], [51] [51]

fade01: Simulates the Gaussian process $\{g(t)\}$ with correlation [6], [8]

$$\rho_{gg}(\tau) = \frac{R_{gg}(\tau)}{R_{gg}(0)} = e^{-(\pi f_D \tau)^2},$$

where f_D denotes the maximal Doppler frequency [93, page 128]

$$f_D = \frac{v}{\lambda},$$

v denotes the radial speed between the transmitter and the receiver, and the carrier wavelength is denoted by λ . This fading model is appropriate for air-to-satellite links [6], [53], [8] or air-to-air links [35].

fade02: Simulates the Gaussian process $\{g(t)\}$ with a Bessel function for its correlation. In terms of its normalized power spectrum [61, page 117], [93, page 150]

$$P_{gg}(f) = \begin{cases} (1 - (f/f_D)^2)^{-1/2} & |f| < f_D \\ 0 & \text{elsewhere} \end{cases}.$$

This fading model is commonly used for land-mobile links. Parsons [61, pages 114-120] has a fine discussion remarking that this spectrum is the result of assuming the multipaths are distributed around a vertical whip antenna uniformly in azimuth but with zero elevation. Allowing a small variance in elevation rolls off the poles.

fade03: Simulates the Gaussian process $\{g(t)\}$ with a Butterworth function for its normalized power spectrum [48]

$$P_{gg}(f) = \begin{cases} (1 + (f/f_D)^{2k})^{-1} & |f| < f_D \\ 0 & \text{elsewhere} \end{cases}.$$

Loo & Secord [48] use this fading model for both multiplicative and the log-normal noise for their land-mobile satellite links in the L band. They claim that a fast fading log-normal process is needed to model the effects of foliage near the transmitter. To simulate the fast fading log-normal process, they simply exponentiate the output of **fade03**. This fast fading applies to carrier frequencies above VHF. It remains to determine reasonable ranges for the variance of $\{g(t)\}$. Not surprisingly, it depends on the propagation environment.

Land Mobile Communications: A typical setup for land mobile communications is to assume that no specular channel exists. That is, $\Gamma=0$. Thus, the probability density function of $\{|a(t)|\}$ is Ricean and described by the ratio K of the direct to diffuse power [61, page 135]. Parsons [61, page 209] tabulates K for various terrains.

Aeronautical Channel: Figure 4.1 provides the model for the Input Delay-Spread function of an aeronautical channel:

$$h(t, \tau) = \sqrt{P_0} \{ \delta(\tau - \tau_1) + \Gamma \delta(\tau - \tau_2) + g(t) \delta(\tau - \tau_3) \}.$$

The reflection coefficient and delay are determined in Section 4.3 while $\{g(t)\}$ is given by `fade01.m`. The problem is to determine σ_g . We assume the divergence $D = 1$. Beard, Katz, and Spetner [2], used the aeronautical channel model to obtain estimates of σ_g . They reported $\sigma_g/|\Gamma_0|$ was approximately constant as a function of the electrical roughness parameter and was bounded between 0.2 and 0.4. However, additional measurements reported by Beard [1] in 1961 showed $\sigma_g/|\Gamma_0|$ was not constant. Although Bello [6] in 1975 developed approximations to this ratio, Ryan¹ argues from conservation laws that

$$\sigma_g = G_f |\Gamma_0| \sqrt{1 - \mathcal{R}^2}, \quad (4.12)$$

where G_f denotes the “forward-scatter” gain which has a maximal value of $1/\sqrt{2}$. This corresponds to receiving the entire forward hemisphere on the diffuse channel. The simulations will set G_f to agree with measured mean values of approximately 0.33 so that $G_f = 0.66$.

4.5 Ship-to-Shore

The preceding discussion is summarized in a ship-to-shore simulation adapted from [56]. The goal is to parameterize the Input Delay-Spread function of Equation 4.1 as:

$$h(t, \tau) = \sqrt{P_0} \{ L \delta(t - \tau_1) + [\Gamma_0 \mathcal{R} e^{+j\Delta\phi} + g(t)] \delta(t - \tau_2) \},$$

and the associated SNR for scaling the additive noise $\{\eta(t)\}$. Specifically, a naval ship is operating within line-of-sight (LOS) of a coastal city. The ship

¹Frank J. Ryan [1996]: Personal communication.

transmits at $f_c=300$ MHz to a receiver positioned on bluffs 350 feet above the shoreline. Consulting [44, Table 1.1], we see that the Flat-Terrain Model from Section 4.3 applies and the geometry follows Figure 4.4.

Table 4.2 lists the relevant physical parameters. The antenna height h_T is taken from [44, page 202]. The receiver height h_R is taken to be the height of the bluffs. The total horizon range is 35 nm [43, page 115], so the separation $d=10$ nautical miles insures both ship and shore are in sight of each other. For ship-to-shore communications, assume an AN/WSC-3(V)6 radio is used on this LOS link at $f_c=300$ MHz [44, page 213]. Assume both receiver and transmitter antenna have 0 dB gain (adapted from [44, page 203]) and vertical polarization. The results are highlighted in the following paragraphs and summarized in Table 4.3.

Table 4.2: Ship-to-Shore Parameters

Parameter	Symbol	Value
Ship: antenna height	h_T	100 feet
gain	G_T	0 dB
power	P_T	100 Watts
Shore: antenna height	h_R	350 feet
gain	G_R	0 dB
Separation	d	10 nautical miles
Carrier frequency	f_c	300 MHz
Bandwidth	B	25 kHz
Receiver Noise Figure	NF	8 dB
Cable Loss	L_{cable}	5 dB
Cable Temperature	T_{cable}	290 K
Polarization		vertical
Roll-off factor	β	0.5

The Reflected Path: Equation 4.10 gives the reflected delay:

$$\tau_2 = \sqrt{d^2 + (h_T + h_R)^2} = \tau_1 + 0.001$$

which sets the phase shift $\Delta\phi=126$ degrees (Equation 4.11). The grazing angle is $\theta_g=0.3772$ degrees and the reflection coefficient is

$$\Gamma_0 = 0.8160\angle -170.7^\circ.$$

This is slightly reduced by the roughness coefficient. Sea-State 2 sets the “1/3 wave height” $h_{1/3}=2$ feet [47, page 50-54]. Equations 4.7 and 4.8 determine the roughness coefficient $\mathcal{R}=0.9999$.

The Fading Component: Section 4.4 sets the diffuse component $\{g(t)\}$ to a zero-mean, complex-valued, Gaussian random process with power spectrum proportional to $\exp(-\{\pi f/f_D\}^2)$. The Doppler f_D is estimated to be 10 Hz [55]. Equation 4.12 sets $\sigma_g=0.0076$. Thus, the relatively smooth sea and small grazing angle produce specular rather than diffuse reflection.

The Noise: An urban environment at $f_c=300$ MHz sets the sky temperature $T_{\text{sky}} \approx 10^5$ (K). The receiver temperature is $T_{\text{rcr}} = (10^{\text{NF}/10} - 1) \times 290 = 1540$ (K). Then the link budget for the operating temperature is

$$\begin{aligned} T_{\text{op}} &= \{G_R T_{\text{sky}} + T_{\text{ant}}\}/L_{\text{cable}} + T_{\text{cable}}(1 - 1/L_{\text{cable}}) + T_{\text{rcr}} \\ &= \{199822 + 100\}/2.95 + 290 \times 0.6612 + 1540 \\ &= 69474 \text{ [K]}. \end{aligned}$$

Thus, the sky noise due to the urban environment dominates the noise and sets the additive noise power $P_\eta=-136$ (dB).

Table 4.3: The surface scatter parameters for the ship-to-shore simulation: The $\text{SNR}=P_R/P_\eta=53$ dB at the receiver input.

Symbol	Value
L	1
P_R	-83 dB
P_η	-136 dB
τ_1	61.73 μs
$\tau_2 - \tau_1$	1 ns
Γ_0	$0.8160\angle -170.6802^\circ$
$\Delta\phi$	126.4°
σ_g	0.0076
f_D	10 Hz

Table 4.3 completes the immediate goal of this chapter. But is it worthwhile to step back and consider a “global” view of how the signal power

is arriving at the receiver's antenna. Specifically, we examine the free-space gain G_0 . Figure 4.6 shows how this gain distributes in range and elevation. The reader can see several lobes present in the cross section as a function of elevation. The lobing is called the “Lloyds Mirror” effect and results from the interference of the direct and reflected wave. With this picture in mind, we return to the question raised at the beginning of this chapter: *How well does this scattering model reflect real-world propagation?* The final section is devoted to this problem.

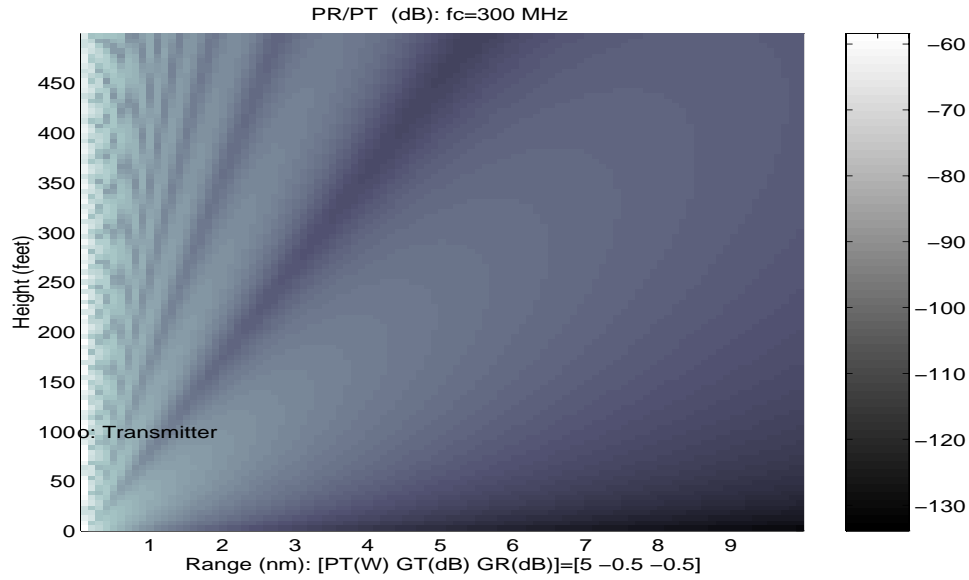


Figure 4.6: Two-path model of propagation gain P_R/P_T from an antenna at $h_T=100$ foot transmitting at $f_c=300$ MHz over water (Sea State 2). Isotropic antenna pattern.

4.6 Propagation Issues: Ship-to-Shore

There is a huge literature on propagation. Brayer in 1975 [10] and Goldberg in 1976 [30] are both substantial collections of classic papers. Parsons [61], Yacoub [93], and Boithias [9] are more recent references that summarize much of the engineering or ray-tracing approach to propagation modeling. This approach models the paths from the transmitter and receiver. A standard

list for LOS propagation includes the following: Direct Path; Reflected Path; Sky Wave; Troposcatter; Surface Wave; Secondary Surface Effects; Terrain Effects;

For a ship-to-shore simulation, $f_c=300$ MHz and $d=10$ nm precludes the need to model the sky wave [44, pages 157–163]. Likewise, the close range permits us — in theory — to neglect the troposcatter [5]. However, the surface wave and terrain effects cannot be ignored. To see this, the reader is asked to compare the propagation factor P_R/P_0 for two simulations. This factor is the effect due solely to the reflections and not the free-space loss.

Figure 4.7 shows the estimated propagation factor for the ship-to-shore simulation computed using from the two-path model. Figure 4.8 shows the propagation factor essentially for the same setup but computed using the VTRPE code [70]. Recall that the shore site is on high cliffs overlooking the ocean. The VTRPE simulation includes these shore cliffs. It also includes a dipole antenna pattern. Away from the terrain, the free-space structure of these two propagation factors agree. However, the reader can see a strong surface wave present in the VTRPE simulation and non-trivial scattering at the edge of the cliff. The surface wave is important for maritime RF applications. The scattering at the edge of the cliff is critical for site placement. These plots argue that RF mission planners handling propagation effects with simple models or their “tweaked-up” versions are omitting non-trivial phenomenon affecting mean power levels.

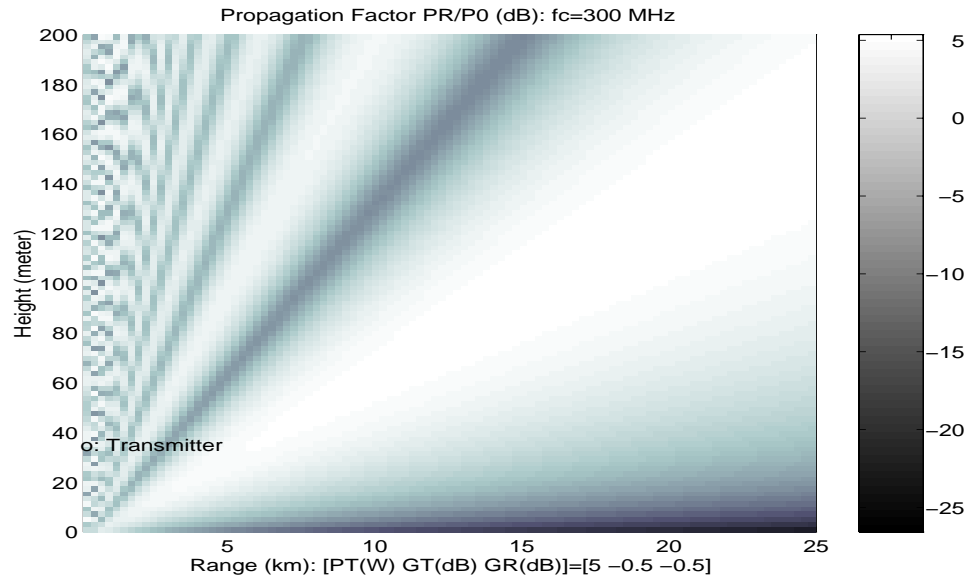


Figure 4.7: Two-path model of the propagation factor P_R/P_0 from an antenna at $h_T=100$ foot transmitting at $f_c=300$ MHz over water (Sea State 2). Isotropic antenna pattern.

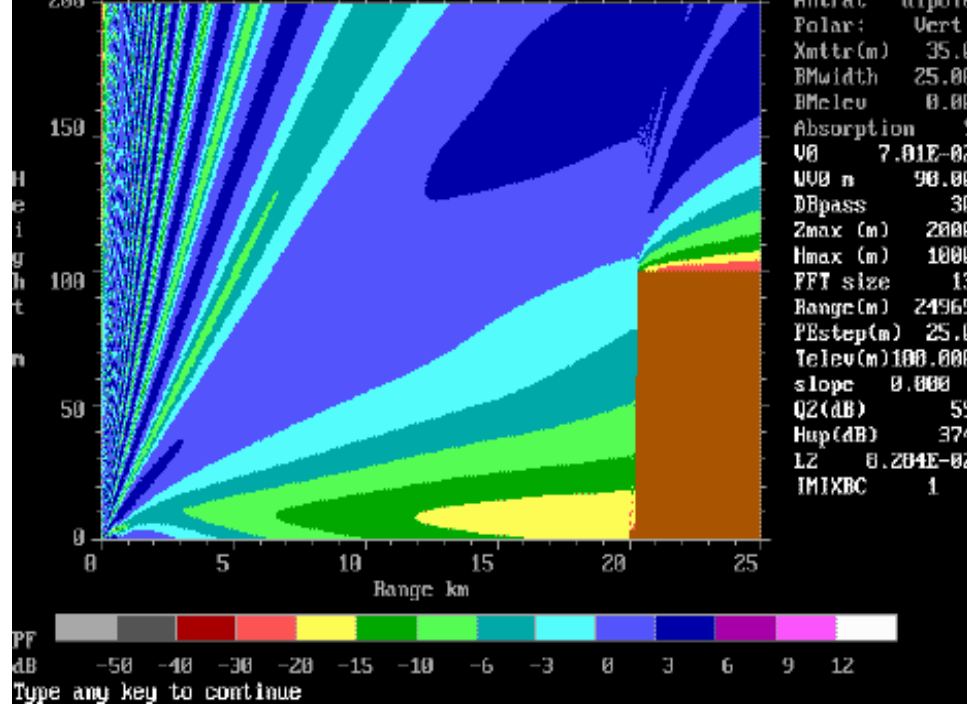


Figure 4.8: VTRPE's propagation factor P_R/P_0 : Antenna at $h_T=100$ foot transmitting at $f_c=300$ MHz, vertical polarization, over sea water. Isotropic antenna pattern.

Chapter 5

Channel Estimation: Sequence Methods

The preceding chapters demonstrated that the quadrature-modulation fading simulator (QMFS) is an acceptable channel model. The QMFS with Baseband Assumptions B-1, B-2, B-3, B-4, and B-5 (See Chapter 3) produced the following digital approximation of a signal received through the QMFS. This model is given in Equation 3.3 and reproduced here for the reader's convenience:

$$y(t_m) = \sum_{k=-\infty}^{\infty} h_B(m, k) \tilde{s}_{m-k} + \nu(t_m).$$

The received digital signal $\mathbf{y} = [y(t_m)]$ is sampled at time instants

$$t_m = m\tilde{T} = \frac{T}{O_s},$$

where O_s is the oversampling rate. The baseband digital Input Delay-Spread function

$$h_B(m, k) = \sum_{n=1}^N a_n(m\tilde{T}) x_{\text{RC}}(k\tilde{T} - \tau_n) \quad (5.1)$$

is convolved with the zero-filled signal $\mathbf{s} = [\tilde{s}_k]$, and corrupted by additive noise $\mathbf{v} = [\nu(t_m)]$ where $\nu(t) = p_R * \eta(t)$. *The channel estimation problem is to recover $h_B(m, k)$ from \mathbf{y} and \mathbf{s} .*

In matrix form, the channel system can be written as

$$\mathbf{y} = H_B \mathbf{s} + \mathbf{v},$$

where $H_B = [h_B(m, m - k)]$. Suppose H_B was not so constrained. Then for a non-trivial input vector \mathbf{s} , we have an underdetermined system in the unknown matrix H_B . Either no solution exists or an infinite number of solutions are available. Without modeling assumptions to constrain H_B , we could simply offer a scaled version of $\mathbf{y}\mathbf{s}^H$ as a solution for H_B and close this chapter. The problem with that solution is that it is not constrained by the QMFS model specified by h_B in Equation 5.1. More generally, all channel estimation schemes make some model assumptions — explicit or otherwise — to constrain H_B .

A common constraint is to claim the channel is (locally) time-invariant. This forces H_B to be Toeplitz and we get a convolution:

$$\mathbf{y} = \mathbf{s} * \mathbf{h} + \mathbf{v}.$$

Given the input signal \mathbf{s} and the output \mathbf{y} , the problem is to recover $\mathbf{h} = [h_B(k)]$. It goes without saying that there exists an enormous and expanding literature on this problem. This chapter uses a simple analytic framework that includes both the standard PN processing and more recent extensions to channel estimation.

The baseline PN processing is the simple and robust autocorrelation. With $\mathbf{w} = \text{flipud}(\mathbf{s})/\langle \mathbf{s}, \mathbf{s} \rangle$, the correlation function of \mathbf{s} may be written as

$$\rho_{\mathbf{s}\mathbf{s}}(k) = \frac{R_{\mathbf{s}\mathbf{s}}(k)}{R_{\mathbf{s}\mathbf{s}}(0)} = \mathbf{w} * \mathbf{s}.$$

The digital channel estimate is then

$$\mathbf{h}_{\text{PN}} = \mathbf{w} * \mathbf{y} \approx \mathbf{h}$$

because $\rho_{\mathbf{s}\mathbf{s}} \approx \delta$ for PN sequences. *This approximation “ \approx ” is the crux of the problem for channel estimation* and has spawned a cottage industry in the manufacture of “optimal” sequences. The Gauss-Markov (GM) theory (See Appendix 5.2) provides an analytical framework to handle this approximation. Section 5.1 reviews our baseline PN processing. Section 5.2 presents a Gauss-Markov estimator. Section 5.3 presents a Minimum-Variance (MV) estimator. For comparison, a simple, time-invariant channel is carried through these sections.

Because these simulations are time-invariant, a good question is the following: *How do these estimators perform on time-variant channels?* The

problem with this worthy question is that it focuses on baseband channel simulations. In Chapter 7, these estimators are coupled with a demodulator to process RF data. We will see that the demodulation scheme must also be considered part of the estimator and that its effects swamp the problem of time invariance. Section 5.4 closes with a review of the literature.

5.1 PN Processing

Our baseline channel estimation scheme is the standard PN processing. Viterbi [90] has a fine exposition on PN sequences and maximal length linear shift register (MLSR) sequences. A pseudorandom $\{0, 1\}$ sequence should exhibit three “randomness” properties [90, page 12]

- R.1** Relative frequencies of 0 and 1 are $1/2$.
- R.2** Run lengths of 0’s and 1’s are as a coin flipping experiment; $1/2$ of all run lengths are 1; $1/4$ are length 2; $1/8$ are length 3;
- R.3** If the random sequence is shifted by any non-zero number elements, the resulting sequence will have an equal number of agreements with and disagreements with the original sequence

For an MLSR sequence of length P , Viterbi concludes “that with the slight unbalance of $1/P$. . . , an MLSR sequence is indistinguishable from a Bernoulli or ‘coin-flipping’ binary sequence, at least with respect to randomness properties (R.1) through (R.3), as long as the initial vector or time is chosen randomly. In all that follows, we shall treat MLSR and coin-flipping sequences interchangeably.” To facilitate comparisons between the various channel estimators, the following time-invariant channel is offered as an example.

Example 5.1.1 (A “Leaky” Channel) This baseband time-invariant channel is rigged to show “sidelobe leakage” with minimal assumptions. An $N_s=511$ -point PN sequence \mathbf{s} is generated by the call to `pn_src(9, 1041, N_s , 1)`. Figure 5.1 plots the sample correlation function

$$\rho_{ss}(k) = \frac{R_{ss}(k)}{R_{ss}(0)}.$$

The two largest sidelobes of the correlation function are marked with circles and determine the τ_n 's. The sign of the delays is chosen to cause maximal cancellation at the first reflector. We assume the sample increment T matches the symbol rate. That is, there is no oversampling ($O_s=1$) so the raised-cosine filters needs only “0” or “1” values. The channel \mathbf{h} is shown in Figure 5.2. Our digital model takes the form

$$\mathbf{y} = \mathbf{s} * \mathbf{h} + \mathbf{v} = \text{conv}(\mathbf{s}, \mathbf{h}) + \mathbf{v},$$

where the receiver noise \mathbf{v} is IID Gaussian because $O_s = 1$ (See Appendix D). For ease of examining the plots, the reflector coefficients have magnitude 1. This makes the channel “active” with a gain of 3. To compensate, the noise level set from Equation 2.12 is modified as follows:

$$\text{SNR} = 10 \log_{10} \left(\frac{3^2}{\sigma_{\mathbf{v}}^2} \right).$$

The PN channel estimate is

$$\mathbf{h}_{\text{PN}} = \text{conv}(\text{flipud}(\mathbf{s}), \mathbf{y}) / N_{\mathbf{s}}.$$

Figure 5.3 compares the magnitudes of the channel \mathbf{h} and \mathbf{h}_{PN} and shows the magnitude of the first delay is degraded by the sidelobe leakage. \square

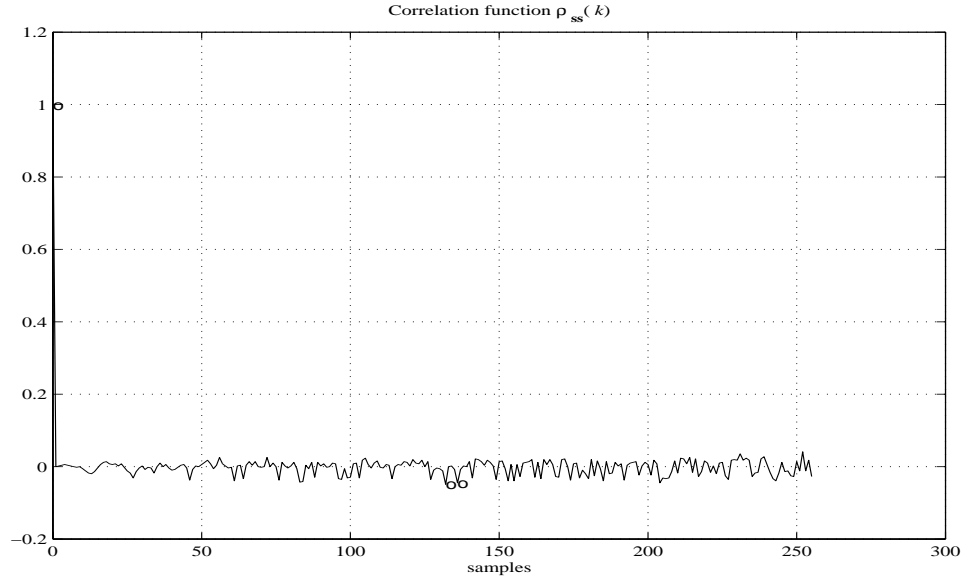


Figure 5.1: Sample correlation function $\rho_{ss}(k)$ for the PN sequence $s = \text{pn_scr}(9, 1041, 511, 1)$. The circles mark the delay times in the channel.

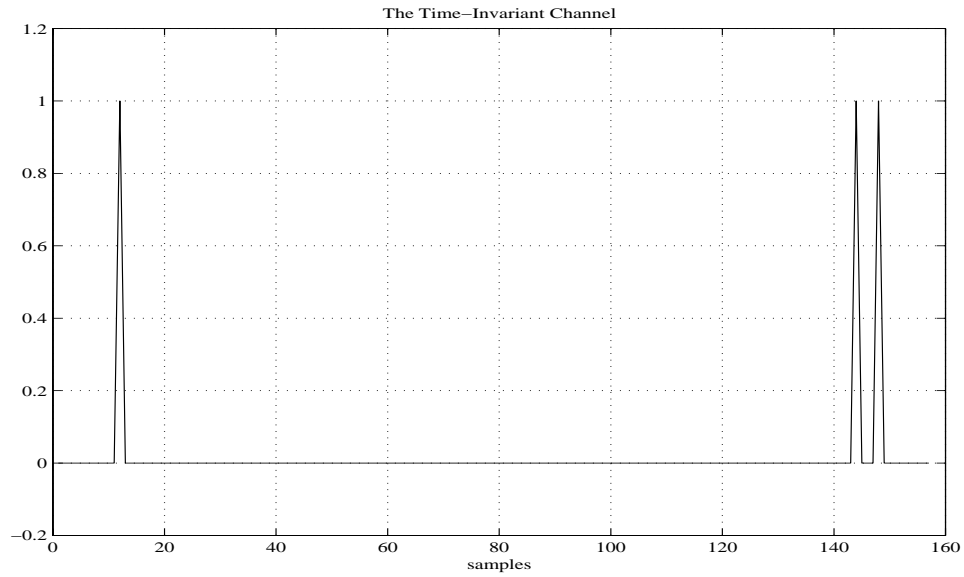


Figure 5.2: The channel function \mathbf{h} rigged for maximal leakage into the first reflector.

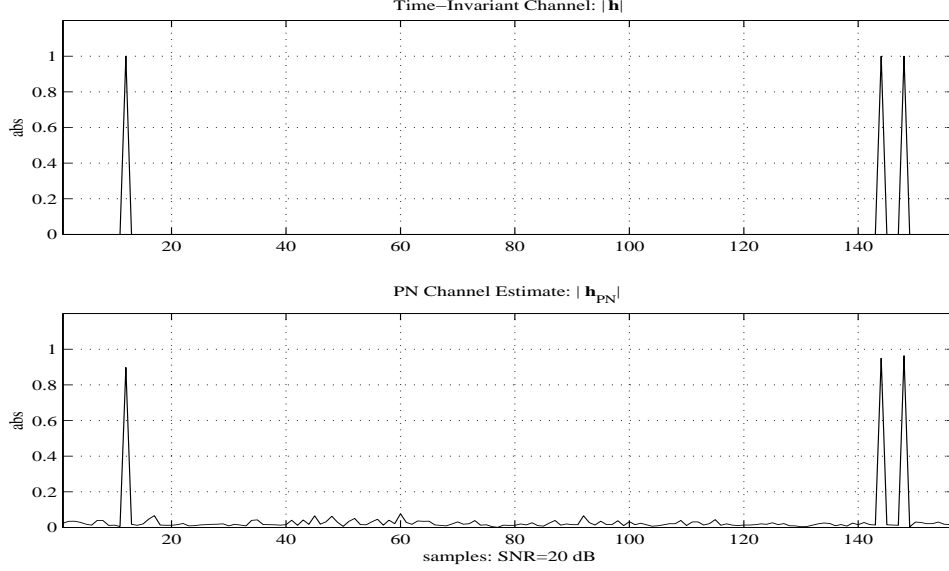


Figure 5.3: Upper Panel: The time-invariant channel magnitude $|\mathbf{h}|$. Lower Panel: The PN-estimate $|\mathbf{h}_{\text{PN}}|$ showing the side-lobe leakage degrading the estimate of the first reflector.

Given this leakage, it is natural to ask: *How long does the PN sequence need to be to reduce this leakage?* Write the time-invariant channel as a linear system

$$\mathbf{y} = \mathbf{s} * \mathbf{h} + \mathbf{v} = C_{\mathbf{s}} \mathbf{h} + \mathbf{v},$$

where $C_{\mathbf{s}}$ denotes the convolution matrix determined by \mathbf{s} . We can generate $C_{\mathbf{s}}$ in MATLAB as

$$C_{\mathbf{s}} = \text{conv2}(\text{eye}(\text{length}(\mathbf{h})), \mathbf{s}) = \text{convmtx}(\mathbf{s}, \text{length}(\mathbf{h})).$$

Elementary bounds on the bias and the variance for any linear estimator are obtained next.

Lemma 5.1.1 *Assume \mathbf{s} and \mathbf{h} are fixed vectors of length $N_{\mathbf{s}} \geq N_{\mathbf{h}}$. Assume \mathbf{v} is a zero mean noise vector with covariance $R_{\mathbf{v}\mathbf{v}} = E[\mathbf{v}\mathbf{v}^H]$. Assume the linear system*

$$\mathbf{y} = C_{\mathbf{s}} \mathbf{h} + \mathbf{v}$$

admits an approximate left-inverse W :

$$WC_{\mathbf{s}} = I + R,$$

where R will be called the residual matrix. The estimate \mathbf{h}_W of \mathbf{h} has the form

$$\mathbf{h}_W = \mathbf{h} + R\mathbf{h} + W\mathbf{v}.$$

The bias is

$$\text{Bias}[\mathbf{h}_W] = E[\mathbf{h}_W - \mathbf{h}] = R\mathbf{h}.$$

The covariance is

$$\text{Cov}[\mathbf{h}_W] = WR_{\mathbf{v}\mathbf{v}}W^H.$$

If R is pointwise bounded: $|R(m, n)| \leq \rho_{\max}$ then

$$(a) \quad \|\text{Bias}[\mathbf{h}_W]\|_2 \leq \|R\| \|\mathbf{h}\|_2 \leq \rho_{\max} N_{\mathbf{h}} \|\mathbf{h}\|_2.$$

$$(b) \quad \|\text{Bias}[\mathbf{h}_W]\|_{\infty} \leq \rho_{\max} \|\mathbf{h}\|_1.$$

Lemma 5.1.1 shows that the mean-square error in \mathbf{h}_W arises from the bias and the variance:

$$E[\|\mathbf{h}_W - \mathbf{h}\|_2^2] = \|R\mathbf{h}\|_2^2 + \text{trace}[WR_{\mathbf{v}\mathbf{v}}W^H].$$

It is the bias that causes the sidelobe leakage. The bias can be set to zero by setting W to a left inverse — which may induce an excessive variance. This variance can be made small by setting W to zero — giving a rather biased estimate. The problem is to find an optimal trade-off between the bias and the variance. This leads to some fascinating optimization problems for our channel estimators. The PN estimator uses the “matched filter”:

$$\mathbf{h}_{\text{PN}} = W\mathbf{y} = \frac{1}{N_{\mathbf{s}}} C_{\mathbf{s}}^H \mathbf{y}.$$

Its residual matrix R is the Toeplitz matrix generated from the correlation function $\rho_{\mathbf{ss}}(k)$ of \mathbf{s} :

$$\begin{aligned} R &= \frac{1}{N_{\mathbf{s}}} C_{\mathbf{s}}^H C_{\mathbf{s}} - I \\ &= \begin{bmatrix} 0 & \rho_{\mathbf{ss}}(-1) & \rho_{\mathbf{ss}}(-2) & \dots & \rho_{\mathbf{ss}}(-N_{\mathbf{h}} + 1) \\ \rho_{\mathbf{ss}}(1) & 0 & \rho_{\mathbf{ss}}(-1) & \ddots & \vdots \\ \rho_{\mathbf{ss}}(2) & \rho_{\mathbf{ss}}(1) & 0 & \ddots & \vdots \\ \ddots & \ddots & \ddots & \ddots & \vdots \\ \rho_{\mathbf{ss}}(N_{\mathbf{h}} - 1) & \ddots & \ddots & \dots & 0 \end{bmatrix}. \end{aligned}$$

Thus, the bias is governed by the sidelobes of ρ_{ss} . There exists a considerable literature on the correlation properties of PN sequences (The 1980 review paper of Sarwate & Pursley cites 136 references [76] See Hellesteth & Kumar for a 1997 review [38]). The bulk of the theory treats circular or periodic convolution whereas we need estimates of the maximum sidelobes for linear or aperiodic convolution (actually need a bound on $\|R\|$). A typical approach is to adapt the periodic estimates [38, page 98]. Set ρ_{\max} to be the maximum of the correlation sidelobes:

$$\rho_{\max}(N_s) = \max\{|\rho_{ss}(k)| : 1 \leq k \leq N_s\}.$$

Then arguments based on either the merit figure [38, page 102] or the Welsh bound [38, page 103] give a lower bound of

$$\rho_{\max}(N_s) \geq \frac{1}{\sqrt{4N_s - 3}}$$

for large N_s . The upper bound is more difficult [54] and there holds [75]

$$\rho_{\max}(N_s) < \frac{2 \log(4N_s/\pi)}{\pi} \frac{\sqrt{1 + 1/N_s}}{\sqrt{N_s}} + \frac{1}{N_s}$$

for large N_s . Figures 5.4 and 5.5 illustrate a variant of these sidelobe levels and bounds. The PN “type” or characteristic polynomial is held constant while the sample sidelobe levels are computed for increasing sequence length N_s . If the channel had a single strong reflector and the PN sequence from Figure 5.4 was used, then the bias induced by the strong reflector may be estimated as

$$\rho_{\max}(N_s) \text{ [dB]} \approx 9.7 - 0.86 \times N_s \text{ [dB]},$$

where N_s is in dB. With $N_s=511$, this reflector could induce a bias of approximately -13.5 dB and sets a “bias floor” on the channel estimate. These figures show that $\rho_{\max}(N_s)$ rolls off more slowly than $\mathcal{O}[1/\sqrt{N_s}]$. This slow reduction of $\rho_{\max}(N_s)$ for \mathbf{h}_{PN} requires long PN sequences. But long sequences may run afoul of the time-invariance assumption for the channel.

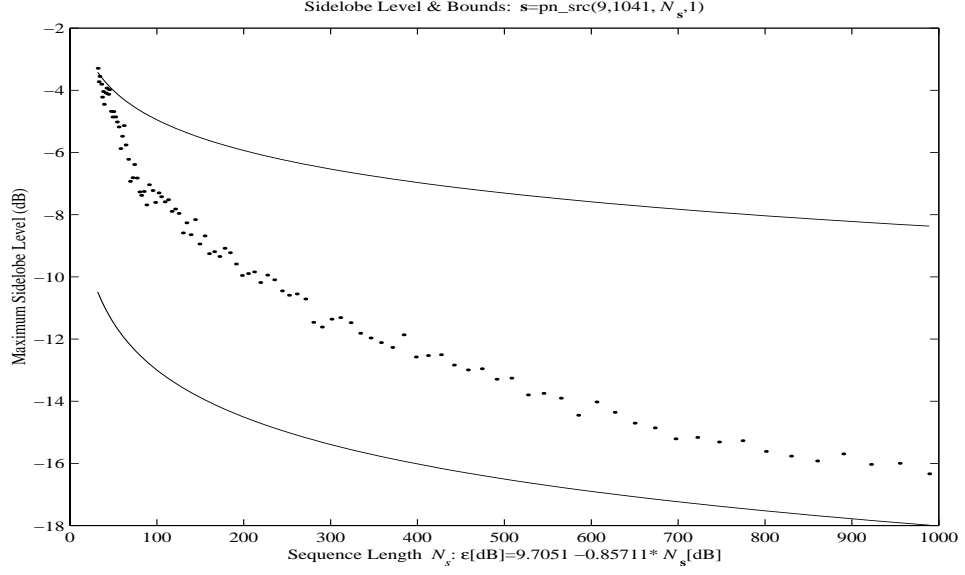


Figure 5.4: The dots mark the maximal sidelobe levels of the PN sequence $pn_src(9,1041,N_s,1)$. Upper bound: Sarwate. Lower bound: Welsh.

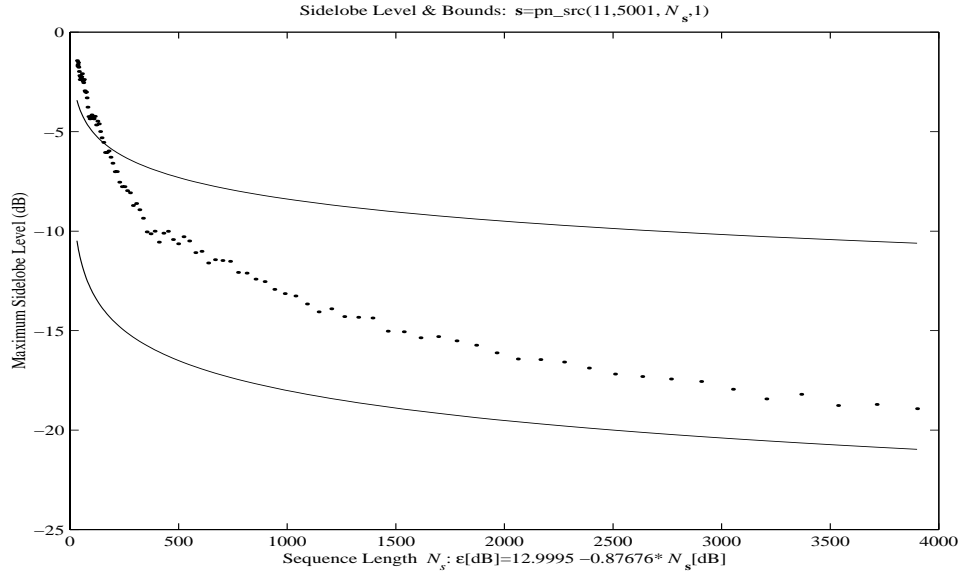


Figure 5.5: The dots mark the maximal sidelobe levels of the PN sequence $pn_src(11,5001,N_s,1)$. Upper bound: Sarwate. Lower bound: Welsh.

Although the maximum sidelobe level is useful, more accurate assessments of the bias are obtained from $\|R\|$. This is the next result and illustrated in the following figures.

Lemma 5.1.2 *Assume \mathbf{s} and \mathbf{h} are fixed vectors of length $N_{\mathbf{s}} \geq N_{\mathbf{h}}$. Assume \mathbf{s} is a PN sequence. Assume \mathbf{v} is a zero mean noise vector with covariance $R_{\mathbf{vv}}$. Solve the linear system*

$$\mathbf{y} = C_{\mathbf{s}}\mathbf{h} + \mathbf{v}$$

using the “matched filter”:

$$\mathbf{h}_{\text{PN}} = \frac{1}{N_{\mathbf{s}}} C_{\mathbf{s}}^H \mathbf{y}.$$

The residual matrix is

$$R = \frac{1}{N_{\mathbf{s}}} C_{\mathbf{s}}^H C_{\mathbf{s}} - I.$$

The bias is

$$\text{Bias}[\mathbf{h}_{\text{PN}}] = R\mathbf{h}$$

and has bounds:

(a) *If $\rho_{\max}(N_{\mathbf{s}})$ denotes the maximal sidelobe level then*

$$\|R\| \leq \rho_{\max}(N_{\mathbf{s}}) \times N_{\mathbf{h}} < \frac{4 \log(4N_{\mathbf{s}}/\pi)}{\pi \sqrt{N_{\mathbf{s}}}}.$$

(b) *If $\hat{\mathbf{s}} = \text{fft}(\mathbf{s}, N_{\mathbf{s}} + N_{\mathbf{h}} - 1)$ then*

$$\|R\| \leq \left\| \frac{1}{N_{\mathbf{s}}} |\hat{\mathbf{s}}|^2 - 1 \right\|_{\infty}.$$

The covariance is

$$\text{Cov}[\mathbf{h}_{\text{PN}}] = \frac{1}{N_{\mathbf{s}}^2} C_{\mathbf{s}}^H R_{\mathbf{vv}} C_{\mathbf{s}}.$$

If the noise is uncorrelated: $R_{\mathbf{vv}} = \sigma_{\mathbf{v}}^2 I$ then

$$\text{Var}[\mathbf{h}_{\text{PN}}] = \text{trace}[\text{Cov}[\mathbf{h}_{\text{PN}}]] = \sigma_{\mathbf{v}}^2 \frac{N_{\mathbf{h}}}{N_{\mathbf{s}}}.$$

The point of Lemma 5.1.2 is that the bias is bounded by $\|R\|$. Indeed, a channel simulation that took \mathbf{h} from the eigenspace of $\|R\|$ would attain maximal bias. *So how bad is this bias?* Figures 5.6 and 5.7 plot $\|R\|$ as a function of sequence length N_s while holding the channel length constant. These plots show $\|R\|$ is a decreasing function of the sequence length only to half the maximal sequence length. By comparing the dB levels with the maximum sidelobe level ρ_{\max} (Figures 5.4 and 5.5), we see that ρ_{\max} is an incomplete description of the bias. For completeness, the two bounds obtained from Lemma 5.1.2 are plotted. The FFT bound is very good — provided $N_s \approx N_h$. As N_s becomes much greater than N_h , the FFT bound levels off because R is the small compression of a large circulant matrix (See the discussion following Lemma 5.2.1). Using this large matrix to bound its compression R produces the loose upper bounds. The Frobenius bound follows $\|R\|$ well but is 10 dB too loose also.

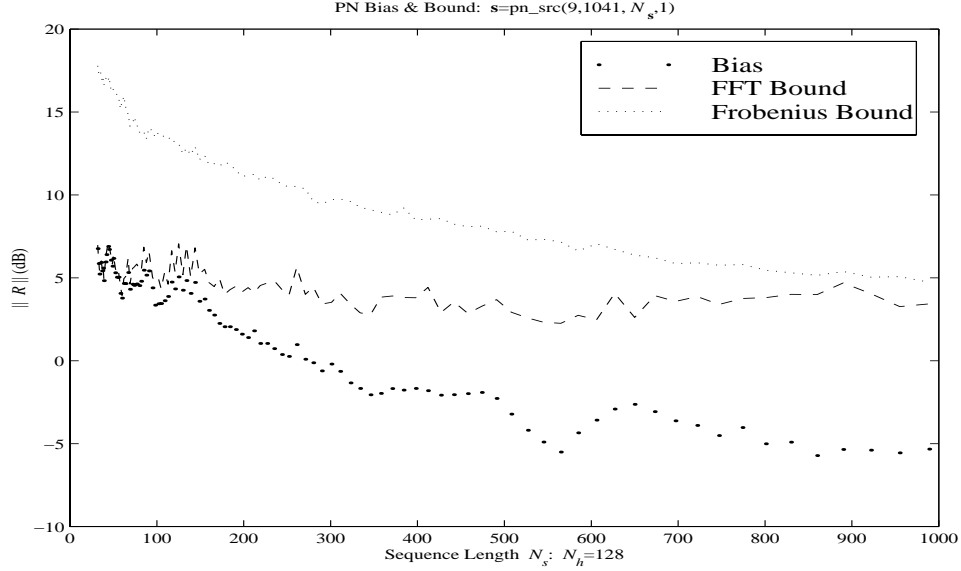


Figure 5.6: The dots mark the bias $\|R\|$ of the PN sequence `pn_src(9,1041, N_s ,1)`. The FFT bound is $\|\hat{\mathbf{s}}|^2/N_s - 1\|_\infty$. The Frobenius bound is $N_h \rho_{\max}(N_s)$.

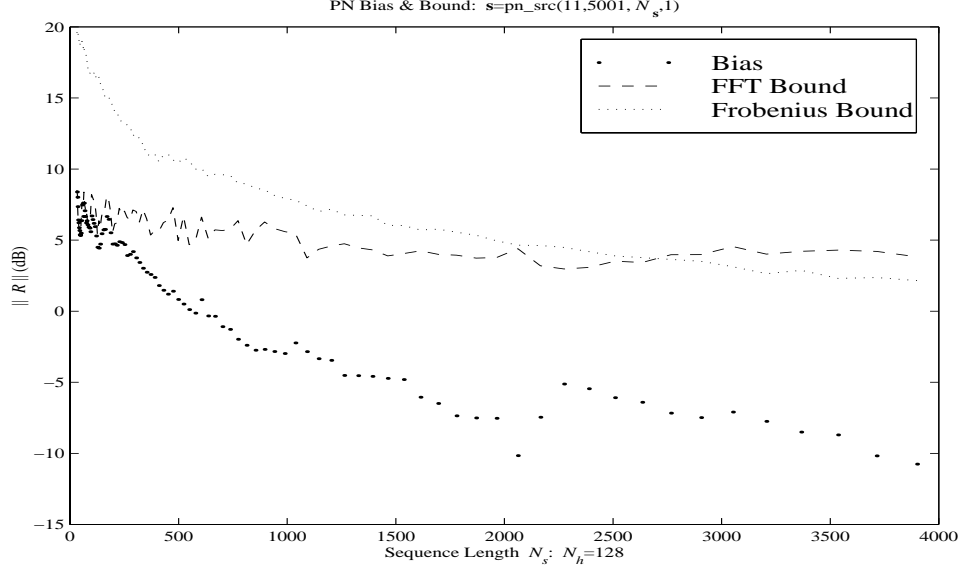


Figure 5.7: The dots mark the bias $\|R\|$ of the PN sequence `pn_src(11,5001, N_s ,1)`. The FFT bound is $\|\hat{\mathbf{s}}^2/N_s - 1\|_\infty$. The Frobenius bound is $N_h \rho_{\max}(N_s)$.

5.2 Gauss-Markov Processing

Recall that the time-invariant channel is modeled as

$$\mathbf{y} = \mathbf{s} * \mathbf{h} + \mathbf{v} = C_s \mathbf{h} + \mathbf{v},$$

where C_s denotes the convolution matrix determined by \mathbf{s} . The vectors \mathbf{s} and \mathbf{h} have lengths $N_s \geq N_h$. Processing all of \mathbf{y} gives C_s as the rectangular matrix

$$C_s = \text{conv2}(\text{eye}(N_h), \mathbf{s}) \sim (N_s + N_h - 1) \times N_h.$$

Some applications take only the center of \mathbf{y} for processing. This gives C_s as the square matrix

$$C_s = \text{conv2}(\text{eye}(N_h), \mathbf{s}, \text{'same'}) \sim N_h \times N_h.$$

The Gauss-Markov estimator assumes the following about the channel \mathbf{h} and the noise \mathbf{v} :

GM-0 \mathbf{h} is an unknown but non-random vector.

GM-1 $E[\mathbf{v}] = 0$.

GM-2 $E[\mathbf{v}\mathbf{v}^H] = R_{\mathbf{v}\mathbf{v}}$.

The Gauss-Markov estimate \mathbf{h}_{GM} is the linear minimum-variance unbiased estimate given as (See Theorem C.0.1):

$$\mathbf{h}_{\text{GM}} = (C_s^H R_{\mathbf{v}\mathbf{v}}^{-1} C_s)^{-1} C_s^H R_{\mathbf{v}\mathbf{v}}^{-1} \mathbf{y}$$

with covariance

$$\text{Cov}[\mathbf{h}_{\text{GM}}] = (C_s^H R_{\mathbf{v}\mathbf{v}}^{-1} C_s)^{-1}.$$

Thus, knowledge of the noise covariance is required for this filter. The exception occurs when the noise is uncorrelated which gives the pseudo-inverse. Because the Gauss-Markov estimate is unbiased, the bias that plagues the PN estimate is eliminated. Consequently, we expect the sidelobe leakage to be greatly reduced when compared to \mathbf{h}_{PN} . If the covariance of \mathbf{h}_{GM} is “less than” the mean-square error of \mathbf{h}_{PN} , then \mathbf{h}_{GM} is a better estimator than \mathbf{h}_{PN} . We explore these issues using the channel of Example 5.1.1.

Example 5.2.1 (The “Leaky” Channel (Continued)) Continuing with Example 5.1.1, recall the three reflectors in channel \mathbf{h} were selected for maximal sidelobe leakage (See Figures 5.1 and 5.2). Recall the symbol rate T was selected to match the sampling rate so that the receiver noise \mathbf{v} is IID: $R_{\mathbf{v}\mathbf{v}} = \sigma_v^2 I$. Then the Gauss-Markov estimate becomes the pseudo-inverse or the least-squares estimate:

$$\mathbf{h}_{\text{GM}} = C_s^+ \mathbf{y}$$

with covariance $\text{Cov}[\mathbf{h}_{\text{GM}}] = \sigma_v^2 (C_s^H C_s)^{-1}$. Figure 5.8 compares the magnitudes of the channel \mathbf{h} , the PN estimate \mathbf{h}_{PN} , and the Gauss-Markov estimate \mathbf{h}_{GM} . The entire vector \mathbf{y} is used so that C_s is rectangular. For this low-noise case, the Gauss-Markov estimate \mathbf{h}_{GM} outperforms the PN estimate \mathbf{h}_{PN} . \square

Several questions regarding the Gauss-Markov estimate naturally occur. The first question regards the well-known problems of such inverse filters. *Is C_s well-conditioned with respect to inversion?* That is, will small singular values of C_s amplify the noise to degrade the estimate \mathbf{h}_{GM} ? Figures 5.9

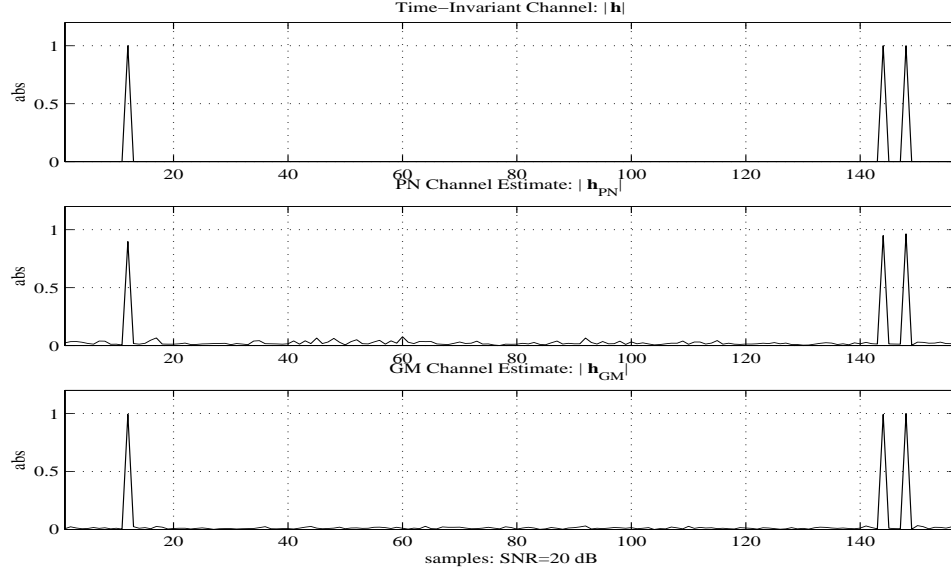


Figure 5.8: Upper Panel: The time-invariant channel magnitude $|\mathbf{h}|$. Middle Panel: The PN-estimate $|\mathbf{h}_{\text{PN}}|$. Lower Panel: The Gauss-Markov estimate $|\mathbf{h}_{\text{GM}}|$.

and 5.10 illustrate the condition number of C_s as a function of sequence length N_s while holding the channel length and PN type constant. Here the condition number of C_s is the ratio of the largest singular value to the smallest singular value. These figures show that C_s is well-conditioned for large N_s and a notion of the minimum sequence length needed to obtain a small condition number.

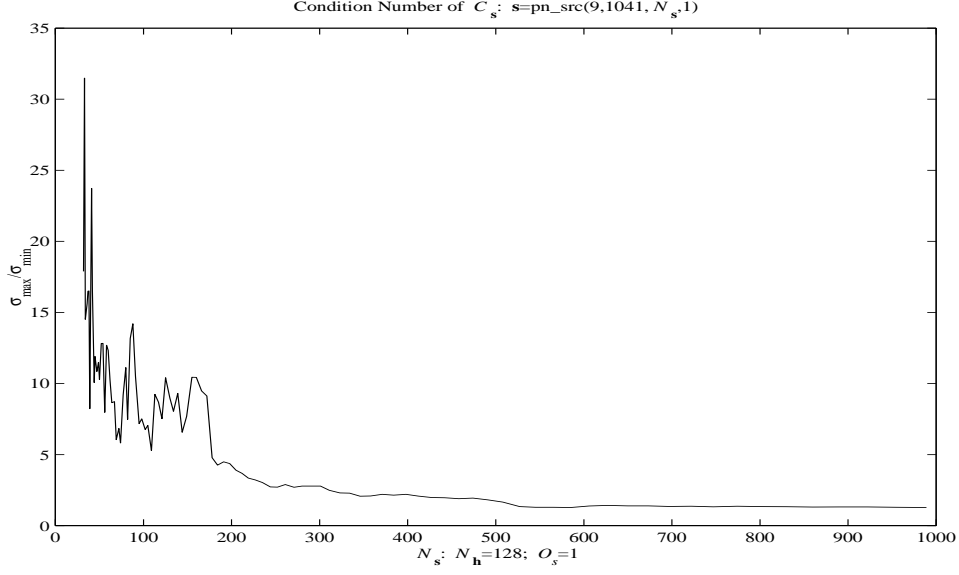


Figure 5.9: Condition number of C_s as a function of sequence length N_s . Sequence: $s=\text{pn_scr}(9,1041,N_s,1)$. Channel length: $N_h=128$.

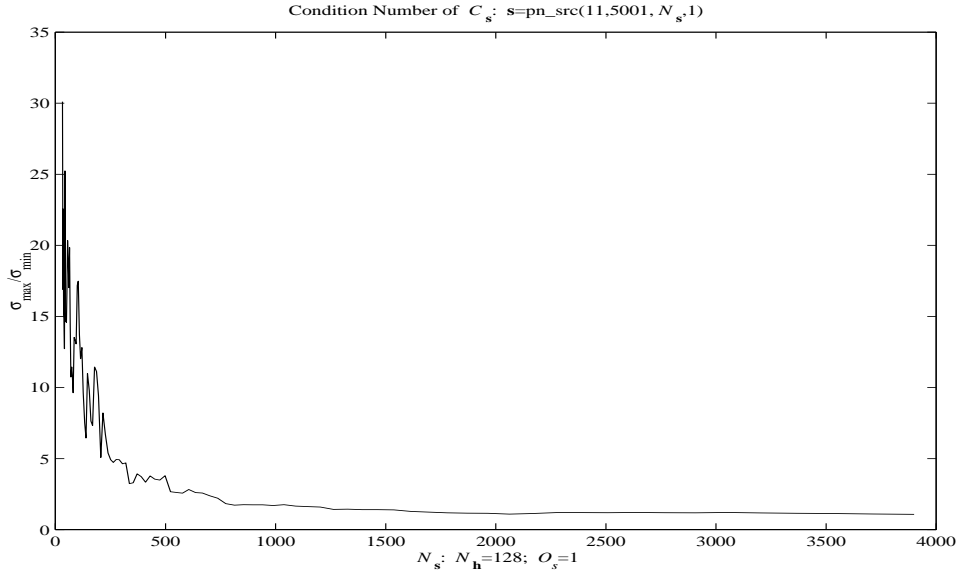


Figure 5.10: Condition number of C_s as a function of sequence length N_s . Sequence: $s=\text{pn_scr}(11,5001,N_s,1)$. Channel length: $N_h=128$.

The second question regards the variance: *How does the variance of the Gauss-Markov estimate \mathbf{h}_{GM} compare to the PN estimate \mathbf{h}_{PN} ?* Under the assumption that the noise is uncorrelated: $R_{\mathbf{v}\mathbf{v}} = \sigma_{\mathbf{v}}^2 I$ Lemma 5.1.2 gives that

$$\text{Var}[\mathbf{h}_{\text{PN}}] = \sigma_{\mathbf{v}}^2 \frac{N_{\mathbf{h}}}{N_{\mathbf{s}}},$$

while

$$\text{Var}[\mathbf{h}_{\text{GM}}] = \sigma_{\mathbf{v}}^2 \text{trace}[(C_{\mathbf{s}}^H C_{\mathbf{s}})^{-1}].$$

Figures 5.11 and 5.12 compare the variance of these two estimators assuming uncorrelated noise. The variance is normalized by $\sigma_{\mathbf{v}}^2$. These figures show the sequence length needed to reduce this (normalized) variance. Both plots also show by trading variance for bias, \mathbf{h}_{PN} obtains a slightly lower variance than \mathbf{h}_{GM} . For this report, variance is less of an issue than bias because the channel soundings will have a high SNR. A trade off between bias and variance is deferred until the third question.

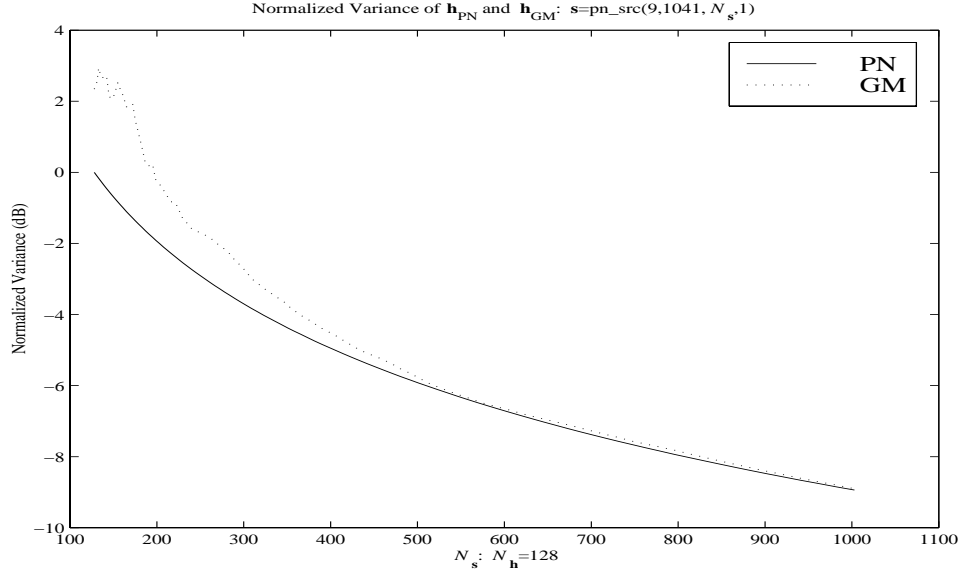


Figure 5.11: Normalized variance of \mathbf{h}_{PN} and \mathbf{h}_{GM} as a function of sequence length $N_{\mathbf{s}}$. Sequence: $\mathbf{s}=\text{pn_src}(9,1041, N_{\mathbf{s}},1)$. Channel length: $N_{\mathbf{h}}=128$.

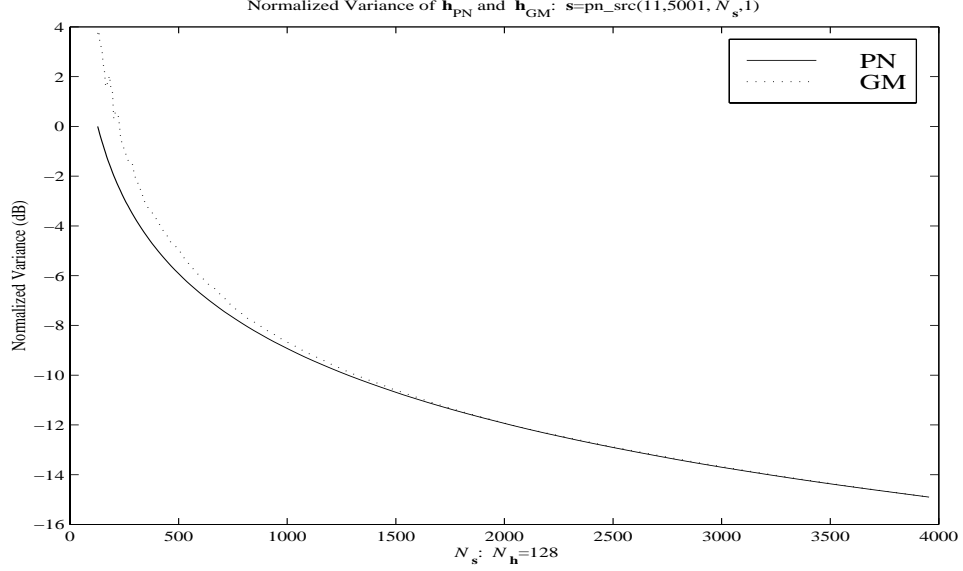


Figure 5.12: Normalized variance of \mathbf{h}_{PN} and \mathbf{h}_{GM} as a function of sequence length N_s . Sequence: $\mathbf{s}=\text{pn_src}(11,5001,N_s,1)$. Channel length: $N_h=128$.

The third question regards the practicality of the Gauss-Markov estimator. The size of C_s may make implementation difficult because

$$C_s \sim O_s(N_s + N_h - 1) \times O_s N_h.$$

For example, a 1001-point sequence transmitted through a channel of length 400 and oversampled by 12 makes $C_s \sim 16,800 \times 4800$. This is a rather large matrix to blindly invert. So is it worthwhile to ask: *What is a practical implementation or approximation to the Gauss-Markov estimator?* Given the low condition number of C_s , a left inverse is a candidate. One MATLAB implementation is:

$$\begin{aligned} M &= N_s + N_h - 1; \\ \mathbf{h}_{\text{FGM}} &= \text{ifft}(\text{fft}(\mathbf{y}) ./ \text{fft}(\mathbf{s}, M)); \\ \mathbf{h}_{\text{FGM}} &= \mathbf{h}_{\text{FGM}}(1 : N_h); \end{aligned}$$

The matrix formulation is also revealing. Let U denote the unitary $M \times M$ DFT matrix partitioned across its columns:

$$U = \frac{1}{\sqrt{M}} \text{dftmtx}(M) = [U_1 \ U_2] \sim M \times [N_{\mathbf{h}} \ N_{\mathbf{h}} - 1].$$

Let $\hat{\mathbf{s}} = \text{fft}(\mathbf{s}, M)$ and set $S = \text{diag}(\hat{\mathbf{s}})$. Then $C_{\mathbf{s}} = U^H S U_1$ and admits the left inverse

$$W = U_1^H S^{-1} U,$$

provided $\hat{\mathbf{s}}$ does not pointwise vanish. With this notation, the “specs” of this fast Gauss-Markov (FGM) estimate may be compared to the Gauss-Markov estimate.

Lemma 5.2.1 *Assume \mathbf{s} and \mathbf{h} are fixed vectors of length $N_{\mathbf{s}} \geq N_{\mathbf{h}}$, respectively. Assume \mathbf{s} is a PN sequence with DFT*

$$\hat{\mathbf{s}} = \text{fft}(\mathbf{s}, N_{\mathbf{s}} + N_{\mathbf{h}} - 1)$$

Assume also no component of $\hat{\mathbf{s}}$ vanishes. Assume \mathbf{v} is a zero mean noise vector with covariance $R_{\mathbf{vv}}$. Solve the linear system

$$\mathbf{y} = C_{\mathbf{s}} \mathbf{h} + \mathbf{v}$$

using with the “inverse filter”:

$$\mathbf{h}_{\text{FGM}} = W \mathbf{y} = U_1^H S^{-1} U \mathbf{y}.$$

Then \mathbf{h}_{FGM} is unbiased and has covariance

$$\text{Cov}[\mathbf{h}_{\text{FGM}}] = W R_{\mathbf{vv}} W^H$$

Example 5.2.2 (The “Leaky” Channel (Continued)) Continuing with Example 5.1.1, recall the three reflectors in channel \mathbf{h} were selected for maximal sidelobe leakage (See Figures 5.1 and 5.2). Recall the symbol rate T was selected to match the sampling rate so that the receiver noise \mathbf{v} is IID: $R_{\mathbf{vv}} = \sigma_{\mathbf{v}}^2 I$. Figure 5.13 compares the magnitudes of the channel \mathbf{h} , the Gauss-Markov estimate \mathbf{h}_{GM} , and the fast Gauss-Markov estimate \mathbf{h}_{FGM} . For this low-noise case, both estimators are comparable and outperform \mathbf{h}_{PN} . As expected, the noise floor has increased in \mathbf{h}_{FGM} . This effect is explored next. \square

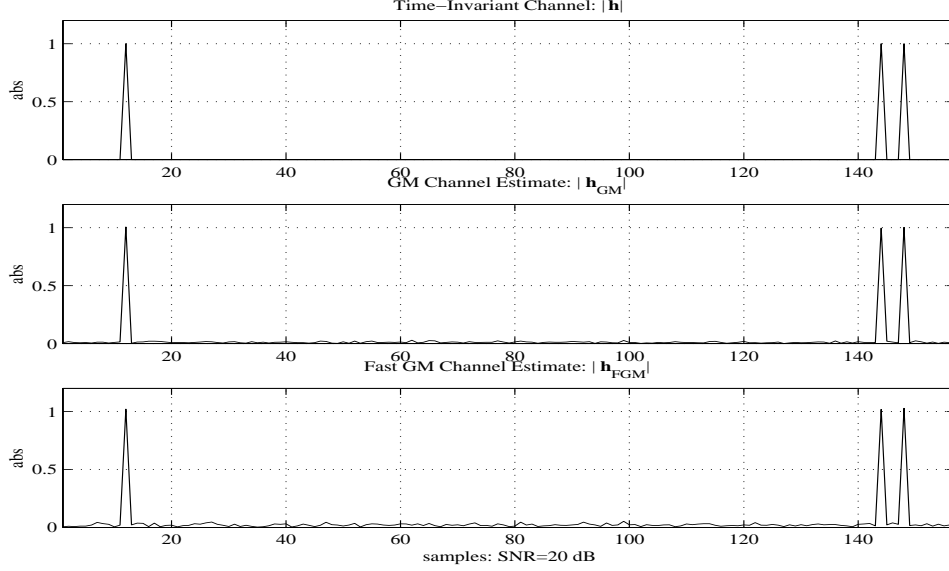


Figure 5.13: Upper Panel: The time-invariant channel magnitude $|\mathbf{h}|$. Middle Panel: The GM-estimate $|\mathbf{h}_{\text{GM}}|$. Lower Panel: The Fast Gauss-Markov estimate $|\mathbf{h}_{\text{FGM}}|$.

Because the Gauss-Markov estimate is the unbiased linear estimator with minimum variance (See Theorem C.0.1), it is natural to ask *How does the increase in variance of incurred by using \mathbf{h}_{FGM} rather than \mathbf{h}_{GM} ?* Gathering the covariances obtained so far, we have:

(a) $\text{Cov}[\mathbf{h}_{\text{PN}}] = N_s^{-2} C_s^H R_{\mathbf{v}\mathbf{v}} C_s.$

(b) $\text{Cov}[\mathbf{h}_{\text{GM}}] = (C_s^H R_{\mathbf{v}\mathbf{v}}^{-1} C_s)^{-1}.$

(c) $\text{Cov}[\mathbf{h}_{\text{FGM}}] = W R_{\mathbf{v}\mathbf{v}} W^H.$

If the noise is uncorrelated: $R_{\mathbf{v}\mathbf{v}} = \sigma_v^2 I$ then:

(a) $\text{Var}[\mathbf{h}_{\text{PN}}] = \sigma_v^2 N_{\mathbf{h}} N_s^{-1}.$

(b) $\text{Var}[\mathbf{h}_{\text{GM}}] = \sigma_v^2 \text{trace}[(U_1^H |S|^2 U_1)^{-1}].$

(c) $\text{Var}[\mathbf{h}_{\text{FGM}}] = \sigma_v^2 \text{trace}[U_1^H |S|^{-2} U_1].$

Ignoring subspace angles, $\text{Var}[\mathbf{h}_{\text{GM}}]$ sums $|\hat{\mathbf{s}}|^2$ before inverting so small Fourier coefficients need not be fatal. $\text{Var}[\mathbf{h}_{\text{FGM}}]$ inverts $|\hat{\mathbf{s}}|^2$ before summing so a small Fourier coefficient can blowup the variance. Figures 5.14 and 5.15 compare these normalized ($\sigma_v^2=1$) variances as a function of sequence length N_s . As expected, the variance of \mathbf{h}_{FGM} always exceeds the variance of \mathbf{h}_{GM} . And Fourier coefficients do vanish for a few sequence lengths (omitted from the plots). Regularization of \mathbf{h}_{FGM} can reduce this variance. Indeed, a heavily regularized estimate can have an arbitrarily small variance — with the usual cost of a large bias. So a bias-variance trade-off must be made. For example, the channel soundings collected for this report typically have an SNR of 20–30 dB. Figures 5.14 and 5.15 show \mathbf{h}_{FGM} has an additive noise gain rarely exceeding 10 dB. So a large SNR gives the nod to minimal regularization. Regularization schemes are discussed in the next section in the context of the Minimum-Variance estimator.

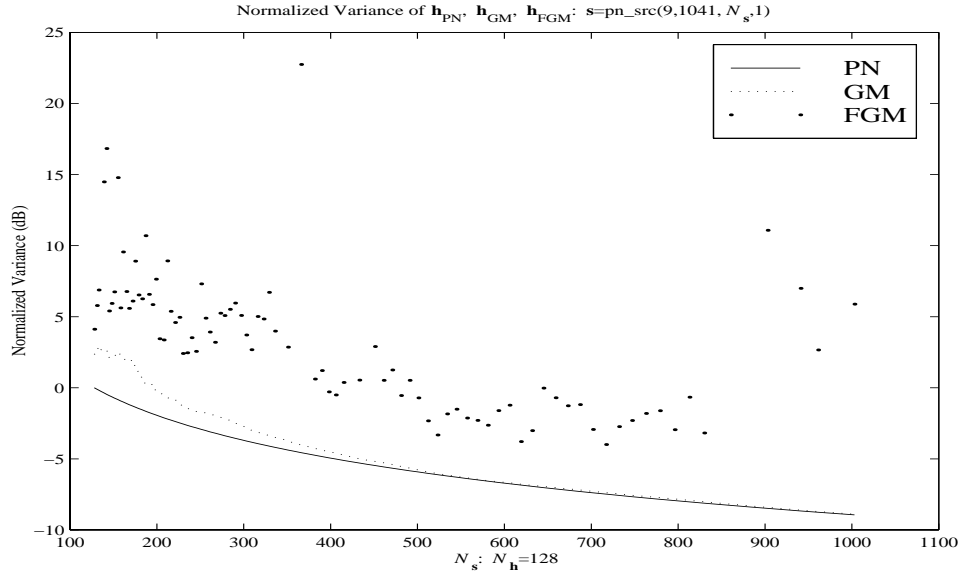


Figure 5.14: Normalized variance of \mathbf{h}_{PN} , \mathbf{h}_{GM} , and \mathbf{h}_{FGM} as a function of N_s . Sequence: $\mathbf{s}=\text{pn_src}(11,1041, N_s,1)$. Channel length: $N_{\mathbf{h}}=128$.

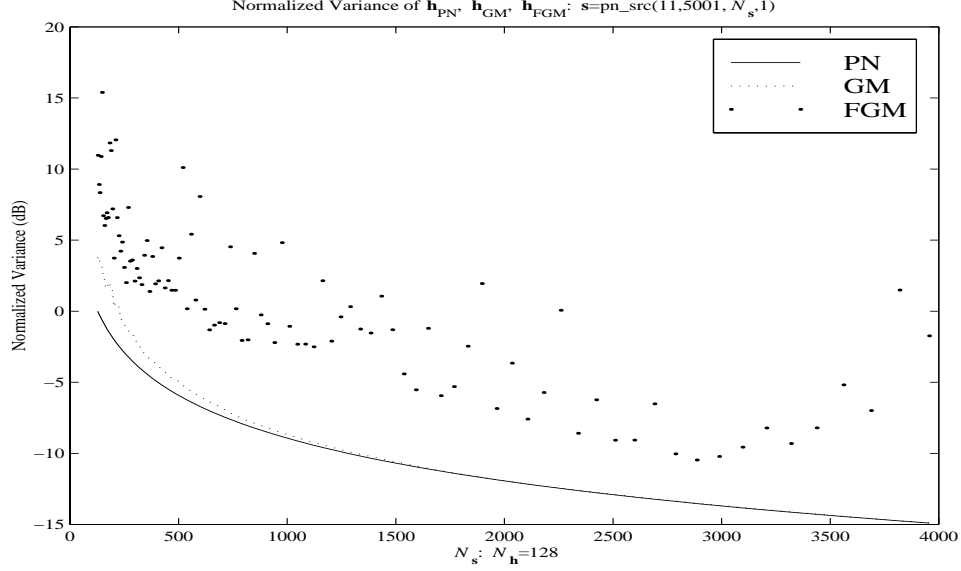


Figure 5.15: Normalized variance of \mathbf{h}_{PN} , \mathbf{h}_{GM} , and \mathbf{h}_{FGM} as a function of N_s . Sequence: $\mathbf{s}=\text{pn_src}(11,5001, N_s,1)$. Channel length: $N_{\mathbf{h}}=128$.

5.3 Minimum-Variance Processing

The minimum-variance estimator concludes this review of the sequence-based channel estimators. Recall that the time-invariant channel is modeled as

$$\mathbf{y} = \mathbf{s} * \mathbf{h} + \mathbf{v} = C_{\mathbf{s}} \mathbf{h} + \mathbf{v},$$

where $C_{\mathbf{s}}$ denotes the convolution matrix determined by \mathbf{s} . The vectors \mathbf{s} and \mathbf{h} have lengths $N_s \geq N_{\mathbf{h}}$. The Gauss-Markov estimate \mathbf{h}_{GM} is the linear unbiased estimate that minimizes

$$\mathbf{h}_{\text{GM}} = \text{argmin}\{E[\|\mathbf{h}_W - \mathbf{h}\|^2] : E[\mathbf{h}_W] = E[\mathbf{h}]\}.$$

The minimum variance estimate \mathbf{h}_{MV} is the linear estimate that minimizes

$$\mathbf{h}_{\text{MV}} = \text{argmin}\{E[\|\mathbf{h}_W - \mathbf{h}\|^2]\}.$$

Thus, a trade-off between bias and variance has been made to decrease the mean-square error. More formally, The minimum-variance estimator assumes the following about the channel \mathbf{h} and the noise \mathbf{v} (See Theorem C.0.2):

MV-0 \mathbf{h} is an unknown but random vector.

MV-1 $E[\mathbf{v}] = 0$.

MV-2 $E[\mathbf{v}\mathbf{v}^H] = R_{\mathbf{v}\mathbf{v}}$.

MV-4 $E[\mathbf{h}\mathbf{h}^H] = R_{\mathbf{h}\mathbf{h}}$.

MV-5 $E[\mathbf{h}\mathbf{v}^H] = 0$.

The mean of \mathbf{h} need not be zero (See [50, page 88] for this case). The minimum-variance estimate is

$$\mathbf{h}_{\text{MV}} = (C_s^H R_{\mathbf{v}\mathbf{v}}^{-1} C_s + R_{\mathbf{h}\mathbf{h}}^{-1})^{-1} C_s^H R_{\mathbf{v}\mathbf{v}}^{-1} \mathbf{y}$$

with covariance

$$\text{Cov}[\mathbf{h}_{\text{MV}}] = (C_s^H R_{\mathbf{v}\mathbf{v}}^{-1} C_s + R_{\mathbf{h}\mathbf{h}}^{-1})^{-1}$$

and bias $\text{Bias}[\mathbf{h}_{\text{MV}}] = RE[\mathbf{h}]$ with residual matrix (See Lemma 5.1.1)

$$R = (C_s^H R_{\mathbf{v}\mathbf{v}}^{-1} C_s + R_{\mathbf{h}\mathbf{h}}^{-1})^{-1} C_s^H R_{\mathbf{v}\mathbf{v}}^{-1} C_s - I.$$

Thus, knowledge of both the channel and noise covariances are required for this filter. So the same issues as for the Gauss-Markov filter arise here with greater complexity. To start the discussion, make the simplest assumptions: uncorrelated noise and uncorrelated channel with constant variance. Then the minimum-variance estimate has the form of the regularized pseudo-inverse of C_s :

$$\mathbf{h}_{\text{MV}}(\lambda) = (C_s^H C_s + \gamma I)^{-1} C_s^H \mathbf{y},$$

where the *regularization parameter* $\gamma = \sigma_{\mathbf{v}}^2 / \sigma_{\mathbf{h}}^2$ — in theory. In practice, γ must be determined from data. There is a vast literature on regularization. One of the heavy-weights is Per Christian Hansen and his *L-curve theory* [32], [33], [34], [94]. Hansen has found for inverting *ill-conditioned operators*, the logarithm of the curve

$$\gamma \rightarrow \left[\begin{array}{c} \|\mathbf{h}_{\text{MV}}(\gamma)\|_2 \\ \|\mathbf{y} - C_s \mathbf{h}_{\text{MV}}(\gamma)\|_2 \end{array} \right]$$

forms an “L” with optimal γ ’s located near the knee of the “L”. Although C_s is typically well-conditioned, we adapt these ideas for a bias-variance trade-off.

Figures 5.16 and 5.17 illustrate these kinds of trade-offs for the minimum-variance estimate $\mathbf{h}_{MV}(\gamma)$. Make the assumptions that the channel covariance $R_{\mathbf{h}\mathbf{h}} = \sigma_{\mathbf{h}}^2 I$ and noise covariance is $R_{\mathbf{v}\mathbf{v}} = \sigma_{\mathbf{v}}^2 I$. As $\gamma \rightarrow \infty$, the bias $R(\gamma)$ converges to I while $\text{Var}[\mathbf{h}_{MV}(\gamma)]$ converges to 0. Because C_s is well-conditioned, as $\gamma \rightarrow 0$, the bias $R(\gamma)$ converges to 0 while $\text{Var}[\mathbf{h}_{MV}(\gamma)]$ does not blowup but converges to a finite value. Thus, the vertical part of the “L” is missing. These performance curves show the trade-offs as a function of γ . The high SNR selects $\gamma \approx 0$, so the minimum-variance estimator converges to the Gauss-Markov estimator: $\mathbf{h}_{MV}(0) = \mathbf{h}_{GM}$.

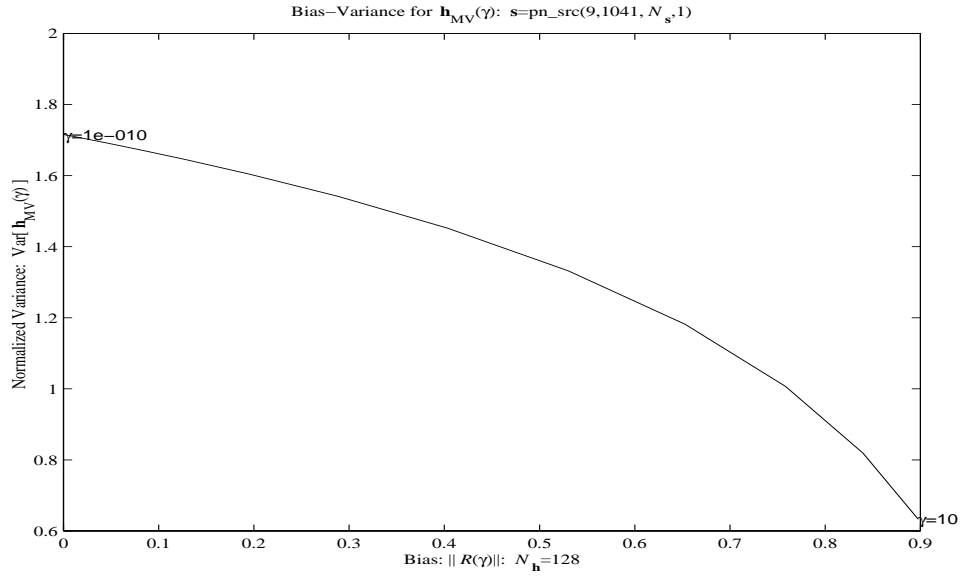


Figure 5.16: Bias $\|R(\gamma)\|$ of the minimum variance estimate versus the normalized variance of $\mathbf{h}_{MV}(\gamma)$. Sequence: $\mathbf{s}=\text{pn_src}(11,1041,N_s,1)$. Channel length: $N_{\mathbf{h}}=128$.

The high SNR also permits a simple regularization of the fast Gauss-Markov estimate of Section 5.2. Figures 5.14 and 5.15 show that \mathbf{h}_{FGM} is ill-conditioned for a few sequence lengths. One regularization scheme, using the notation of Lemma 5.2.1, is

$$\mathbf{h}_{RFGM}(\gamma) = U_1^H \text{diag} \left(\frac{\bar{\hat{\mathbf{s}}}}{|\hat{\mathbf{s}}|^2 + \gamma} \right) U \mathbf{y},$$

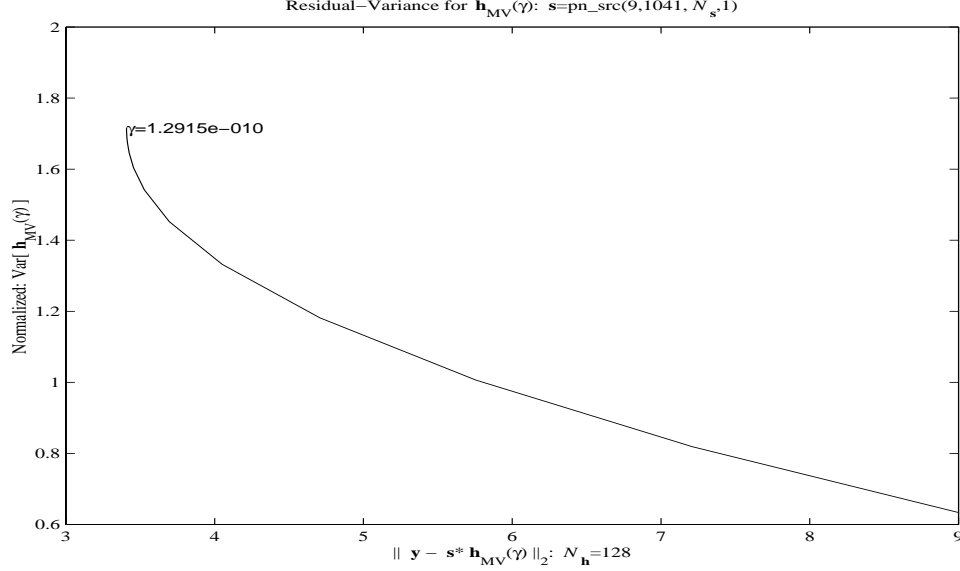


Figure 5.17: Residual versus normalized variance of $\mathbf{h}_{MV}(\gamma)$. Sequence: $\mathbf{s}=\text{pn_src}(11,1041,N_s,1)$. Channel length: $N_h=128$.

where γ is selected to pull the variance of $\mathbf{h}_{RFGM}(\gamma)$ within a specified tolerance of the variance of \mathbf{h}_{PN} . More formally, find the smallest γ so that

$$\text{Var}[\mathbf{h}_{RFGM}(\gamma)] \leq \text{Var}[\mathbf{h}_{PN}] + \Delta \quad [\text{dB}].$$

Figure 5.18 illustrates this approach with a tolerance of $\Delta=8$ dB. Almost all the FGM estimators have a variance within $\Delta=8$ dB of the PN estimator. These are marked with a “+” in the lower panel and have zero bias. Those \mathbf{h}_{FGM} estimates with a variance exceeding 8 dB are regularized to meet this variance tolerance. Their bias is marked with a “.” in the lower panel. The high SNR permits this fast estimate to be used with its bias-variance performance benchmarked against the PN estimate.

5.4 Review of the Sequence Literature

We use the previous estimators and examples to review the sequence literature. The linear system is

$$\mathbf{y} = \mathbf{s} * \mathbf{h} + \mathbf{v} = C_s \mathbf{h} + \mathbf{v}$$

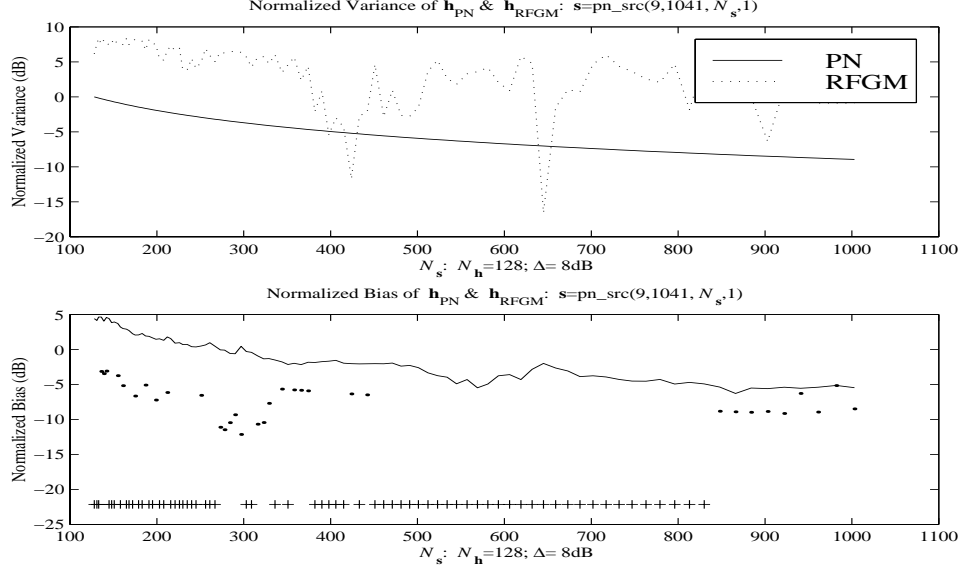


Figure 5.18: Upper Panel: Normalized variance of \mathbf{h}_{PN} , and $\mathbf{h}_{\text{RFGM}}(\gamma)$ as a function of N_s . Sequence: $\mathbf{s}=\text{pn_src}(11,5001,N_s,1)$. Channel length: $N_h=128$.

when C_s is typically invertible (hence a square matrix) and the noise \mathbf{v} is IID: $R_{\mathbf{v}\mathbf{v}} = \sigma_g^2 I$. The Gauss-Markov estimate becomes the inverse filter

$$\mathbf{h}_{\text{GM}} = C_s^{-1} \mathbf{y}$$

with error variance

$$E[\|\mathbf{h}_{\text{GM}} - \mathbf{h}\|_2^2] = \sigma_v^2 \text{trace}[(C_s^H C_s)^{-1}]. \quad (5.2)$$

The trick is to find a sequence \mathbf{s} so that the small singular values of C_s do not amplify the noise.

Avoiding this “blow-up” due to the small singular values is the starting point for the channel estimation of Milewski [52]. He assumes the linear system is modeled by *cyclic convolution* rather than linear convolution. Consequently, C_s is circulant and may be diagonalized by the DFT matrix: $F = \text{dftmtx}(N_s)$. With $\hat{\mathbf{s}} = F\mathbf{s} = \text{fft}(\mathbf{s})$, the variance is

$$E[\|\mathbf{h}_{\text{GM}} - \mathbf{h}\|_2^2] = \sigma_v^2 \sum_{k=1}^{N_s} |\hat{\mathbf{s}}(k)|^{-2}$$

Milewski minimizes the variance under the condition that $\|\mathbf{s}\|_2 = N_s$. The minimum occurs when all the Fourier coefficients are equal: $|\hat{\mathbf{s}}(k)|^2 = N_s$. Such sequences are called Constant Amplitude Zero Autocorrelation (CAZAC) sequences [15], [67]. The error variance for a CAZAC sequence is

$$E[\|\mathbf{h}_{\text{GM}} - \mathbf{h}\|_2^2] = \sigma_v^2.$$

Milewski remarks that a MLSR sequence has Fourier coefficients $\hat{\mathbf{s}}(0) = 1$ and $\hat{\mathbf{s}}(1) = \hat{\mathbf{s}}(3) = \dots \hat{\mathbf{s}}(N_s - 1)$ so that its variance is

$$E[\|\mathbf{h}_{\text{GM}} - \mathbf{h}\|_2^2] = \sigma_v^2 \frac{2N_s}{N_s + 1}.$$

That is, for large N_s , “a maximal-length sequence is at a 3-dB disadvantage compared to a sequence with zero autocorrelation” [52].

Milewski also states that the most important class of CAZAC sequences are the *polyphase sequences* that take their values from the roots of unity. Chu [15] found that “chirps” of the form:

$$\mathbf{s}(k) = \begin{cases} \exp(+j2\pi Pk^2/N_s) & N_s \text{ even} \\ \exp(+j2\pi Pk(k+1)/N_s) & N_s \text{ odd} \end{cases}$$

for the integer P relatively prime to N_s , qualified as such polyphase sequences.

Generalizations of the CAZAC sequences include the *semiperfect binary* sequences characterized by its cyclic autocorrelation function equal to zero at $\pm N_s/4$ bits around the origin [69]. That is, a trade-off between using binary values and having a “good” autocorrelation function has been made. Although Theorem C.0.1 quantifies the trade-off, references analyzing the covariance have not been found to date.

Direct use of Theorem C.0.1 is found in Felhauer’s work starting in 1993 [23], [21], [23]. Felhauer uses inverse filtering with a CAZAC sequence. He notes that $|\hat{\mathbf{s}}|$ is constant. Thus, the engineer is *free to set the phases to meet additional constraints*. Felhauer elects to find sequences that will be robust with respect to the amplifier’s non-linearities. He desires that the analog signal $s(t)$ input to the transmitter’s amplifier have “an envelope as constant as possible” [23]. If $p_T(t)$ denotes the pulse-shaping filter in the transmitter and \mathbf{s} is the CAZAC sequence then

$$s(t) = \sum_{k=1}^{N_s} s(k)p_T(t - kT).$$

Felhauer optimizes over the phases to minimize the *crest factor*

$$\text{CR}(s) = \frac{\|s\|_\infty}{\|s\|_2}.$$

This approach is said to be effective for combating system non-linearities.

Stüber, Austin, and Katz [86] use the Gauss-Markov approach to minimize variance in Equation 5.2. They do *not* require C_s to be circulant. They do restrict their search to elements of the constellation points, and also require the *linear* autocorrelation function have small sidelobes. Their search extended to only 4 taps.

From the current literature, it would appear that the Gauss-Markov estimator has become an established technique for channel estimation that outperforms the standard PN estimator. However, much of the analysis is at baseband. Baseband assumptions, such as those in Chapter 2, assume proper demodulation. Chapter 8 demonstrates that a demodulator must part of a practical channel estimator. This is the approach to channel estimation in Chapter 6: the channel the associated covariances, and the demodulator are adaptively estimated using a minimum-variance estimator.

Chapter 6

Channel Estimation: System Identification

The channel estimation problem introduced in the previous chapter admits an interpretation as a classical system identification problem [37]. Figure 6.1 shows the setup and its solution by system identification. A *known* input signal is applied to an *unknown* system. The *observed* signal is the output of the system corrupted by additive noise. The unknown system is linear but may be time-varying. The known input signal is also applied to an adaptive linear filter. An *error* signal is obtained by subtracting the observed signal from the output of the adaptive filter. By forcing the adaptive filter to approximate the observed signal, the adaptive filter itself is then interpreted as an estimate of the unknown system. To force this fit, the weights of the adaptive filter are selected to minimize the norm of the error signal. A typical norm is the mean square error (MSE) or power of the error signal.

This processing raises an interesting identification issue: *Why should the adaptive filter so obtained have anything to do with the unknown system?* We begin by specializing this general problem to channel estimation. Section 6.1 shows how to insert the Input Delay Spread function for the unknown system and the symbol sequence for the input signal. Section 6.2 gives a filter-bank approach to estimate the channel. Section 6.3 boosts this filter-bank approach by mitigating residual carrier effects. Section 6.4 combines both approaches. With this background in place, Section 6.5 answers the identification issue by demonstrating the uniqueness of the adaptive filter. Section 6.1 closes by setting the adaptive filter parameters.

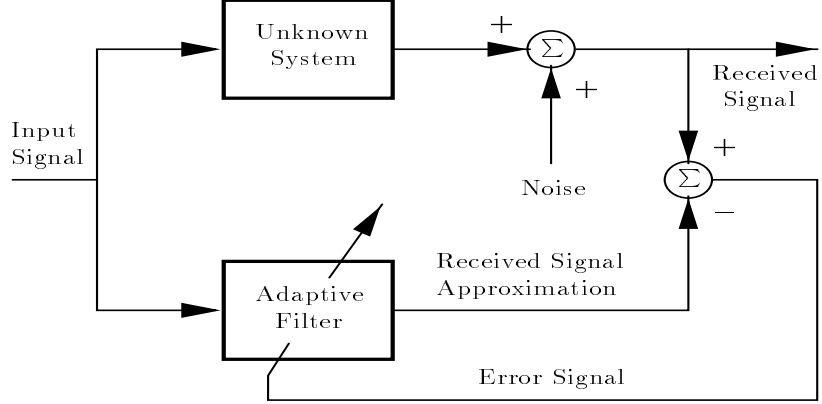


Figure 6.1: Generic system identification schematic.

6.1 The Discrete Channel

Specific to channel estimation, we estimate the *discrete baseband Input Delay Spread function* $h_B(m, k)$ of Equation 3.4 as the unknown system in Figure 6.1. The input signal is the zero-filled symbol sequence $\{\tilde{s}_m\}$ of Equation 3.5. Although $h_B(m, k)$ has infinite support in the lag variable k because of the raised cosine pulse $x_{RC}(k\tilde{T})$, the estimate is based upon a time-varying, causal finite impulse response (FIR) structure and is denoted by $\{\hat{h}_B(m, k)\}_{k=0}^{L-1}$.

The length L of the FIR filter must accommodate the largest expected delay spread with corresponding temporal smoothing caused by the filter $x_{RC}(k\tilde{T})$. In vector notation, the channel estimate at time m is given by

$$\hat{\mathbf{h}}_{B,L}(m)^H = [\hat{h}_B(m, 0) \ \hat{h}_B(m, 1) \ \cdots \ \hat{h}_B(m, L-1)] \quad (6.1)$$

and the symbol vector is given by

$$\tilde{\mathbf{s}}_m = [\tilde{s}_m \ \tilde{s}_{m-1} \ \cdots \ \tilde{s}_{m-L+1}]^T. \quad (6.2)$$

The output of the adaptive channel approximation filter is given by

$$\hat{y}_m = \hat{\mathbf{h}}_{B,L}^H(m) \tilde{\mathbf{s}}_m. \quad (6.3)$$

Figure 6.2 is the schematic of this discrete channel estimation problem. The discrete noise term $\{n_m\}$ corresponds to the sampled lowpass noise process in Equation 3.3.

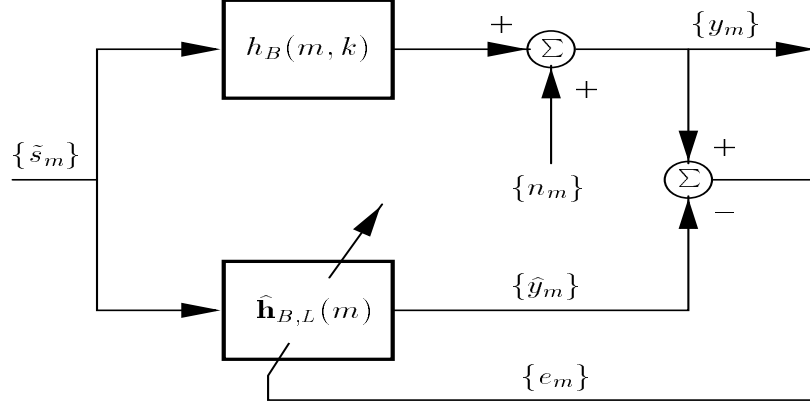


Figure 6.2: Discrete baseband channel estimation schematic.

6.2 A Filterbank Approach

The channel estimation technique depicted in Figure 6.2 can be implemented several ways. We propose a computationally efficient algorithm to exploit the zero-filled input sequence $\{\tilde{s}_m\}$. In addition, we extend the processing to handle a special “noise” type. Residual RF carrier effects resulting from Doppler or frequency offset between the transmitter and receiver oscillators may exist in the received data $\{y_m\}$. To compensate for these residual carrier effects, an additional phase recovery loop is incorporated into the channel estimation algorithm.

The channel estimate vector $\hat{\mathbf{h}}_{B,L}(m)$ will be updated at the sampling rate $1/\tilde{T}$. Because the input sequence $\{\tilde{s}_m\}$ is zero-filled, Equation 6.3 indicates that only a subset of the filter coefficients corresponding to non-zero elements of $\{\tilde{s}_m\}$ contribute to the output $\{\hat{y}_m\}$ at each sample m . As a consequence, only those coefficients are updated. An individual coefficient is updated at the symbol rate $1/T$. For the sake of simplicity, we assume that the FIR filter length L is an integer multiple \hat{L} of the oversampling value O_s ($L = O_s \hat{L}$).

Then the single-filter estimation procedure of Figure 6.2 naturally decomposes into a bank of filters. This is depicted Figure 6.3, where $\hat{m} = \lfloor m/O_s \rfloor$ and $\lfloor x \rfloor$ denotes the integer less than or equal to x . The input sequence $\{s_{\hat{m}}\}$ to the filter bank is incremented once every O_s samples. So during one cycle through the filter bank, each filter operates on the same sequence of data symbols.

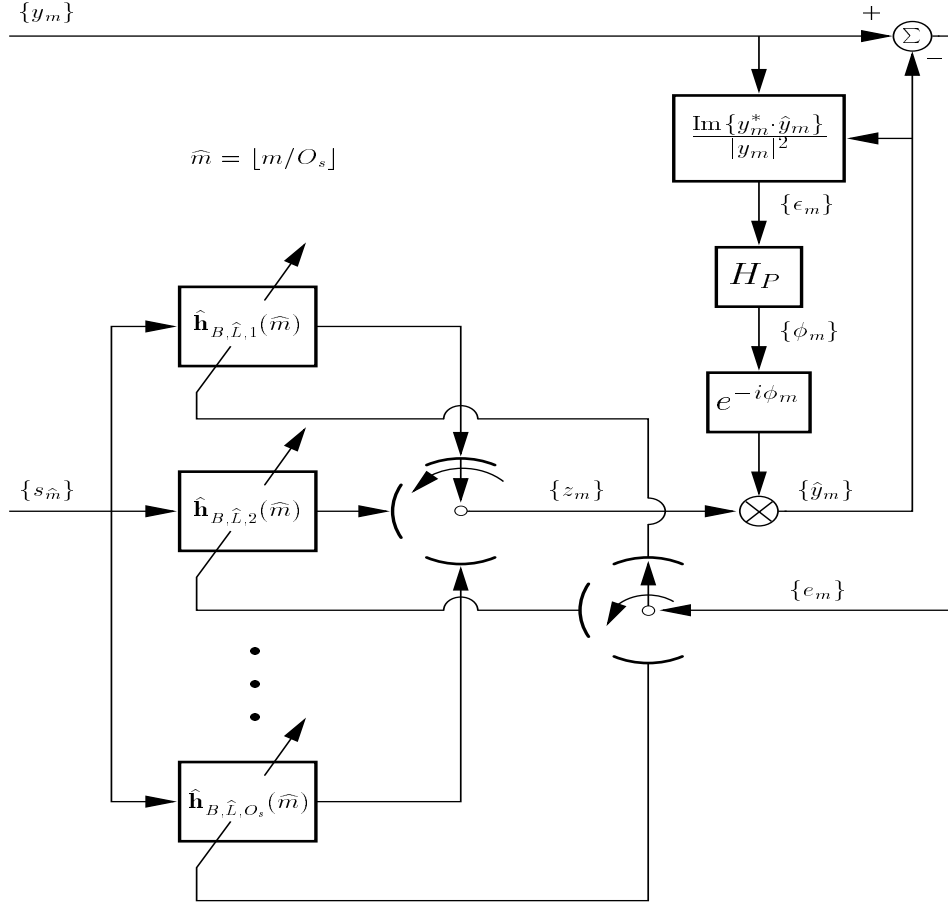


Figure 6.3: Channel estimation implementation with residual carrier compensation.

6.3 Residual Carrier Recovery

The residual carrier recovery circuit displayed in Figure 6.3 has been used in adaptive equalization-demodulation [19], [16]. The loop filter is shown in Figure 6.4 and has transfer function

$$H_P(z) = \frac{\gamma (1 - \rho z^{-1}) z^{-1}}{(1 - z^{-1})(1 - \mu z^{-1})}. \quad (6.4)$$

An exact analysis of the carrier recovery loop is difficult. Standard simplifying assumptions are [19]: (i) The channel estimation routine models the propagation channel *exactly*; (ii) Only a small error exists in the estimation

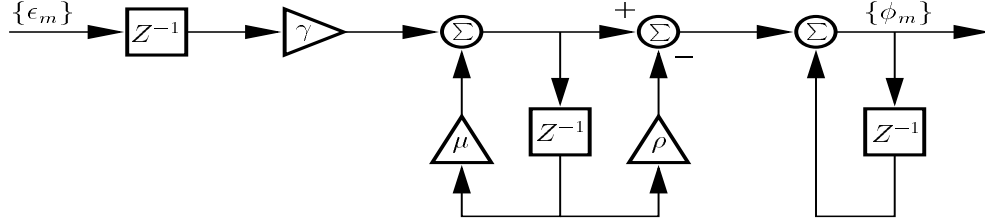


Figure 6.4: Residual carrier recovery loop filter $H_P(z)$.

of the residual carrier phase. These assumptions permit us to write

$$\hat{y}_m = e^{-i(\phi_m - \theta_m)} y_m, \quad (6.5)$$

where θ_m is the actual residual carrier phase. Because the difference in the phases is small, we have the linear approximation:

$$\epsilon_m = \sin(\phi_m - \theta_m) \approx \phi_m - \theta_m.$$

Figure 6.5 displays this linearized phase lock loop approximation. Its transfer function is

$$H_{\text{PLL}}(z) = \frac{\gamma(1 - \rho z^{-1})z^{-1}}{1 - (1 + \mu - \gamma)z^{-1} + (\mu - \gamma\rho)z^{-2}}. \quad (6.6)$$

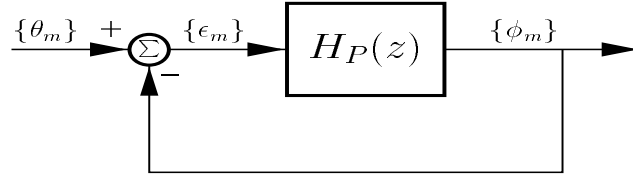


Figure 6.5: Linear model of the residual carrier recovery phase lock loop.

Assumptions (i) and (ii) permit us to approximate the carrier recovery loop as a second-order phase lock loop [80]. The filter parameters γ , μ and ρ are chosen so that the phase lock loop bandwidth is “wide” during signal acquisition and “narrow” during channel tracking. Actual values are determined through experiment.

6.4 Implementation: Filterbanks & Carrier Recovery

Figure 6.3 reveals that the Input Delay Spread function estimate is multiplexed into a bank of filters. To recover the estimate $\hat{\mathbf{h}}_{B,L}(\widehat{m})$, define the matrix

$$\widehat{\mathbf{H}}_B(\widehat{m}) = \begin{bmatrix} \hat{\mathbf{h}}_{B,\widehat{L},1}^T(\widehat{m}) \\ \hat{\mathbf{h}}_{B,\widehat{L},2}^T(\widehat{m}) \\ \vdots \\ \hat{\mathbf{h}}_{B,\widehat{L},O_s}^T(\widehat{m}) \end{bmatrix}. \quad (6.7)$$

Then $\hat{\mathbf{h}}_{B,L}(\widehat{m})$ is recovered by consecutively aligning the columns of $\widehat{\mathbf{H}}_B(\widehat{m})$ into a vector.

Several adaptive algorithms can be used to update the vectors $\hat{\mathbf{h}}_{B,\widehat{L},j}(\widehat{m})$. We utilize the minimum MSE criteria and approximate the solution with the robust and computationally efficient normalized least mean square (NLMS) algorithm [92], [37] in which each filter is updated as

$$\hat{\mathbf{h}}_{B,\widehat{L},j}(\widehat{m} + 1) = \hat{\mathbf{h}}_{B,\widehat{L},j}(\widehat{m}) + \tilde{\mu} e^{-i\phi_m} e_m^* \mathbf{s}_{\widehat{m}} / \|\mathbf{s}_{\widehat{m}}\|^2, \quad (6.8)$$

where

$$\begin{aligned} \mathbf{s}_{\widehat{m}} &= [s_{\widehat{m}} s_{\widehat{m}-1} \cdots s_{\widehat{m}-\widehat{L}+1}]^T \\ e_m &= y_m - \hat{\mathbf{h}}_{B,\widehat{L},j}^H(\widehat{m}) \mathbf{s}_{\widehat{m}} e^{-i\phi_m} \end{aligned} \quad (6.9)$$

and $j = \text{rem}(m, O_s) + 1$, $\tilde{\mu}$ is the step size parameter chosen such that $0 < \tilde{\mu} < 2$ [37], and $\|\mathbf{s}_{\widehat{m}}\|^2 = \widehat{L}$ for symbols with unit variance.

Remarks: (i) Implicit in this algorithm and Figure 6.2 is that the data have been appropriately synchronized such that $\{y_m\}$ and $\{\hat{y}_m\}$ correspond to approximately the same input data sequence. (ii) The input delay spread function estimate derived from Figure 6.2 using the zero-filled sequence $\{\tilde{s}_m\}$ is not identical to the estimate derived from Figure 6.3 using the sequence $\{s_{\widehat{m}}\}$. Each estimate $\hat{\mathbf{h}}_{B,L}(\widehat{m})$ derived from Figure 6.3 spans O_s estimates from Figure 6.2. Equivalently, only the updated coefficients are incorporated into the vector estimate of Figure 6.3. However, if the channel is varying

slowly enough (much slower than the symbol rate) the difference between the snapshots of the estimates at time m derived from Figure 6.2 and at time \widehat{m} from Figure 6.3 is insignificant.

6.5 Linking the Filter to the Channel

The algorithm described in Section 6.4 *approximates* the optimum MSE solution — the Wiener filter. The introduction raised the question regarding how the Wiener filter adequately represents the discrete baseband Input Delay Spread function. We conclude by explicitly making this link.

The output $\{y_m\}$ of the linear, time-varying system of Figure 6.2 is

$$y_m = \sum_{k=-\infty}^{\infty} h_B(m, k) \tilde{s}_{m-k} + n_m. \quad (6.10)$$

For simplicity, we assume that there is no residual RF carrier component. The output of the Wiener filter is given by

$$\hat{y}_{\text{OPT},m} = \hat{\mathbf{h}}_{\text{OPT},B,\hat{L},j}^H(\widehat{m}) \mathbf{s}_{\widehat{m}} \quad (6.11)$$

where

$$m = \widehat{m}O_s + j - 1 \quad (6.12)$$

and $\hat{\mathbf{h}}_{\text{OPT},B,\hat{L},j}(\widehat{m})$ is the Wiener filter of the j^{th} component of the filter bank. Defining the autocorrelation matrix

$$\mathbf{R}_s(\widehat{m}) = E \left[\mathbf{s}_{\widehat{m}} \mathbf{s}_{\widehat{m}}^H \right], \quad (6.13)$$

and the cross correlation vector

$$\mathbf{p}_j(\widehat{m}) = E [y_m^* \mathbf{s}_{\widehat{m}}], \quad (6.14)$$

the j^{th} Wiener filter is given by [37]

$$\hat{\mathbf{h}}_{\text{OPT},B,\hat{L},j}(\widehat{m}) = \mathbf{R}_s^{-1}(\widehat{m}) \mathbf{p}_j(\widehat{m}). \quad (6.15)$$

Assuming that the input data process $\{s_{\widehat{m}}\}$ is white with zero mean and variance σ_s^2 , the Wiener weights are given by

$$\hat{\mathbf{h}}_{\text{OPT},B,\hat{L},j}(\widehat{m}) = \frac{1}{\sigma_s^2} E [y_m^* \mathbf{s}_{\widehat{m}}]. \quad (6.16)$$

Next, assuming that the noise process $\{n_m\}$ is zero mean and independent of the input symbols $\{\hat{s}_m\}$, the cross correlation vector $\mathbf{p}_j(\widehat{m})$ is given by

$$\mathbf{p}_j(\widehat{m}) = E \left[\sum_{k=-\infty}^{\infty} h_B^*(\widehat{m}O_s + j - 1, k) \hat{s}_{\widehat{m}O_s + j - 1 - k}^* \mathbf{s}_{\widehat{m}} \right]. \quad (6.17)$$

Simplifying, we get the Wiener weights

$$\hat{\mathbf{h}}_{\text{OPT},B,\hat{L},j}(\widehat{m}) = \begin{bmatrix} h_B^*(\widehat{m}O_s + j - 1, j - 1) \\ h_B^*(\widehat{m}O_s + j - 1, j - 1 + O_s) \\ h_B^*(\widehat{m}O_s + j - 1, j - 1 + 2O_s) \\ \vdots \\ \vdots \\ \vdots \\ h_B^*(\widehat{m}O_s + j - 1, j - 1 + (\hat{L} - 1)O_s) \end{bmatrix}. \quad (6.18)$$

Then, using the de-multiplexing scheme suggested by Equation 6.7 and using Equation 6.1, the L coefficients representing the minimum MSE estimate are given by

$$\hat{h}_{\text{OPT},B}(\widehat{m}, k) = h_B(\widehat{m}O_s + \text{rem}(k, O_s), k), \quad 0 \leq k \leq L - 1. \quad (6.19)$$

This estimate is a *windowed* version of the discrete baseband Input Delay Spread function spanning O_s time samples. Also, if the step size parameter μ of the NLMS update algorithm of Equation 6.8 is “small enough”, standard analysis shows that this approximating solution approaches the Wiener filter in the mean and has bounded variance when operating in the steady-state [37].

6.6 Setting the Adaptive Filter Parameters

Table 6.1 lists values of the adaptive filter parameters which are used to process the simulated and experimental data. Figure 6.6 is the corresponding frequency response of the phase lock loop filter $H_{\text{PLL}}(z)$. The parameters are divided into three modes. During *acquisition mode*, the bandwidth of $H_{\text{PLL}}(z)$ is widest resulting in rapid initialization of the adaptive filter weights and coarse tuning to the carrier frequency and phase. The *training mode* has

a narrower bandwidth which allows through less noise and is set for convergence of the adaptive filter weights and fine tuning of the carrier frequency. The *tracking mode* has the narrowest bandwidth and accommodates tracking of time-varying propagation environments.

Table 6.1: AF processing parameters.

Mode	Parameter	Value
Acquisition	γ	0.080
	μ	0.800
	ρ	0.100
	$\tilde{\mu}$	0.500
Training	γ	0.040
	μ	0.800
	ρ	0.100
	$\tilde{\mu}$	0.250
Tracking	γ	0.020
	μ	0.800
	ρ	0.100
	$\tilde{\mu}$	0.125

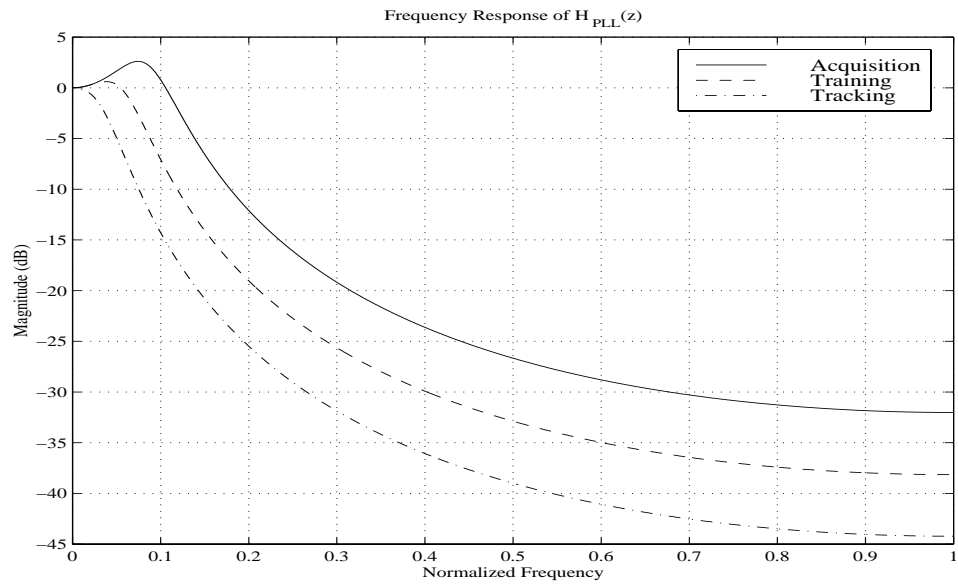


Figure 6.6: Frequency response of the phase lock loop for the three modes of operation.

Chapter 7

Naval Communication Channel Datasets

This chapter describes three sets of data files collected for estimating the characteristics of communication channels. The first set described in Section 7.1 contains emulated RF communication channels for verifying channel estimation algorithms. The other two sets are from live over-the-air mobile experiments. Section 7.2 describes a mobile HMMWV transmitting to a fixed shore site. Section 7.3 describes a mobile Navy ship transmitting to the same fixed shore site. These experiments provide sets of data files representative of urban Marine Corps and the Naval littoral communication environments, respectively.

7.1 Multipath Emulated Data Files

The Telecom Analysis Systems, Inc. TAS 4500 RF Channel Emulator was used to collect multipath emulated data files to verify the channel estimation algorithms. These emulated data files provide a means to validate the accuracy of the channel estimation procedures because the characteristics of each of the discrete multipaths (delay, fade rate, fading statistics, path loss) are known (to the accuracy of the TAS 4500).

The TAS 4500 converts a single RF signal (15 MHz bandwidth) from 25–2500 MHz to a 140 MHz IF frequency. This signal is split into one to six separate propagation paths with a user-defined delay, fade, and loss applied to

each path. These individual fading multipaths are combined and then mixed back to the original RF carrier frequency. The delays on each multipath can be varied from 1 nanosecond to 100 microseconds with 1 nanosecond resolution. The short-term fading can be Ricean (using the GSM model) or Rayleigh with fade rates varying from ± 1 to ± 740 Hz with 0.1 Hz resolution. The repetition interval for the short-term fading is longer than 20 minutes. In addition, a static phase shift can be placed on any multipath from 0 to 360 degrees in 0.1 degree increments. The loss on each multipath can be set to 0 to 40 dB with 0.1 dB resolution. Shadowing effects can be emulated using log-normal fading.

Figure 7.1 shows the equipment configuration used to collect the multipath emulated data files. A CCITT O.153 standard 511 pseudorandom bit pattern was generated with the Telecommunications Techniques Corporation FIREBERD 4000 at a data rate of 999,995 bps¹. This repeated pattern was modulated with BPSK (no coding, no scrambling, no differential encoding, +45 degree phase shift) by the CommQuest 2000 to a 70 MHz, -17 dBm IF signal. The IF signal was upconverted to an RF frequency of 231.5 MHz, 0 dBm with the MITEQ UP-70-313 upconverter and then amplified to 40 Watts with the Amplifier Research AR100W1000M1 Linear Power Amplifier. This power amplifier is Class A at this power amplification. The RF signal is post-selection filtered to reduce out-of-band emissions with the standard Navy UHF multi-coupler OA/9123. After 53 dB of attenuation, the RF signal was fed into the TAS 4500 RF Channel Emulator to create the desired multipath environment. The RF multipath fading signal from the TAS 4500 was attenuated by 35 dB to -70 dBm, pre-selection filtered by another OA/9123 UHF multicoupler, and then downconverted to 70 MHz IF using the MITEQ DN-313-70-AGC. This received IF signal was then used to collect multipath emulated data files using the Applied Signal Technologies AST195 Snapshot Analyzer.

The AST195 used a 12 Msps sample rate to collect 8-bit samples. The signal was bandpass sampled giving approximately 12 samples per bit interval. Narrowband filtering was performed at 70 MHz IF before sampling to reduce out-of-band energy. The resulting aliased IF frequency was 2.0 MHz with spectral inversion.

There are four file types: reference files; static three-path files; dynamic

¹The data rate was set to 1 Mbps but it was later found to be inaccurate by -5 bps.

EMULATED DATA TEST SETUP

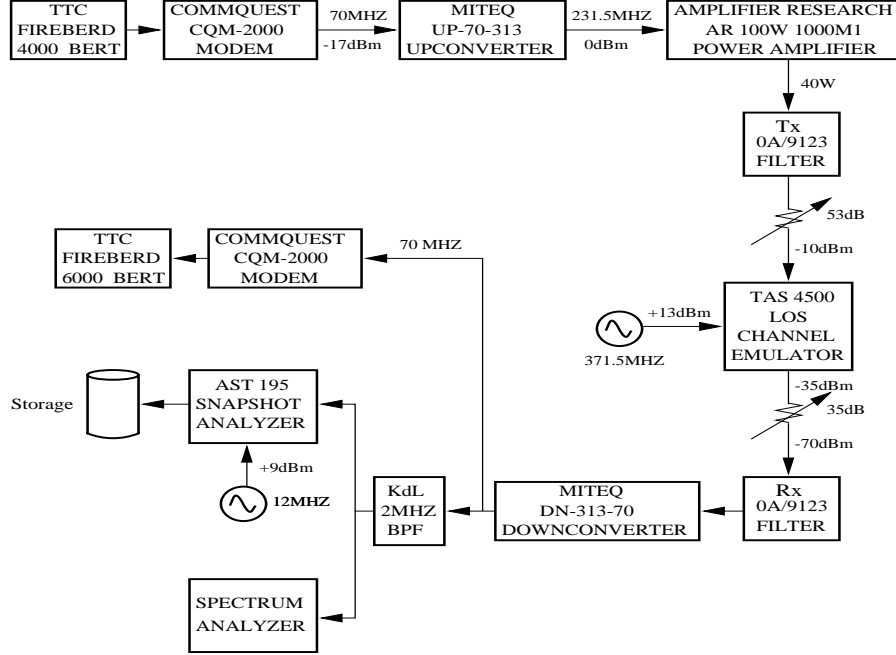


Figure 7.1: Equipment configuration used for the collection of the multipath emulated data files.

three-path files; and UHF channel files. Table 7.1 lists reference data files used to determine the effects of the OA/9123, the TAS4500, and the AST195 Snapshot Analyzer on the received sampled data.

The bandlimiting of the OA/9123 is an undesirable effect that corrupts the resolution of the channel estimates. The OA/9123 consists of four mechanically-tuned cavity filters that have a 1 dB bandwidth of approximately 900 kHz at 231.5 MHz. This bandlimiting generates intersymbol interference extending over several symbols. Over-the-air Tx operation in the San Diego area at 1 Mbps requires an OA/9123 as a post-selection filter to prevent the jamming of other nearby receivers. Over-the-air Rx operation requires an OA/9123 as a pre-selection filter to reduce the effects of adjacent channels when the Rx signal strength is low (the so-called “co-site” or “adjacent channel” EMI problem). During the several weeks that these data sets were collected, the OA/9123 filters were retuned several times, so decorrelating their effects from the over-the-air tests does not appear to be possible. As will be seen in the

next chapter, future experiments should consider either a reduced data rate or a different filter to improve the resolution of the channel estimates.

Tables 7.2 and 7.3 list eighteen static multipath data files with various delays $\Delta\tau$, losses L , and phases $\Delta\phi$, relative to the direct path. The purpose of these files is to determine the resolvable delays and losses and the accuracy of the channel estimation procedures.

Table 7.4 lists six fading multipath data files. Each multipath component is a Rayleigh fading signal. The second path is 20 microseconds delayed from the direct path while the third path is 40 microseconds delayed from the direct path. The fade rates and the losses of each multipath are varied among the data files. The purpose of these data files is to determine the accuracy of the channel estimation procedures in estimating the fade rates of the individual multipaths.

Table 7.5 lists the final three data files collected using the TAS 4500 RF Channel Emulator. These were collected using three UHF Channels (numbered 1, 2, 3) common to various Marine Corps Urban and Naval environments. These channels include a slow flat fading channel (UHF Channel 1) common to ship to ship communications, a slightly frequency selective channel with moderate fading (UHF Channel 2) common to ship to shore/air communications, and a highly frequency selective channel with dynamic fading (UHF Channel 3) common to mobile vehicle communications in urban environments.

Table 7.1: Reference Data Files

File Name	Signal	OA/9123 Tx	TAS 4500	OA/9123 Rx
ref0.snp	BPSK	bypass	bypass	bypass
ref1.snp	BPSK	in-line	bypass	in-line
ref2.snp	BPSK	bypass	bypass	in-line
ref3.snp	BPSK	in-line	bypass	bypass
ref4.snp	BPSK	in-line	in-line	in-line
ref5.snp	none	in-line	in-line	in-line
ref6.snp	CW	in-line	in-line	in-line

Table 7.2: Static Multipath Emulated Data Files (1–9)

File Name	Paths	$\Delta\tau$ μs	L dB	$\Delta\phi$ deg
tas4500_1.snp	Direct	0	0	0
	Second	0.01	0	30
	Third	0.02	0	270
tas4500_2.snp	Direct	0	0	0
	Second	0.10	0	30
	Third	0.20	0	270
tas4500_3.snp	Direct	0	0	0
	Second	0.25	0	30
	Third	0.50	0	270
tas4500_4.snp	Direct	0	0	0
	Second	0.50	0	30
	Third	1.00	0	270
tas4500_5.snp	Direct	0	0	0
	Second	0.75	0	30
	Third	1.50	0	270
tas4500_6.snp	Direct	0	0	0
	Second	1.00	0	30
	Third	2.00	0	270
tas4500_7.snp	Direct	0	0	0
	Second	1.25	0	30
	Third	2.50	0	270
tas4500_8.snp	Direct	0	0	0
	Second	1.50	0	30
	Third	3.00	0	270
tas4500_9.snp	Direct	0	0	0
	Second	1.75	0	30
	Third	3.50	0	270

Table 7.3: Static Multipath Emulated Data Files (10–18)

File Name	Paths	$\Delta\tau$ μs	L dB	$\Delta\phi$ deg
tas4500_10.snp	Direct	0	0	0
	Second	2	0	30
	Third	4	0	270
tas4500_11.snp	Direct	0	0	0
	Second	5	0	30
	Third	10	0	270
tas4500_12.snp	Direct	0	0	0
	Second	10	0	30
	Third	20	0	270
tas4500_13.snp	Direct	0	0	0
	Second	100	0	30
tas4500_14.snp	Direct	0	0	0
	Second	20	-1.0	30
	Third	40	-2.0	270
tas4500_15.snp	Direct	0	0	0
	Second	20	-5.0	30
	Third	40	-10.0	270
tas4500_16.snp	Direct	0	0	0
	Second	20	-7.5	30
	Third	40	-15.0	270
tas4500_17.snp	Direct	0	0	0
	Second	20	-12.5	30
	Third	40	-17.5	270
tas4500_18.snp	Direct	0	0	0
	Second	20	-20.0	30
	Third	40	-30.0	270

Table 7.4: Dynamic Multipath Emulated Data Files

File Name	Paths	Fading	f_D Hz	$\Delta\tau$ μs	L dB
tas4500_19.snp	Direct	Rayleigh	1	0	0
	Second	Rayleigh	1	20	-5
	Third	Rayleigh	1	40	-10
tas4500_20.snp	Direct	Rayleigh	5	0	0
	Second	Rayleigh	5	20	-5
	Third	Rayleigh	5	40	-10
tas4500_21.snp	Direct	Rayleigh	10	0	0
	Second	Rayleigh	10	20	-5
	Third	Rayleigh	10	40	-10
tas4500_22.snp	Direct	Rayleigh	20	0	0
	Second	Rayleigh	20	20	-5
	Third	Rayleigh	20	40	-10
tas4500_23.snp	Direct	Rayleigh	40	0	0
	Second	Rayleigh	40	20	-5
	Third	Rayleigh	40	40	-10
tas4500_24.snp	Direct	Rayleigh	10	0	0
	Second	Rayleigh	20	20	-5
	Third	Rayleigh	40	40	-10

Table 7.5: UHF Channels Emulated Data Files

File Name	Paths	Fading	f_D Hz	$\Delta\tau$ μs	L dB
tas4500_uhfch1.snp	Direct	Rician	1		
	Second	Rayleigh	10	0.01	-6
tas4500_uhfch2.snp	Direct	Rician	10		
	Second	Rayleigh	10	0.07	-5
	Third	Rayleigh	10	0.80	-15
tas4500_uhfch3.snp	Direct	Rician	25		
	Second	Rayleigh	25	0.90	-3
	Third	Rayleigh	25	5.10	-9

7.2 HMMWV Data Files

This section describes a set of data files collected from a HMMWV driving through San Diego residential and urban environments on 16 January, 1998. The HMMWV was configured as a continuous transmitter. SPAWAR System Center, San Diego (SSC-SD) Building 379 was configured as the continuous receive and data collection site using the same equipment described in Section 7.1 (See Figures 7.3 and 7.4). A 511 pseudorandom bit pattern was continuously transmitted from the mobile HMMWV using BPSK at 231.5 MHz, 40 Watts, 999,995 bps. The signal was sampled using the AST195 at 12 Msps to obtain approximately 5.6 seconds of contiguous data. Figure 7.2 is a photograph of the HMMWV in front of SSC-SD Building 379.



Figure 7.2: Picture of the HMMWV in front of the SSC-SD, Building 379 receive site.

The position of the mobile vehicle was recorded using the SABRE GPS beacon system that also was transmitting on UHF LOS. A SABRE GPS beacon was installed in the HMMWV and configured to transmit the (encoded) GPS position of the HMMWV once a minute on UHF LOS at 270.75 MHz. The GPS receive antenna was mounted on top of the HMMWV. The SABRE beacon 20 Watt transmit output was fed into the OA/9123 UHF LOS multi-coupler that fed the UHF LOS omni-directional antenna (Antenna Products DPV-37) as shown in Figure 7.3. The received GPS beacon information was displayed on a JMCIS terminal giving the HMMWV location, bearing, velocity, and past track information.

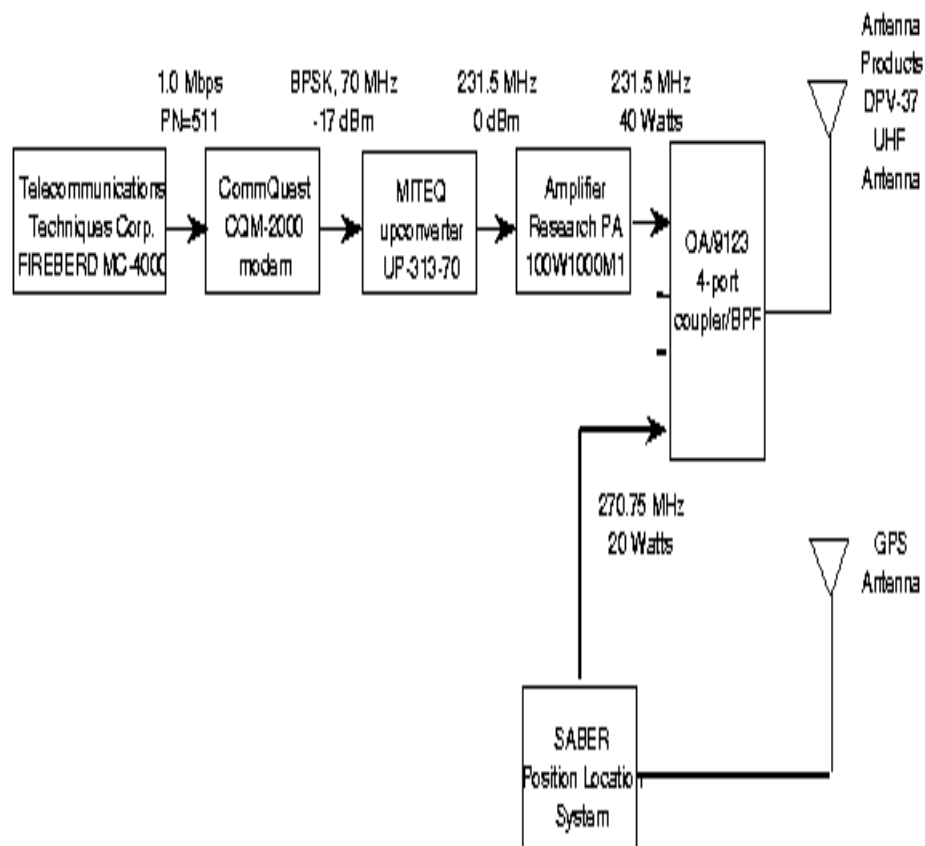


Figure 7.3: HMMWV transmitter configuration.

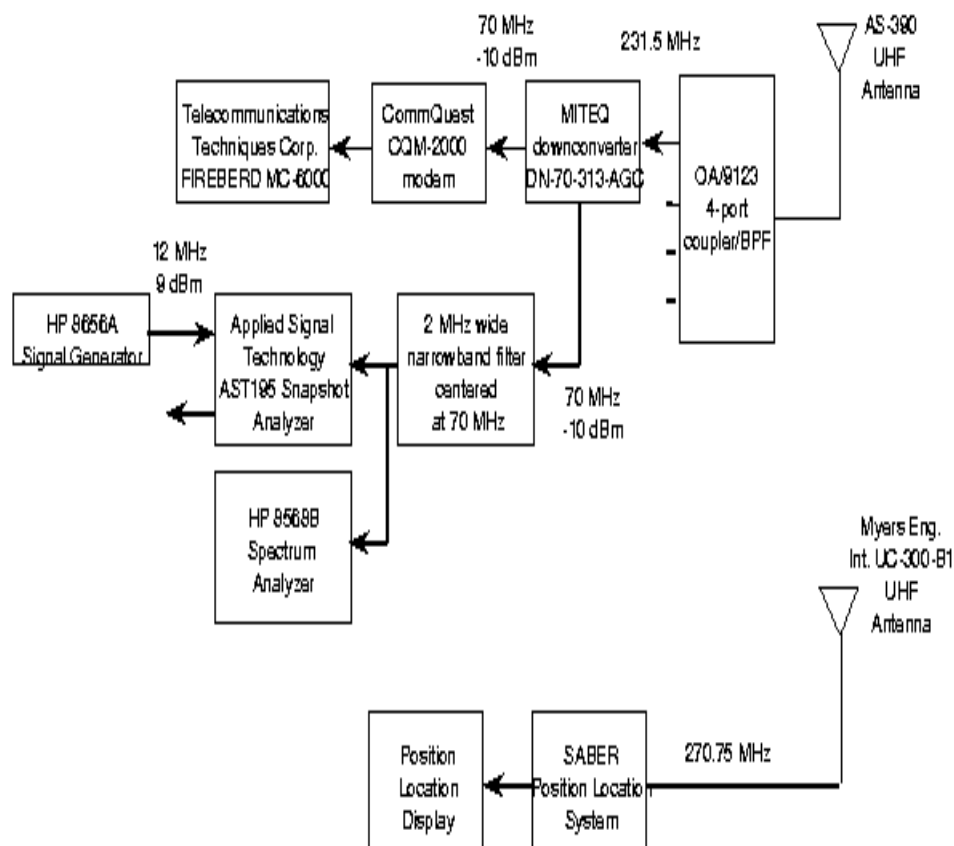


Figure 7.4: SPAWAR System Center, San Diego (SCC-SD) Building 379 receiver configuration.

Table 7.6 lists the data files collected on 16 January, 1998 during a 36-minute drive from SSC-SD Building 379 to Naval Station San Diego (NAVSTASD) pier 8. The signal levels were fluctuating such that the A/D converter clipped some portions. The relative degree of A/D clipping is indicated in Table 7.6 along with other figures of merit. The speed of the HMMWV is only accurate to ± 5 mph.

Table 7.6: Mobile vehicle measured data files.

File Name	Location	Bearing	Range mi	Speed mph	Rx level	A/D clipping	Fading
hmmwv1306.snp	Catalina Blvd.	north	1.0	20	good	some	dynamic
hmmwv1313.snp	Catalina Blvd.	north	1.2	30	good	low	dynamic
hmmwv1318.snp	Catalina Blvd.	north	3.2	20	low	low	dynamic
hmmwv1325.snp	I-5 (near I-8)	south	5.0	55	good	some	dynamic
hmmwv1328.snp	I-5 (near "S")	east	5.2	55	good	some	dynamic
hmmwv1330.snp	I-5 (past 94)	south	6.2	55	low	high	?
hmmwv1333.snp	28th Street	west	6.5	25	good	some	slow
hmmwv1335.snp	Harbor Blvd.	south	6.9	0	good	some	static
hmmwv1338.snp	NAVSTASD	south	7.4	10	good	some	dynamic
hmmwv1340.snp	NAVSTASD	south	7.9	5	good	some	slow
hmmwv1342.snp	NAVSTASD-Pier 8	west	7.6	0	good	high	slow

Figure 7.5 maps the route driven. From 1306 to 1320, the HMMWV traveled away from SSC-SD Building 379 on Catalina Boulevard. This route traverses a residential community consisting of one-story wood houses lining both sides of the two-lane road. From 1320 to 1332, the HMMWV traveled on typical interstate freeways at approximately 55 mph. During this time, the HMMWV drove through downtown San Diego from 1328 to 1330. Downtown San Diego is home to 20-30 high rise buildings and numerous multiple story office buildings. From 1332 to 1340, the HMMWV navigated relatively small streets near and on NAVSTASD. NAVSTASD has numerous two- to four-story concrete buildings close to the waterfront. Navy ships line the piers on the waterfront.



Figure 7.5: Map with HMMWV's position track from SSC-SD, Building 379 to NAVSTASD, Pier 8.

7.3 Navy Ship Data Files

This section describes a set of data files collected from the USS Princeton (CG59) while departing San Diego Bay on 21 January, 1998 and off the coast of Point Loma on 22 January, 1998. These data sets are representative of the Naval littoral environment for the Military UHF band. Ranges were extended because of a strong and persistent ducting condition that existed during these tests. The transmit equipment from the HMMWV described in Section 7.2 was installed on the USS Princeton with the exception of the OA/9123 and the UHF LOS antenna. The existing OA/9123's and the existing UHF LOS antennas (AS-4163) on the USS Princeton were utilized. In addition, the GPS receive antenna was mounted on the ship topside with a low noise amplifier to drive the 150 feet of cable down to the radio room.

The USS Princeton was configured as a continuous transmitter. SPAWAR System Center, San Diego (SSC-SD) Building 379 was configured as the continuous receive and data collection site. As before, a 511 pseudorandom bit pattern was continuously transmitted from the USS Princeton using BPSK at 231.5 MHz, 40 Watts, 999,995 bps. This was transmitted out of the ship's port side AS-4163 antenna. The signal was sampled using the AST195 at SSC-SD Building 379 at 12 Msps to obtain approximately 5.6 seconds of contiguous data. Figure 7.6 is a file photograph of a Ticonderoga Class Guided Missile Cruiser that is similar to the USS Princeton.

Position of the mobile ship was recorded using the SABRE GPS beacon system transmitting on UHF LOS at 260.625 MHz. The SABRE GPS beacon was installed on the USS Princeton and configured to transmit the (encoded) GPS position of the ship once a minute through an unused port on the ship's existing OA/9123 UHF LOS multicoupler that fed the ship's existing UHF LOS omni-directional antenna (starboard side AS-4163). The received GPS beacon information was displayed on a JMCIS terminal giving the present ship location, bearing, velocity, and past track information. Figures 7.7, 7.8, and 7.9 show the ship's location during the experiment conducted on 21-22 January, 1998. The effects of strong ducting propagation condition can be seen by the 90 nmi range obtained by the SABRE GPS Beacon during the night of 21 January, 1998 over UHF LOS in Figure 7.8. The ship antenna height is approximately 100 feet above sea level. The receiver antenna at SSC-SD, Building 379 is approximately 350 feet above sea level. These heights give an LOS communication range of approximately 35 nmi.

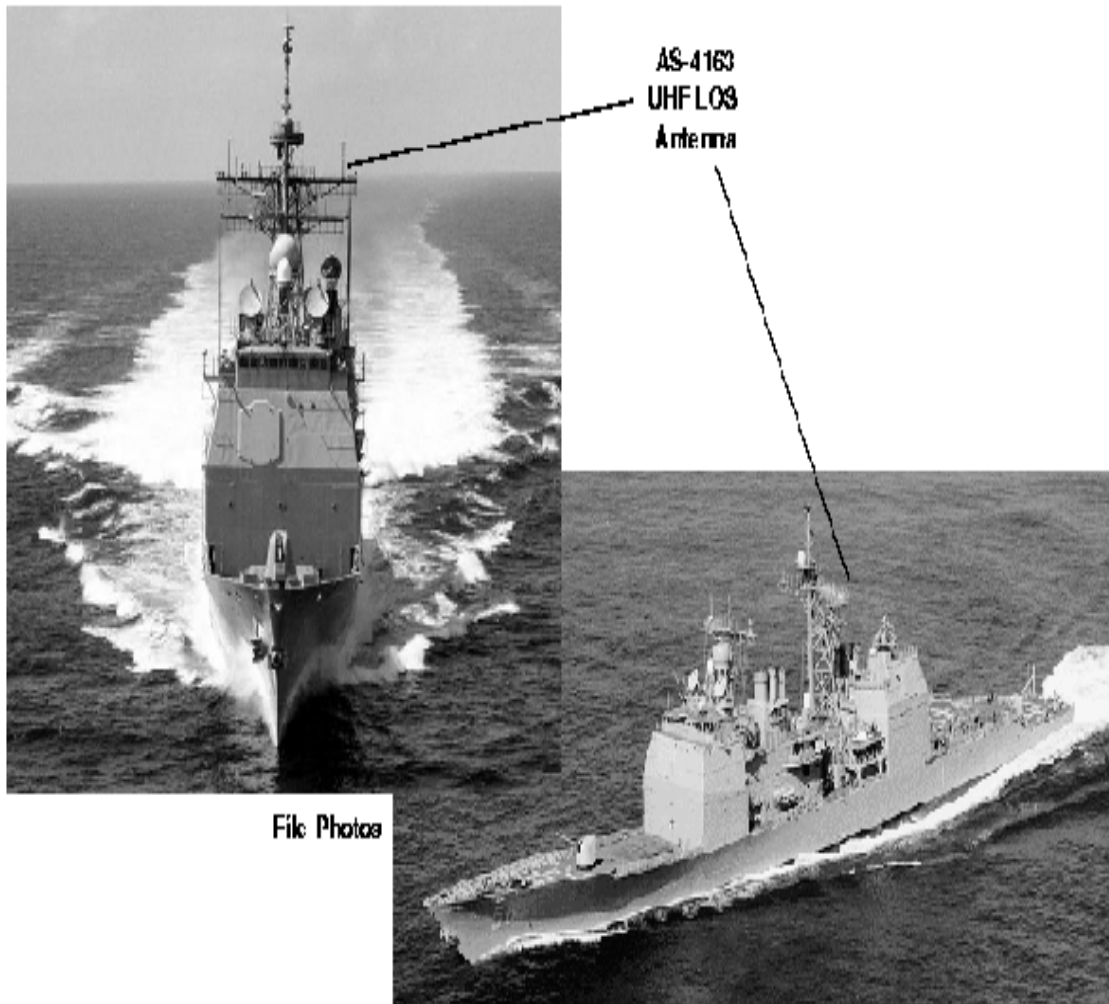


Figure 7.6: File Photograph of a Ticonderoga Class Guided Missile Cruiser used as a mobile ship transmitter.

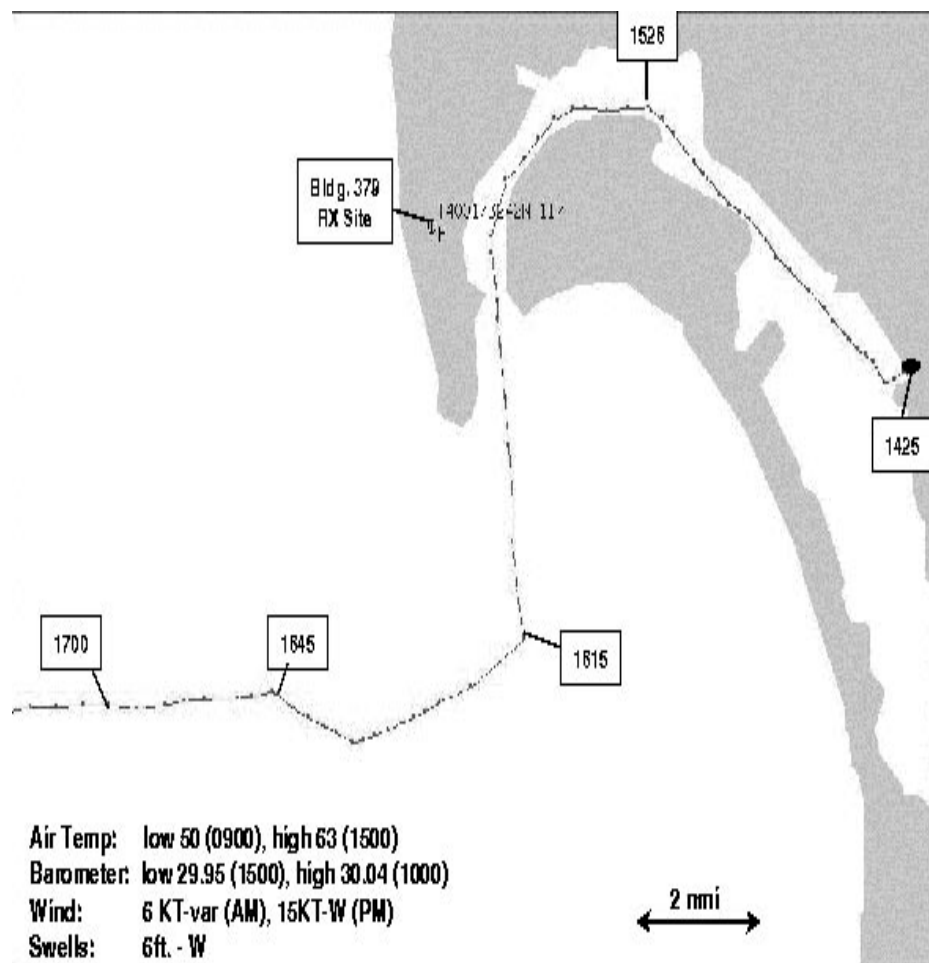


Figure 7.7: Position tracks for the USS Princeton on 21 January, 1998 departing Port of San Diego.

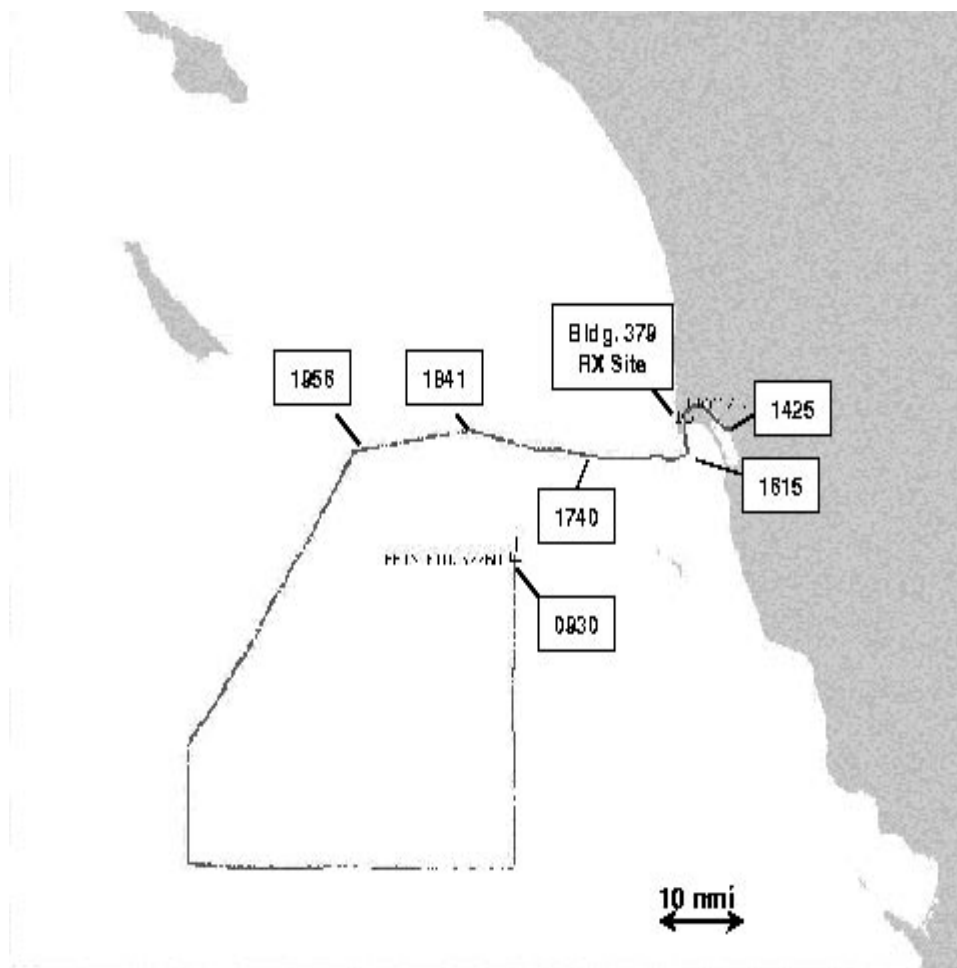


Figure 7.8: Position tracks for the USS Princeton on 21 January, 1998.

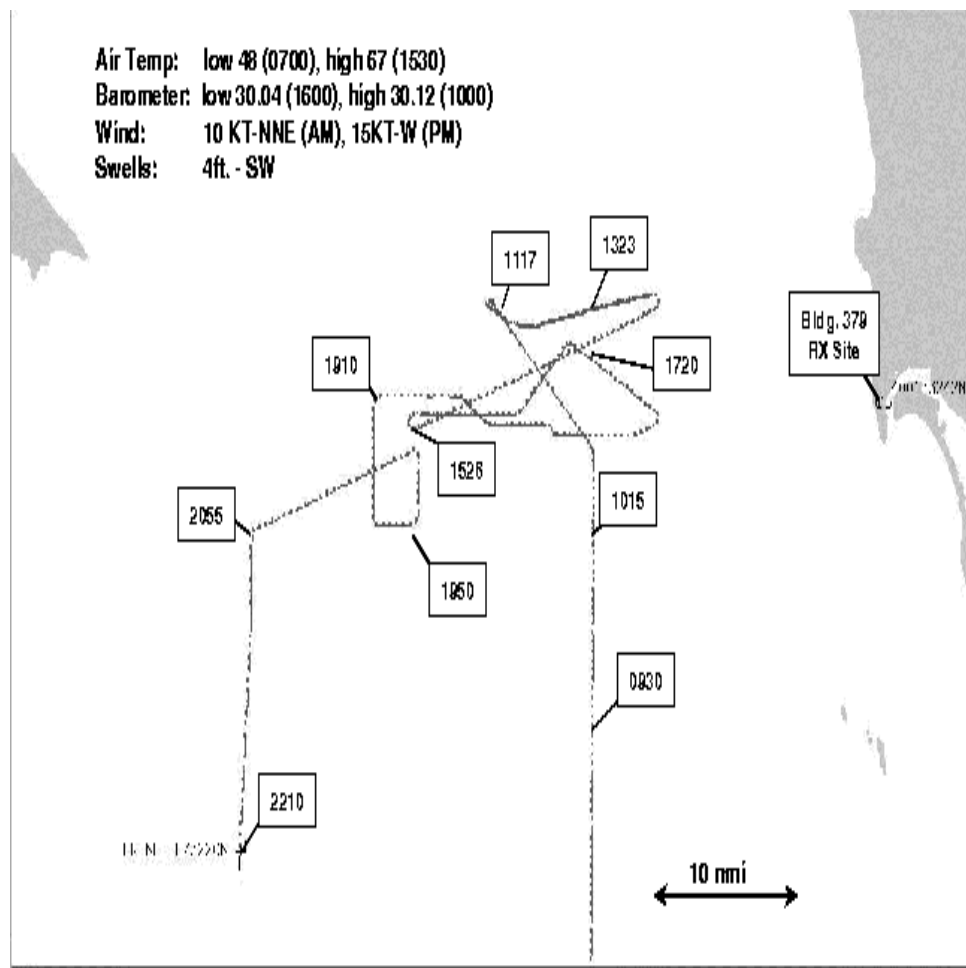


Figure 7.9: Position tracks for the USS Princeton on 22 January, 1998.

Table 7.7 lists the data files collected on 21-22 January, 1998 at SSC-SD Building 379. Very little A/D clipping of the signal was observed in these files. Some dramatic multipath fading was evident while the ship was in San Diego Bay. In contrast, slow flat fading was observed in blue waters. The transmit antenna was on the port side of the ship on the end of a yard arm. As such, there were several times when the mast would partially block the transmitted signal to create deep and rapid fades. The maximum range when unobstructed for 1 Mbps was typically 40 nmi during this test period. This is slightly longer than anticipated due to the strong ducting condition.

Table 7.7: Ship data files. No A/D clipping.

File Name	Location	Bearing deg	Range mi	speed KT	Rx dBm	Fading
ship21jan0843.sn timer	Pier 8	290	6.5	0	-73	very slow
ship21jan1459.sn timer	Coronado Bridge	320	4.7	5	-68	dynamic
ship21jan1518.sn timer	in SD Bay	318	3.5	5	-69	slow
ship21jan1607.sn timer	Ballast Point	171	3.8	15	-81	slow
ship21jan1642.sn timer	SW of Point Loma	311	5.0	8	-70	slow
ship21jan1739.sn timer	W of Point Loma	280	12.0	12	-71	slow
ship21jan1824.sn timer	W of Point Loma	285	22.4	12	-79	slow
ship21jan1936.sn timer	W of Point Loma	262	36.3	14	-94	slow
ship21jan1956.sn timer	W of Point Loma	216	40.5	12	-105	slow
ship22jan1117.sn timer	W of Point Loma	309	26.8	11	-83	slow
ship22jan1507.sn timer	W of Point Loma	247	31.0	18	-90	slow
ship22jan1526.sn timer	W of Point Loma	13	33.0	8	-101	slow
ship22jan1757.sn timer	W of Point Loma	0	22.9	0	-83	slow
ship22jan1800.sn timer	W of Point Loma	0	22.9	0	-81	slow

Chapter 8

Emulated & Over-the-Air Channel Estimates

In this chapter, the ship and the HMMWV channel soundings are analyzed to extract channel estimates for these military scenarios. The channel model is taken to be the quadrature-modulation fading simulator (QMFS) with Delay-Spread function (See Chapter 3)

$$h(t, \tau) = \sum_{n=1}^N a_n(t) \delta(t - \tau_n).$$

So a QMFS specifies N , the delays τ_n 's, and fading processes $\{a_n(t)\}$'s. More generally, the distribution of the delays and Doppler frequencies will be determined from the scattering function $P(f, \tau)$. The Fourier transform in t of $h(t, \tau)$ produces the Delay-Doppler function $U(f, \tau)$. Its covariance yields the scattering function (See Chapter 2):

$$P(f, \tau) = E[|U(f, \tau)|^2].$$

Links between the scattering function and delay-Doppler distribution for the QMFS are discussed in Chapter 3. For fixed τ_n 's and $\{a_n(t)\}$'s JWSS and uncorrelated, Example 3.3.2 shows

$$P(f, \tau) = \sum_{n=1}^N P_{a_n a_n}(f) \delta(\tau - \tau_n).$$

So the power spectrum of each fading process registers at its corresponding delay. More generally, Example 3.3.3 admits random delays to give

$$P(f, \tau) = \sum_{n=1}^N P_{a_n a_n}(f) p_{\tau_n}(\tau).$$

So each reflector registers a “blob” in the scattering function of its delay-Doppler distribution. Section 3.3 makes explicit our belief system that the converse is true: Well-separated “blobs” in the scattering function register the local delay-Doppler distribution. It is these blobs that can test claims such as: “the first path is Ricean and the second path is Rayleigh”.

This approach is confounded by at least three factors. First, we are working from digital data so our channel functions are smeared by the raised cosine filter $x_{\text{RC}}(t)$. Section 3.5 shows that the digital baseband Delay-Doppler function $U(f, k)$ links to $U(f, \tau)$ as

$$U_B(f, k) = x_{\text{RC}} *_{\tau} U(f, k\tilde{T}).$$

The baseband digital scattering function $P_B(f, k)$ is then

$$P_B(f, k) = x_{\text{RC}}^2 *_{\tau} P(f, k\tilde{T}).$$

Thus, the scattering function is smeared by the raised cosine filter. — in theory. The practical aspects are the second factor: we only have finite samples of noisy, received signals distorted by the filters — the OA/9123 Tx and Rx — of the real system. Third, we do not have the baseband Delay-Spread function h_B — only the estimates h_{PN} , and h_{FRGM} from Chapter 5 and h_{AF} from Chapter 6. Given these factors, it is worthwhile to ask: *How do these estimators compare on laboratory data?* To answer is pretty simple. Estimates of the Delay-Spread and scattering function are compared to the known channel parameters of the TAS4500 RF Channel Emulator.

To establish this ground truth, we start by calibrating our estimators on the RF laboratory data. Section 8.1 starts by establishing an end-to-end *spurious-free dynamic range* (SFDR) for the RF system without the TAS4500 channel emulator and the OA/9123 multicoupler (See Chapter 7 and Figures 7.1). The SFDR sets a threshold that prevents system-generated spikes to register as possible reflectors. Section 8.2 discusses the system distortion induced by including the OA/9123 multicoupler. Section 8.3 adds the TAS4500 and then assesses the SFDR.

With these estimates of the SFDR, we turn to registering the pulse shape and amplitude. Section 8.4 uses a benign emulation to show the precision that h_{PN} , h_{RFGM} and h_{AF} register amplitude levels despite this distortion. Section 8.5 assesses these estimators on a more challenging emulation. It is shown that the channel estimation is affected by the demodulation schemes. The adaptive filter estimate h_{AF} also adapts the demodulator — and obtains an excellent channel registration. The demodulation for h_{PN} , h_{RFGM} is not adaptive. Consequently, these channel estimates may be corrupted by the demodulator. Section 8.6 verifies this claim and points out that such problematic demodulation can be flagged by the power spectrum. With these calibrations in place, Sections 8.7 and 8.8 compare the channel estimators on emulated time-variant channels with fade rates from 1–40 Hertz. The AF filter continues to be the best estimate overall and gives excellent estimates of the scattering function.

The final sections step from the laboratory to the real world where two datasets from Chapter 7 are analyzed. Section 8.9 examines transmissions from a mobile HMMWV operating in an urban environment. Section 8.10 presents a ship-to-shore channel. A simple two-path QMFS model captures most of this channel whereas more complex model is needed to model the HMMWV channel.

8.1 Spurious-Free Dynamic Range (SFDR)

This section estimates the spurious-free dynamic range (SFDR) for each channel estimator using the 8-bit sampled data from `ref0.snp`. This SNP file includes all RF components except the TAS4500 channel emulator and the OA/9123 coupler. These SNP datasets contain the received RF signal folded down by undersampling. That is, the IF frequency is approximately $f_c=70$ MHz, and the sample rate is approximately $f_s=12$ MHz so the negative 1 MHz band is centered at 2 MHz. The processing for h_{PN} , h_{GM} , h_{FRGM} is:

1. Get the PN sequence \mathbf{s} of length $N_s=511$:

$$\mathbf{s} = \text{pn_src}(9, 1041, N_s, 1).$$

2. Get a sequence of real-valued channel snapshots \mathbf{y}_{RF} .

3. Hilbert-transform Demodulation: Extract the narrow-band phase ϕ of \mathbf{y}_{RF}^2 at 4 MHz to phase-cancel the Hilbert transform $H(\mathbf{y}_{\text{RF}})$ to get the demodulated signal:

$$\mathbf{y} = H(\mathbf{y}_{\text{RF}})e^{-j\phi/2}.$$

4. Sub-Channel Estimation: The oversampling factor is $O_s=12$. Channel estimates are pulled out of the demodulated vector \mathbf{y} by reshaping the vector \mathbf{y} into 12 sub-channels. Each sub-channel has only one sample per symbol. Then the additive noise is uncorrelated on each sub-channel, zero-filling \mathbf{s} is unnecessary, and estimators described in Chapter 5 may be applied to each sub-channel. The resulting channel estimates for each of the sub-channels are reshaped back to a vector giving an estimate of the Input Delay-Spread function $h(t, \tau)$.

The processing for h_{AF} is:

1. Get a segment of the real-valued channel snapshots \mathbf{y}_{RF} .
2. Bandshift \mathbf{y}_{RF} such that the negative 1 MHz band centered at the nominal frequency of -2MHz is centered at DC, lowpass filter with the square-root raised cosine filter, and possibly decimate.
3. Generate repeated patterns of the PN sequence to match the time series in Step 2.
4. Use the sub-channel estimation technique described in Chapter 6 matched to the oversampling factor determined in Step 2.

Figure 8.1 plots the power spectrum of \mathbf{y}_{RF} from ref0.snp estimated from the first 300 snapshots. The input power level is $P_i=-15$ dBm and the sample rate is approximately $f_s=12$ MHz. This noise floor is -40 dB from signal but is corrupted by the harmonic of the carrier frequency at 4 MHz that is -25 dB from the signal.

Figures 8.2 and 8.3 plot the PDP estimate obtained from $h_{\text{PN}}(t, \tau)$ and $h_{\text{FRGM}}(t, \tau)$. Our belief is that $h_B(t, \tau)$ is approximated by $h_{\text{PN}}(t, \tau)$ and $h_{\text{FRGM}}(t, \tau)$ so that the power delay profile — smeared by the raised cosine — is proportional to the time-average of the estimates:

$$p_\tau * x_{\text{RC}}^2(\tau) \propto \int_{-\infty}^{\infty} |h_{\text{PN}}(t, \tau)|^2 dt \quad \text{and} \quad \int_{-\infty}^{\infty} |h_{\text{FRGM}}(t, \tau)|^2 dt.$$

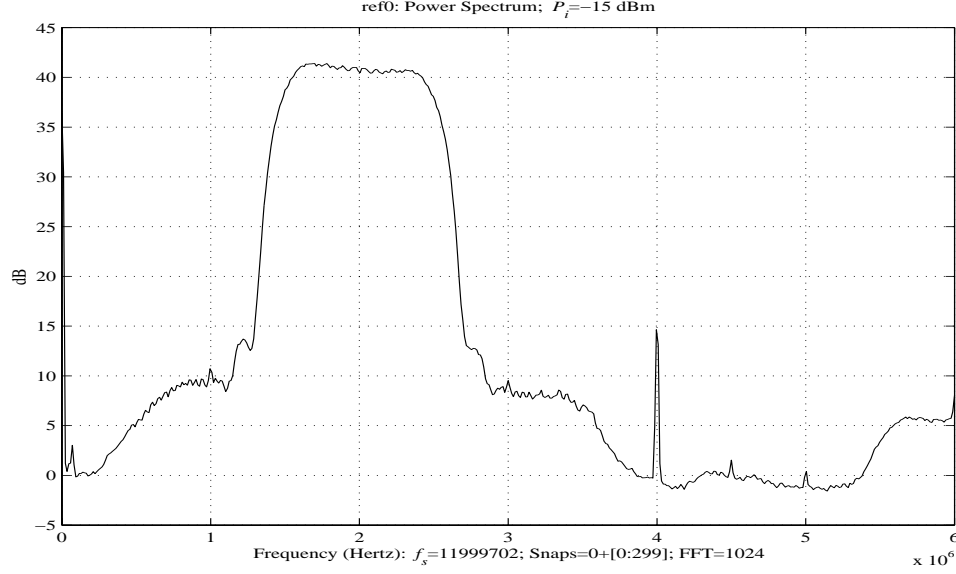


Figure 8.1: Power spectrum estimate of ref0.snp

PN Estimate: Figure 8.2 shows the PN estimate of the PDP. The x -label “Snaps = [10:30:300]; |Snaps| = 30” means the PN estimate for the PDP was computed by averaging 30 snapshots indexed by 10, 40, 70, ..., 300. To make the channel estimate for the n th snapshot, we grab snapshots $n + [-1 : 1]$, demodulate, PN filter, and select the n th snapshot. The plot shows the “direct” path on the right, the mean noise floor at approximately -52 dB, and several little peaks. These little peaks are system artifacts — there is no channel emulator or converters. Thus, the SFDR for the PN estimate is approximately -30 dB.

FRGM Estimate: Figure 8.3 shows the FRGM estimate of the PDP. The regularization parameter $\gamma=0.001$ has little effect on the noise floor. The “7 snapshot window” means the channel estimate for the n th snapshot starts by grabbing snapshots $n + [-3 : 3]$, demodulating, weighting by a Hamming window, applying the regularization filter using the FFT, and selecting the n th snapshot. We make explicit that the Hamming window was not used in Chapter 5 but employed in this chapter. The window permits a small regularization parameter $\gamma_0=0.001$ to be used and keeps h_{FRGM} closer to the inverse filter. Figure 8.3 shows a noise floor at approximately -37 dB with a single spurious peak. This sets SFDR for RFGM at -30 dB.

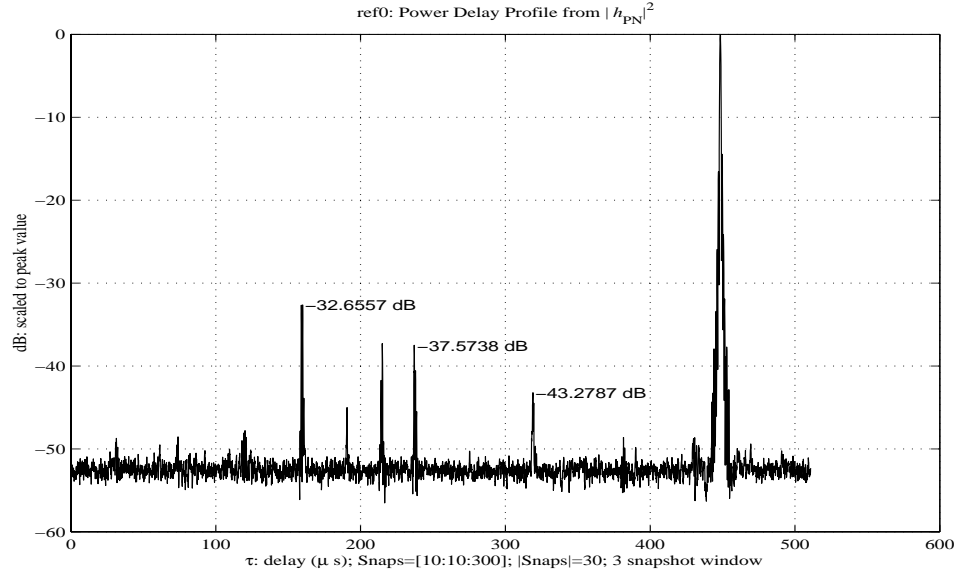


Figure 8.2: PN estimate of the power delay profile for ref0.snp.

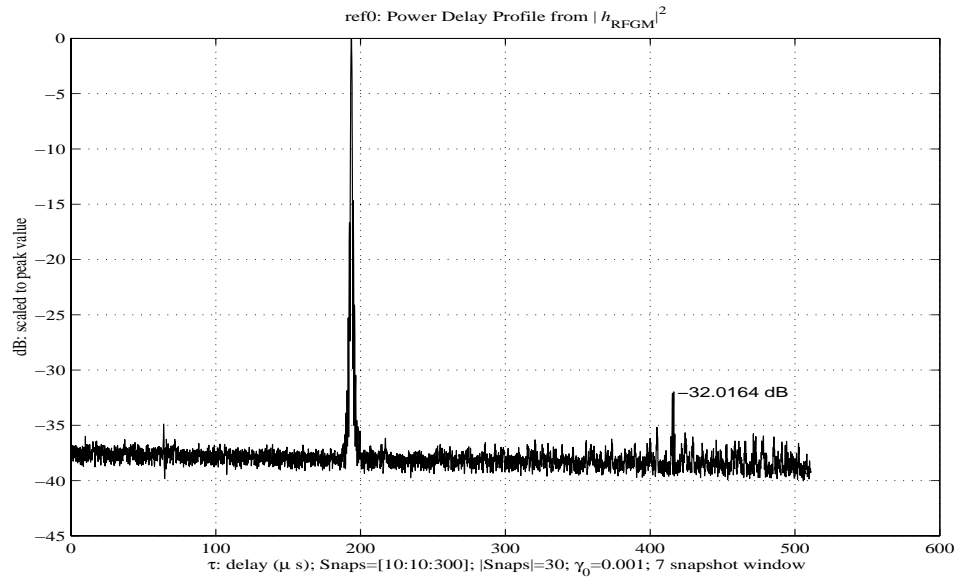


Figure 8.3: RFGM estimate of the power delay profile for ref0.snp.

AF Estimate: Figure 8.4 is the AF estimate of the PDP. For computational reasons, the delay spread is restricted to a $100\ \mu\text{s}$ window. To accommodate this window, the signal was further decimated by 2 to get the $O_s=6$. Within this window, the noise floor is approximately -62 dB. The trailing peak sets the SFDR=-50 dB. This low noise is likely due to the lowpass filtering in Step 2 of the AF method, and the narrow $100\ \mu\text{s}$ window of the AF estimate. Making the adaptive filter longer not only increases the computational burden, but also increases gradient noise thereby increasing the noise floor and the related SFDR. Figure 8.4 clearly shows the raised cosine filter centered on the “direct” path. Both the PN and FRGM estimators display similar characteristics when plotted on the same horizontal scale.

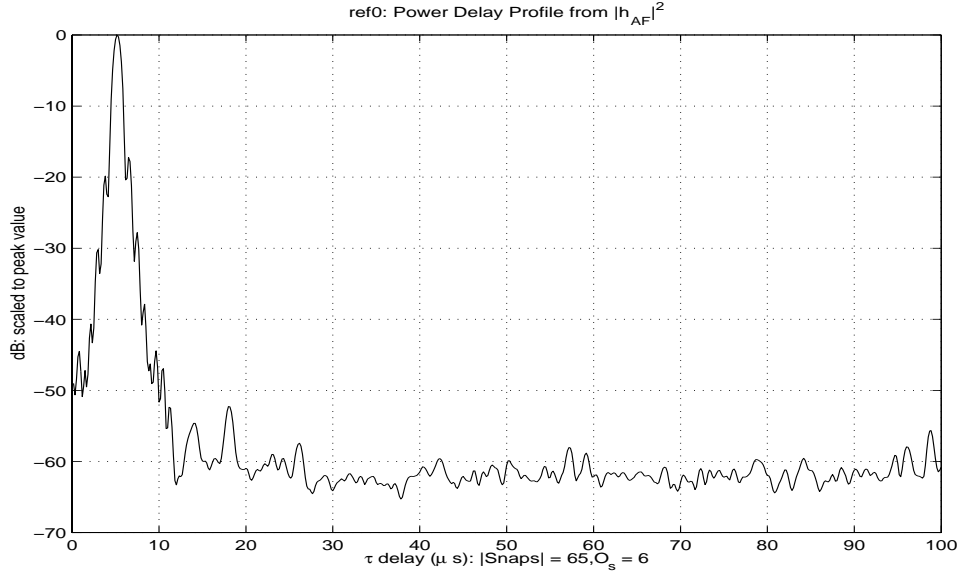


Figure 8.4: AF estimate of the power delay profile for ref0.snp.

8.2 Distortion of the Raised Cosine

The SNP file `ref1.snp` extends `ref0.snp` by including the OA/9123 multicoupler (this also includes the up- and down-converters). Adding these RF components decreases the out-of-band spectral energy but slightly distorts the signal of interest. Figure 8.5 plots the power spectrum of \mathbf{y}_{RF} from `ref1.snp` estimated from the first 300 snapshots. Comparison with Figure 8.1 shows distortion across the passband, a 5 kHz reduction of the lower band, and a 10 kHz reduction of the upper band. This distorts the raised cosine filter that registers each channel delay. Figure 8.6 shows the resulting distortion. Compared to Figure 8.4, we see that this distortion raises the trailing side lobes and limits the path resolution. At -20 dB, the pulse is $3.7 \mu\text{s}$ wide. We adopt -20 dB as the noise floor and $3.7 \mu\text{s}$ as the time resolution.

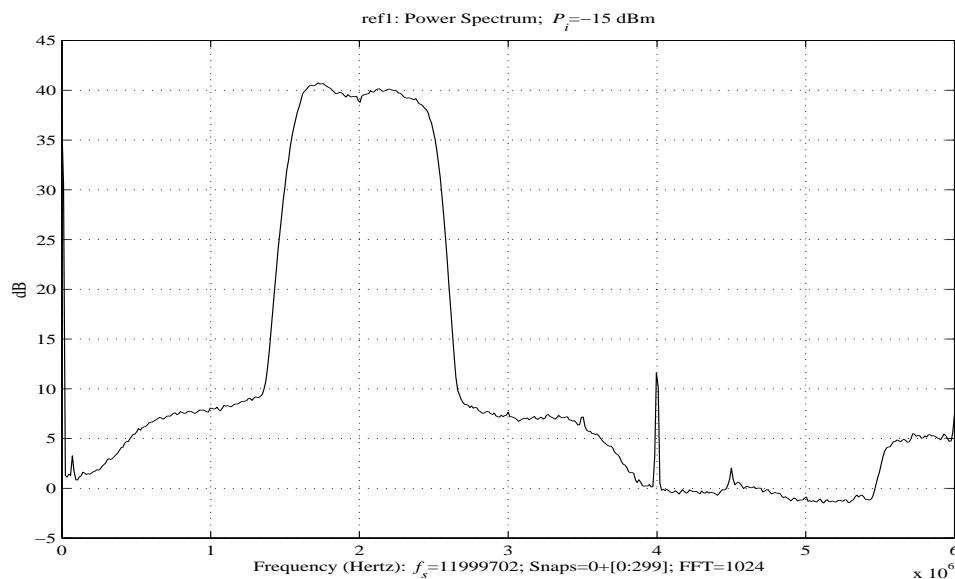


Figure 8.5: Power spectrum estimate of `ref1.snp`

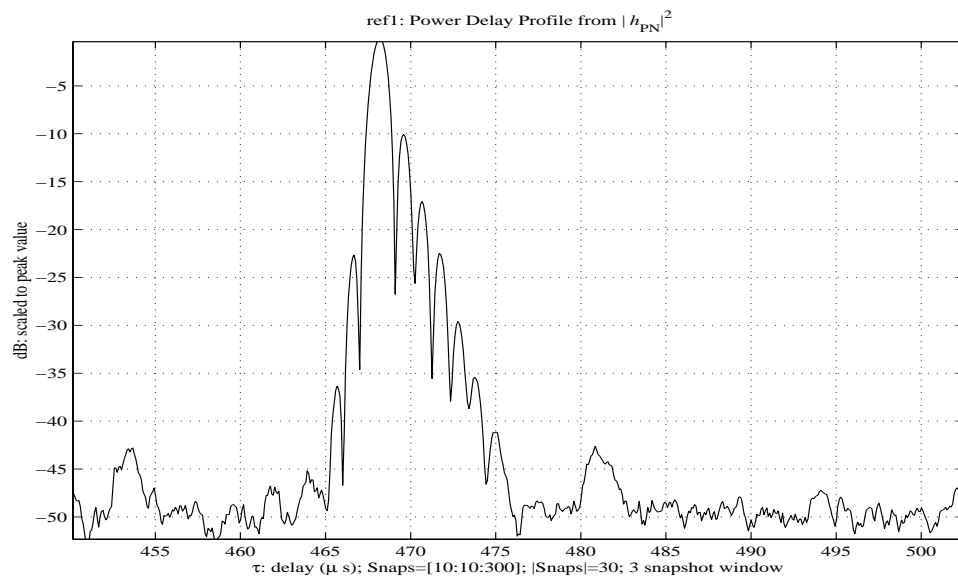


Figure 8.6: PN estimate of the power delay profile for ref1.snp. Close-up of the distorted raised cosine filter.

8.3 TAS4500: SFDR & Pulse Distortion

Section 8.1 established the noise floor without the OA/9123 coupler or the TAS4500 channel emulator. Section 8.2 added only the OA/9123 coupler to show the distortion of the raised cosine. In this section, the TAS4500 channel emulator is added along with the OA/9123 to get the RF full channel emulation

We start by noting the “noise only” SNP file (ref5.snp) has an input power level of $P_i = -43$ dBm. Next, a CW is transmitted to get a nominal SNR. Figure 8.7 shows the power spectrum of ref6.snp estimated from the first 300 snapshots. The input power level is $P_i = -18$ dBm giving an SNR of +25 dB. The spectral noise floor is nearly -50 dB from signal but the harmonic of the carrier frequency at 4 MHz is -40 dB.

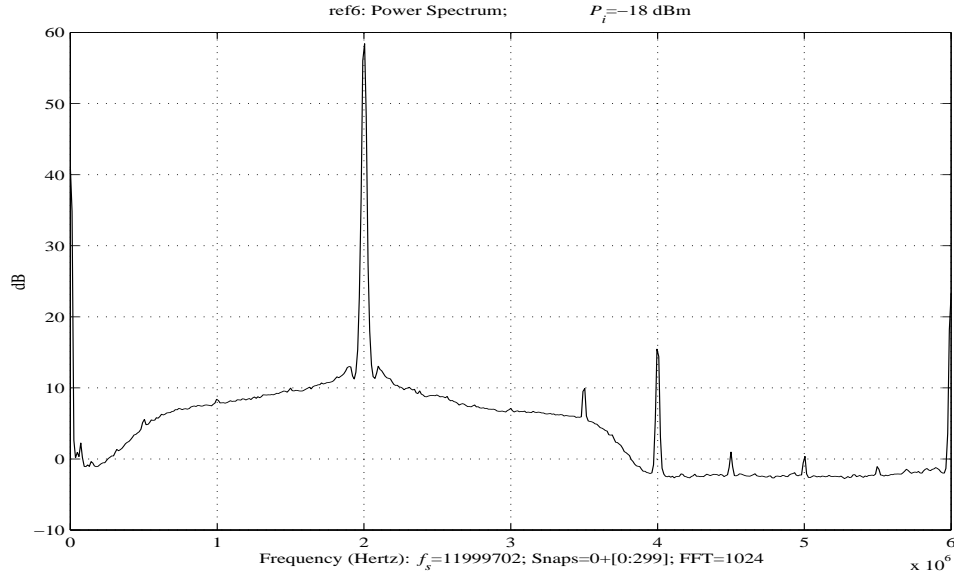


Figure 8.7: Power spectral estimate of the CW signal from ref6.snp. Full RF system including the OA/9123 and the TAS4500.

A straight BPSK is recorded in ref4.snp: no additive noise, fading, or loss. Figure 8.8 shows the power spectrum of ref4.snp estimated from the first 300 snapshots. The input power level is $P_i = -14$ dBm giving a nominal SNR of +29 dBm. This relatively wide signal bandwidth permits a similar claim to be

drawn from the spectrum: The noise floor is approximately -30 dB from the signal. Comparison with Figure 8.5 shows that the spectral distortion across the passband has slightly increased. Figure 8.9 shows this corresponding distortion of the raised cosine pulse in the time domain. Comparison with Figure 8.6 shows that the leading sidelobe has slightly increased its power.

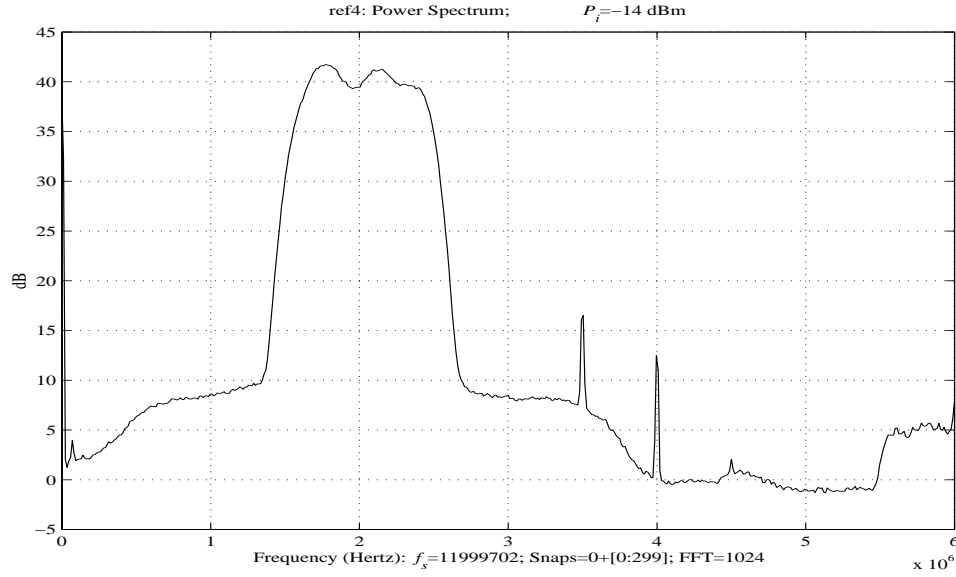


Figure 8.8: Power spectral estimate of the BPSK signal in ref4.snp. Full RF system including the OA/9123 and the TAS4500. No additive noise, fading, or loss.

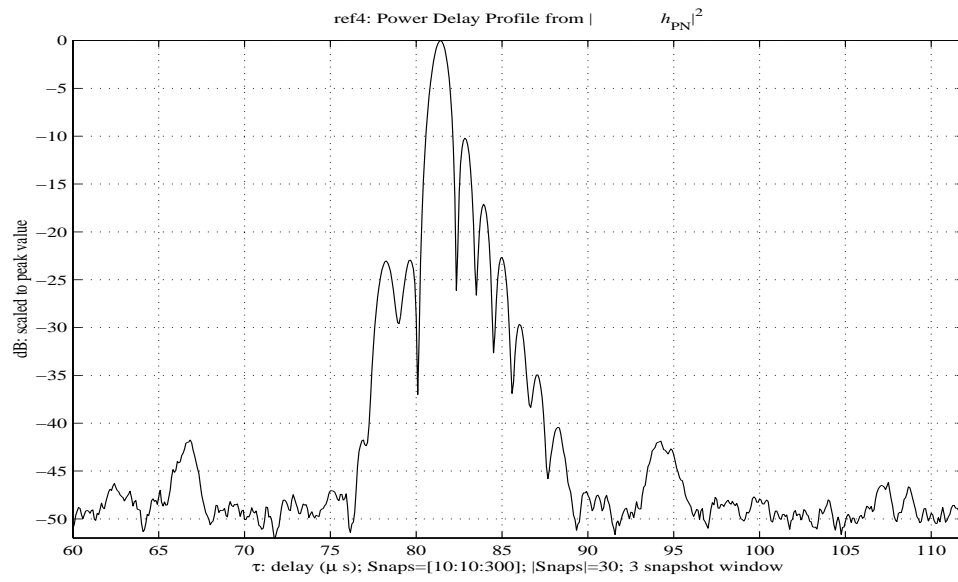


Figure 8.9: PN estimate of the power delay profile for the BPSK ref4.snp. Close-up of the distorted raised cosine filter.

8.4 TAS4500_13: Amplitude Calibration

Section 8.1 established the noise floor without the TAS4500 channel emulator and the OA/9123 coupler in the channel emulation. Section 8.2 added the OA/9123 coupler and showed the distortion of the raised cosine. This section adds the TAS4500 channel emulator to get the full RF multipath channel emulation. Two SNP files establish the noise, time, and resolution. The SNP file tas4500_13.snp has two paths with a relative delay of $100 \mu\text{s}$ and equal amplitude. Figure 8.10 displays the PN estimate. The (circularly shifted) estimated delay is $100 \mu\text{s}$ with the second path amplitude at -0.3291 dB . In concordance with Sections 8.1 and 8.2, the SFDR= -34 dB . Figure 8.11 shows the RFGM estimate. The estimated delay is again $100 \mu\text{s}$ with the second path's amplitude at -0.0078 dB . Figure 8.12 is a close-up for comparison with the AF estimate. Figure 8.13 is the AF estimate where the data has been decimated to accommodate the $100 \mu\text{s}$ relative delay. The noise floor has increased by 10 dB compared to Figure 8.4. All estimators display a leading sidelobe in the first pulse.

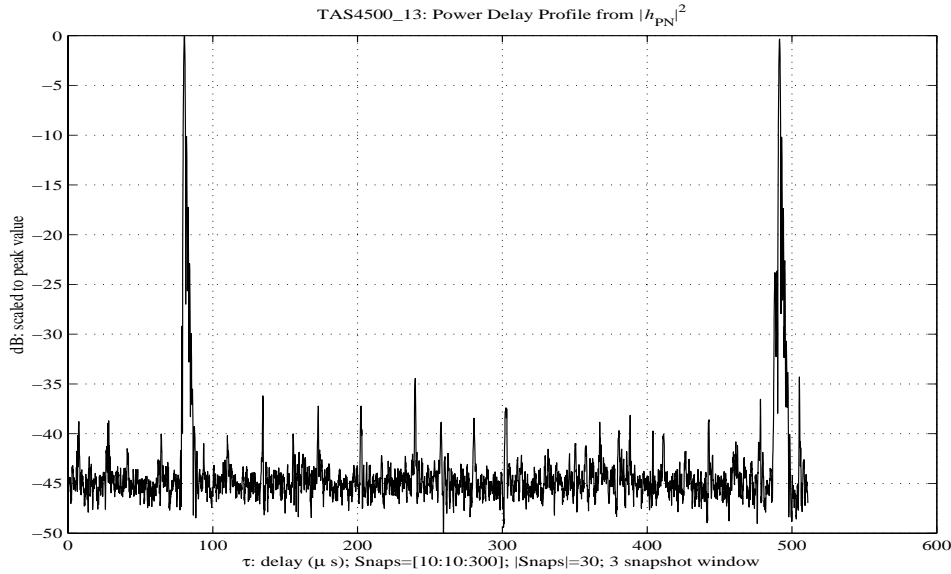


Figure 8.10: PN estimate of the power delay profile for tas4500_13.snp. Emulated delays: $\tau_n = [0 \ 100] \mu\text{s}$. Emulated amplitudes: $a_n = [0 \ 0] \text{ dB}$. Estimated amplitudes: $[0 \ -0.3291] \text{ dB}$.

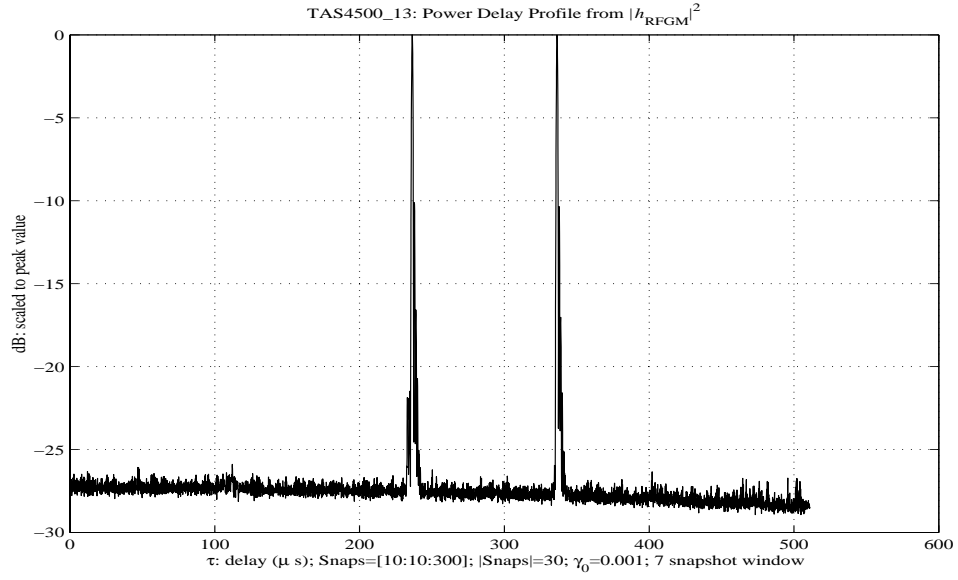


Figure 8.11: RFGM estimate of the power delay profile for tas4500_13.snp. Emulated delays: $\tau_n=[0 \ 100] \ \mu\text{s}$. Emulated amplitudes: $a_n=[0 \ 0] \ \text{dB}$. Estimated amplitudes: $[0 \ -0.0078] \ \text{dB}$.

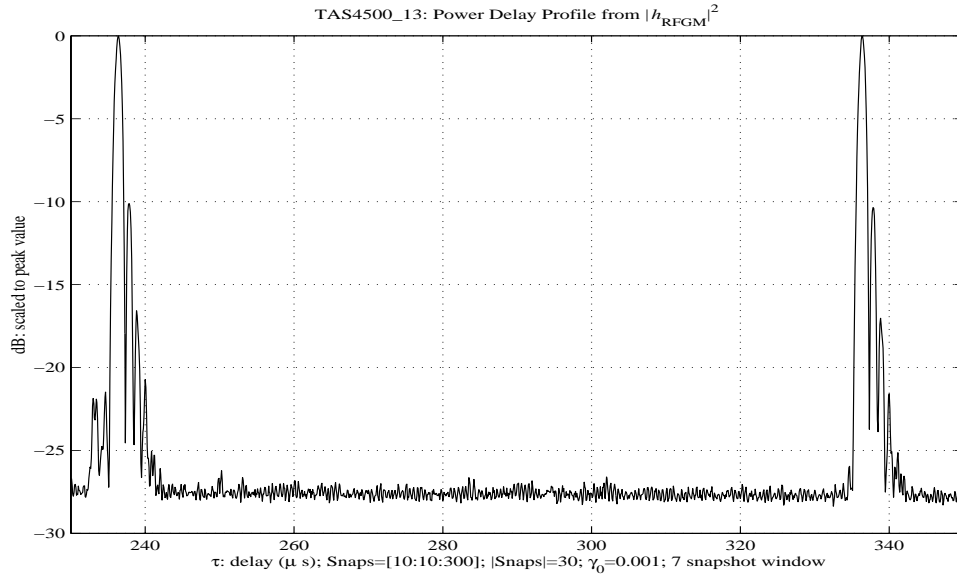


Figure 8.12: Close-up of the RFGM estimate of the power delay profile for tas4500_13.snp

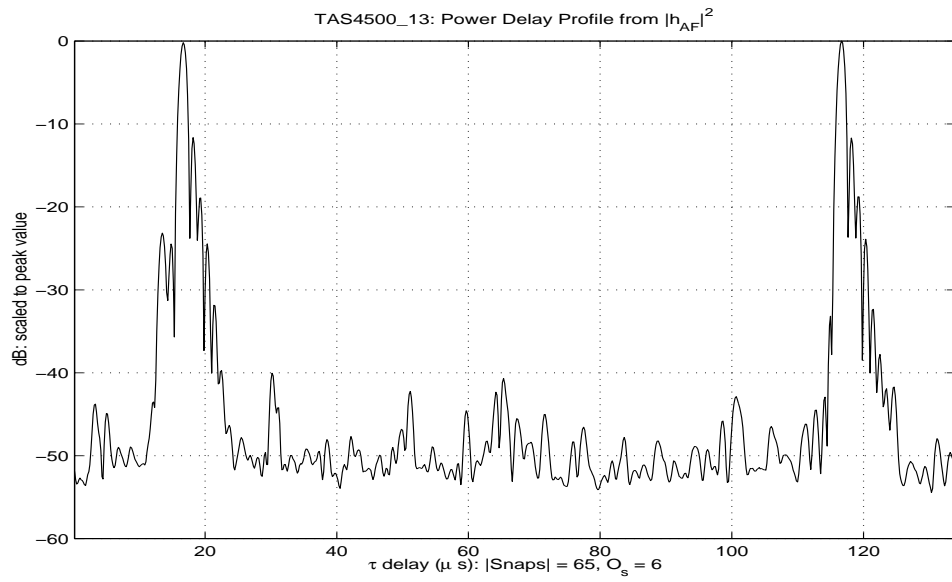


Figure 8.13: Close-up of AF estimate of the power delay profile for tas4500_13.snp. Emulated delays: $\tau_n=[0\ 100]\ \mu s$. Emulated amplitudes: $a_n=[0\ 0]\ \text{dB}$. Estimated amplitudes: $[-0.17\ 0]\ \text{dB}$.

8.5 TAS4500_11: Amplitude Calibration

Section 8.4 showed h_{PN} , h_{RFGM} , and h_{AF} obtained excellent estimates of the channel characteristics. These results differ when `tas4500_11.snp` file is considered. In this file, three paths of equal amplitude are emulated. The delays of Path 2 and 3 are 5 and 10 μs so they are well-separated to assess the time resolution. Figure 8.14 displays the PN estimate. In contrast to the SFDR of -30 dB obtained from Sections 8.1, 8.2, and 8.4, the SFDR has been reduced. Figure 8.15 presents a close-up of the paths. The delays are at the proper times but errors are in the amplitudes. Similar amplitude errors are present in the RFGM estimate shown in Figures 8.16 and 8.17.

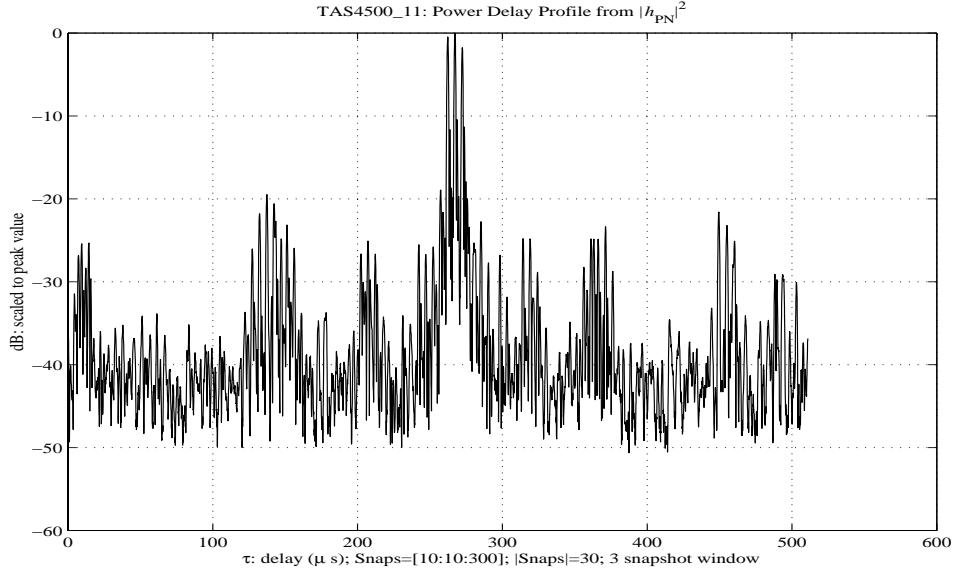


Figure 8.14: PN estimate of the power delay profile for `tas4500_11.snp`.

In contrast, the AF estimate shown in Figure 8.18 has a noise floor of -50 dB with maximum amplitude error of -0.17 dB. Yet in Section 8.4, we saw all three estimators in close agreement. *Why should h_{PN} and h_{RFGM} fail in this case?* The reason lies in the demodulation scheme and is explored in the next section.

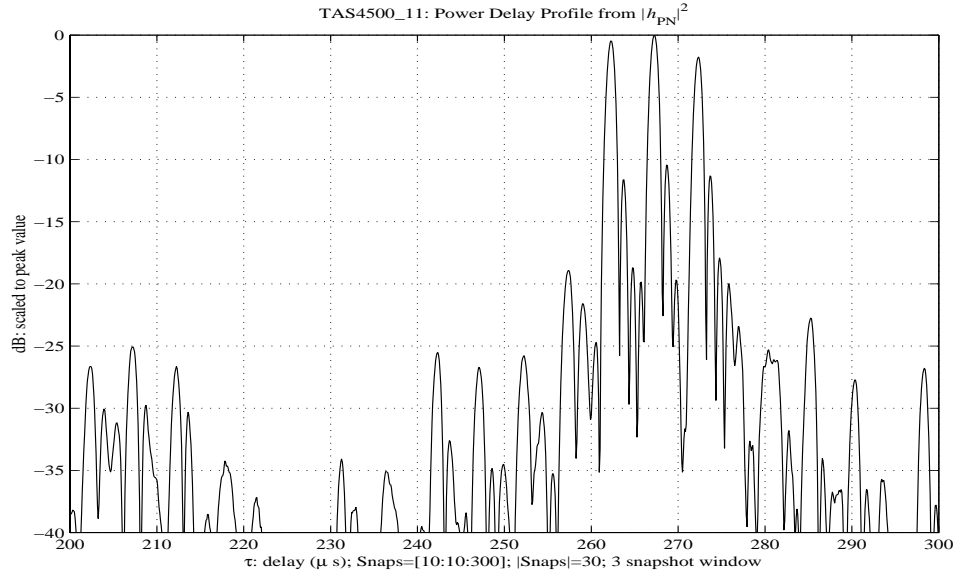


Figure 8.15: Close-up of PN estimate of the power delay profile for tas4500_11.snp. Emulated delays: $\tau_n=[0 \ 5 \ 10] \mu s$. Emulated amplitudes: $a_n=[0 \ 0 \ 0] \text{ dB}$. Estimated amplitudes: $[-0.47 \ 0 \ -1.77] \text{ dB}$.

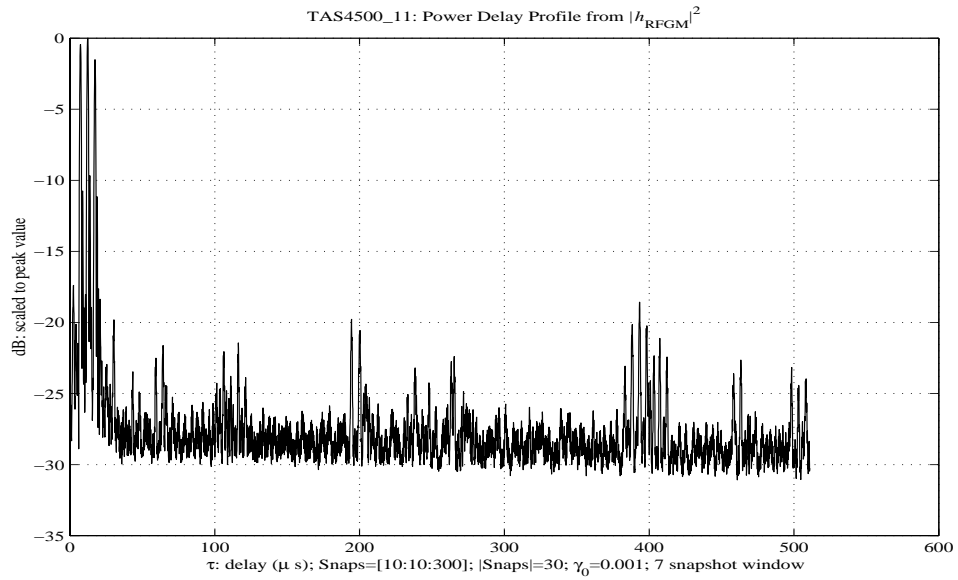


Figure 8.16: RFGM estimate of the power delay profile for tas4500_11.snp.

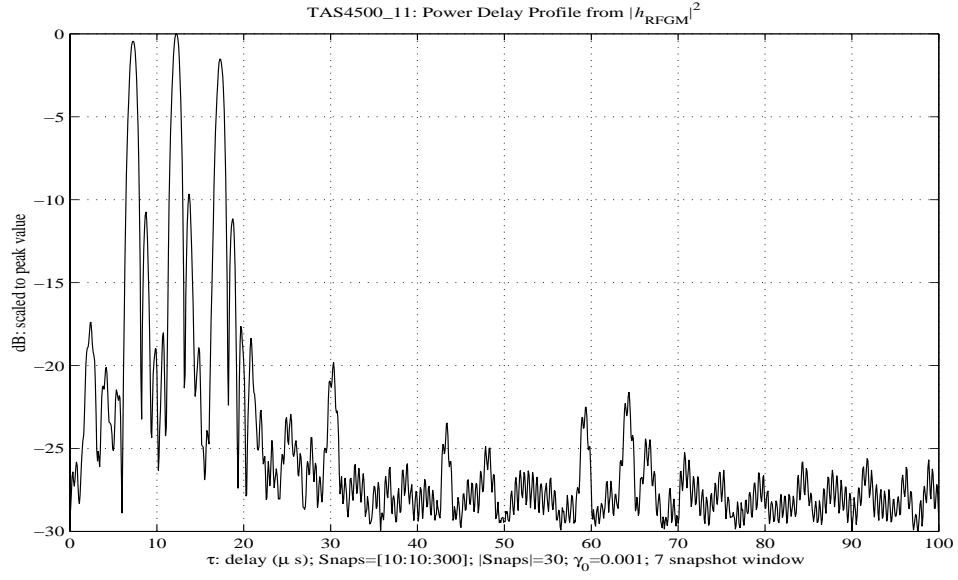


Figure 8.17: Close-up of RFGM estimate of the power delay profile for tas4500_11.snp. Emulated Delays: $\tau_n=[0 \ 5 \ 10] \ \mu\text{s}$. Emulated Amplitudes: $a_n=[0 \ 0 \ 0] \ \text{dB}$. Estimated amplitudes: $[-0.34 \ 0 \ -1.5] \ \text{dB}$.

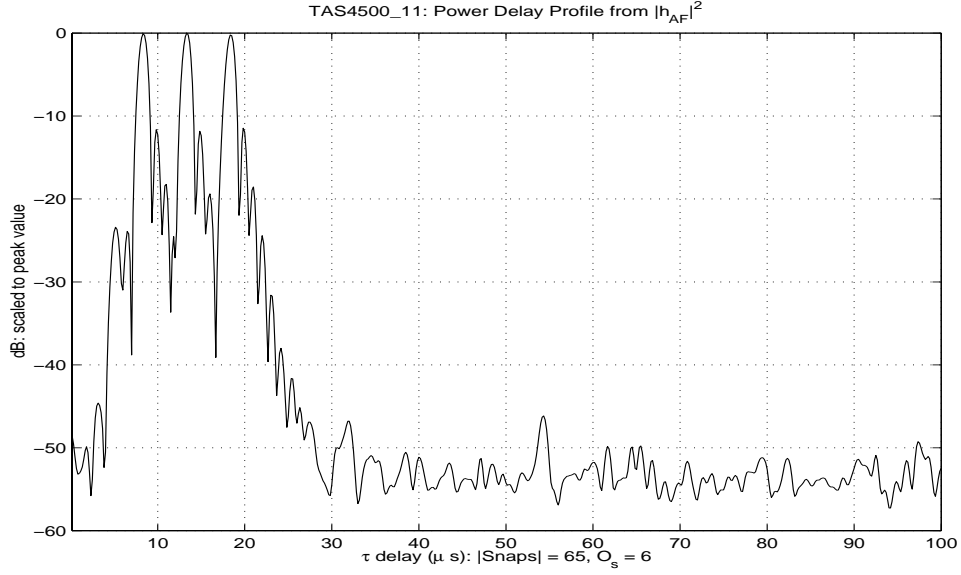


Figure 8.18: AF estimate of the power delay profile for tas4500_11.snp. Emulated Delays: $\tau_n=[0 \ 5 \ 10] \ \mu\text{s}$. Emulated Amplitudes: $a_n=[0 \ 0 \ 0] \ \text{dB}$. Estimated amplitudes: $[-0.079 \ 0 \ -0.17] \ \text{dB}$.

8.6 TAS4500_18: Amplitude Calibration

Section 8.4 showed h_{PN} , h_{RFGM} , and h_{AF} in close agreement on the estimated amplitudes for tas4500_13.snp. However, Section 8.5 showed that only h_{AF} registered the amplitudes for tas4500_11.snp. The reason is that the demodulation scheme for h_{PN} and h_{RFGM} works best when only a single dominant path is present. Multiple paths of nearly equal amplitudes may or may not be demodulated properly.

The demodulation for h_{PN} and h_{RFGM} requires the filtered phase extracted from y_{RF}^2 (See Section 8.1). So we start by considering the power spectrum of y_{RF}^2 . Figure 8.19 shows the carrier of y_{RF}^2 for tas4500_13.snp. Even though this file contains two paths of equal amplitude, the carrier at 4 MHz clearly registers in the power spectrum. Correct demodulation is possible and all estimators obtained close agreement on the amplitudes (See Section 8.4). In contrast, Figure 8.20 shows the power spectrum of y_{RF}^2 for tas4500_11.snp. The 4 MHz carrier barely exceeds the noise level. Demodulation using this approach is corrupted by the phase errors. Consequently, h_{PN} and h_{RFGM} were corrupted (See Section 8.5).

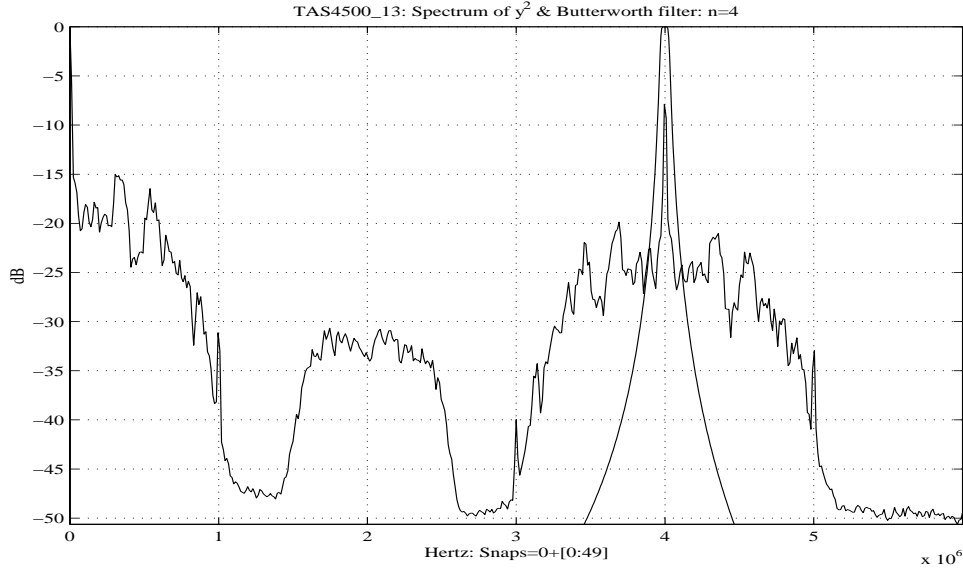


Figure 8.19: Power spectrum estimate of y_{RF}^2 from tas4500_13.snp with demodulation filter.

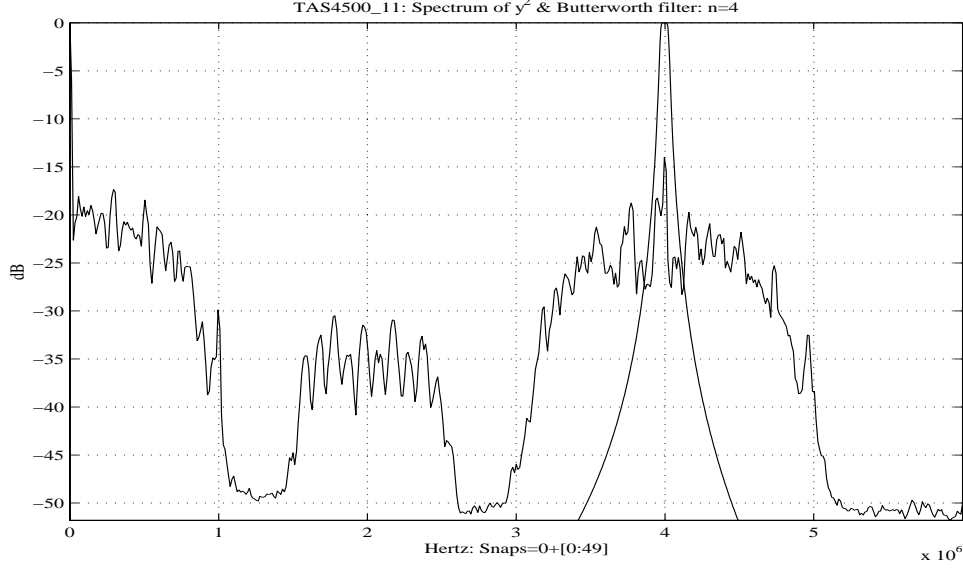


Figure 8.20: Power spectrum estimate of y_{RF}^2 from tas4500_11.snp with demodulation filter.

To back this demodulation assertion, consider tas4500_18.snp. This time-invariant emulation has three paths with relative delays of 0, 20, and 40 μs and losses of 0, 20, and 30 dB, respectively. This emulation also tests how well different amplitudes are resolved. Figure 8.21 shows the power spectrum of y_{RF}^2 . The 4 MHz carrier is clear. Figure 8.22 shows h_{PN} cleanly registers the amplitudes. However, h_{RFGM} in Figure 8.23 barely displays the 30 dB path and obtains a poor estimate for the 20 dB path. As expected, Figure 8.24 shows that h_{AF} precisely registers the amplitudes.

In contrast to the “blind” approach of carrier phase retrieval, the AF estimator incorporates the known transmitted bit sequence in the carrier recovery as shown in Figure 6.3. The phase is adjusted on-the-fly at each sample instant using the portion of the bit sequence currently spanned by the adaptive filter. This method is generally more robust than the block approach used in the PN and RFGM estimators, and is analogous to decision-directed phase estimation used in adaptive equalization [63, pages 347–350]

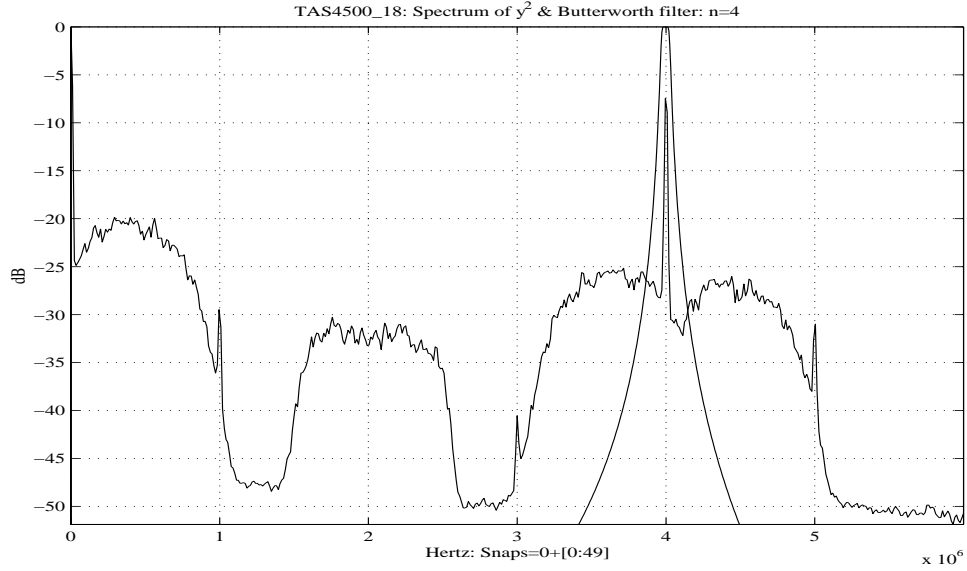


Figure 8.21: Power spectrum estimate of y_{RF}^2 from tas4500_18.snp with de-modulation filter.

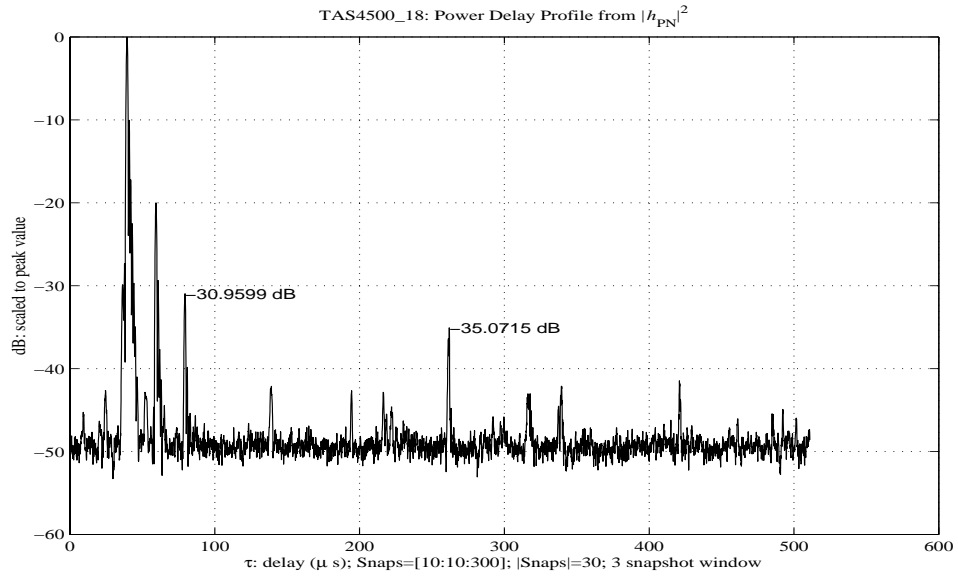


Figure 8.22: PN estimate of the power delay profile for tas4500_18.snp. Emulated Delays: $\tau_n=[0 \ 20 \ 40] \mu\text{s}$. Emulated Amplitudes: $a_n=[0 \ 20 \ 30] \text{ dB}$.

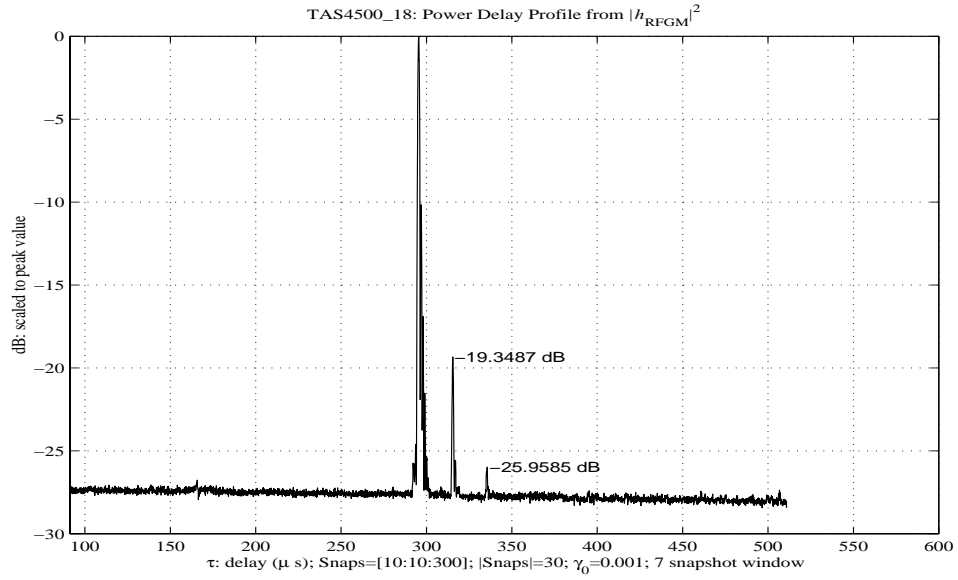


Figure 8.23: RFGM estimate of the power delay profile for tas4500_18.snp. Emulated Delays: $\tau_n=[0 \ 20 \ 40] \mu\text{s}$. Emulated Amplitudes: $a_n=[0 \ 20 \ 30] \text{ dB}$.

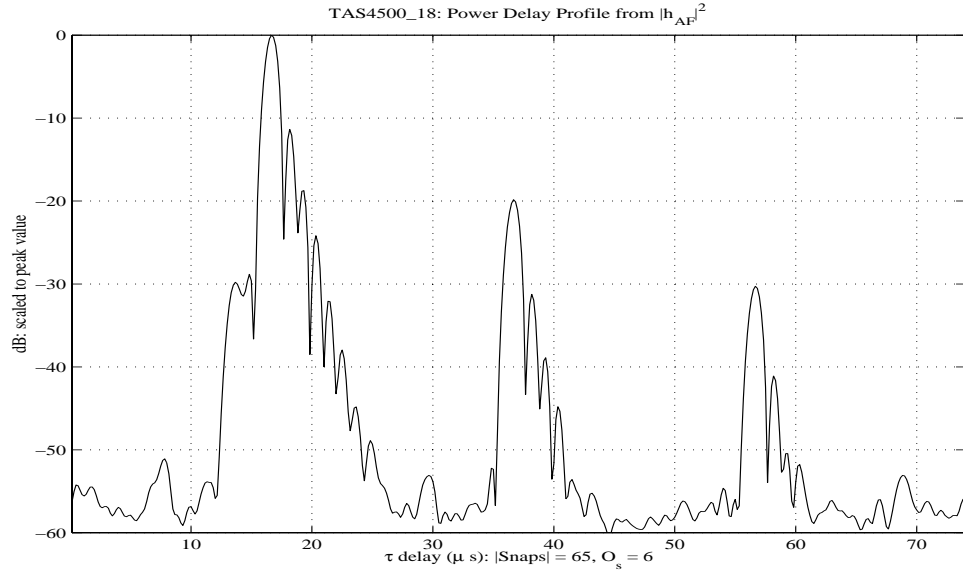


Figure 8.24: AF estimate of the power delay profile for tas4500_18.snp. Emulated Delays: $\tau_n=[0 \ 20 \ 40] \mu\text{s}$. Emulated Amplitudes: $a_n=[0 \ 20 \ 30] \text{ dB}$. Estimated amplitudes: $[0 \ -19.82 \ -30.22] \text{ dB}$.

8.7 TAS4500_19: Time-Variant Channel

This section records the performance of the channel estimators in a slow time-varying channel. The SNP tas4500_19.snp is a 5.6-second dataset containing three Rayleigh fading paths: relative delays are $\tau_n=[0 \ 20 \ 40] \ \mu\text{s}$; relative powers are $a_n=[0 \ -5 \ -10] \ \text{dB}$; fade rates are all 1 Hertz. Figure 8.25 shows the h_{AF} estimate of the power delay profile averaged over the entire dataset. Excellent estimation of the amplitudes is obtained in noise with a SFDR of approximately -40 dB. The distorted raised cosine pulse agrees with the laboratory estimate (Figure 8.6).

Figure 8.26 shows the estimated delay-spread function. The fading on each of the paths is evident as well as the relative amplitudes. Estimated fade rates are obtained directly from level-crossing estimates of the tap amplitudes (Fix τ_n and count level-crossings of $|h_{\text{AF}}(t, \tau_n)|$ [61, pages 125–129]). More detail is revealed by the scattering function in Figure 8.27. The bandwidth agrees with the expected shape. However, the peaks are shifted by 5 Hertz. This may be due to the 5 bps error (Chapter 7) in the FIREBERD-4000.

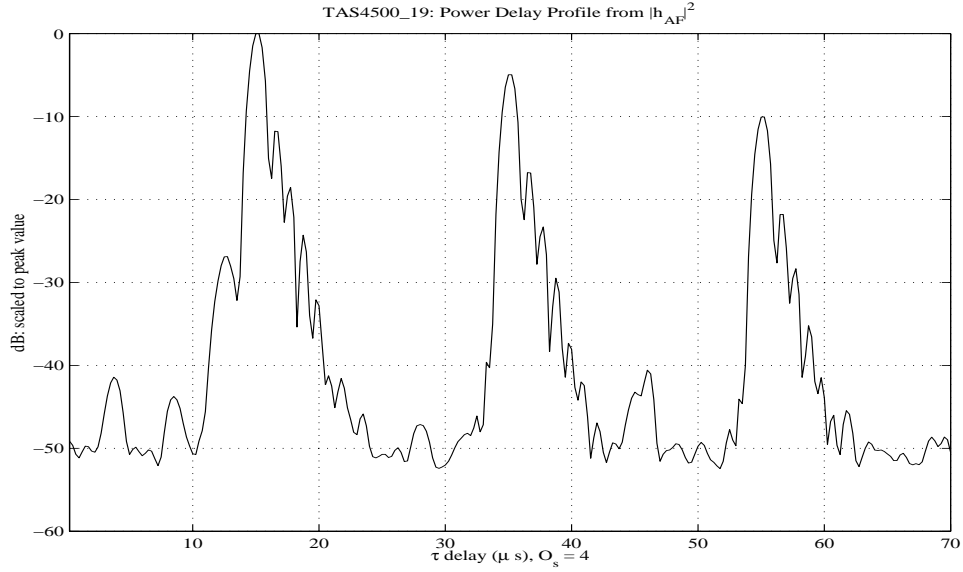


Figure 8.25: AF estimate of the power delay profile for tas4500_19.snp. Emulated Delays: $\tau_n=[0 \ 20 \ 40] \ \mu\text{s}$. Emulated Amplitudes: $a_n=[0 \ -5 \ -10] \ \text{dB}$. Estimated Amplitudes: $[0 \ -4.96 \ -10.06] \ \text{dB}$.

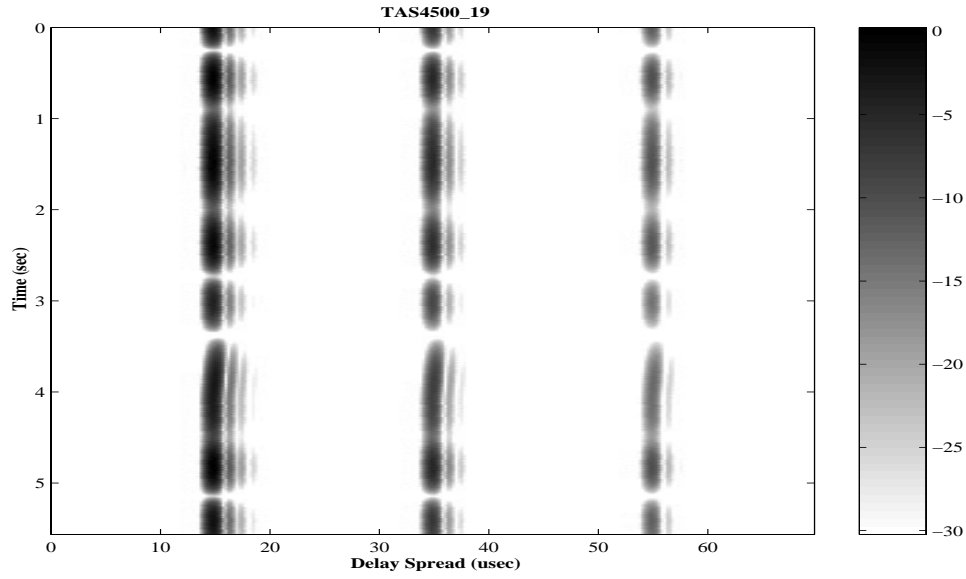


Figure 8.26: AF estimate of the delay-spread function for tas4500_19.snp. Emulated Delays: $\tau_n=[0 \ 20 \ 40] \ \mu s$. Emulated Amplitudes: $a_n=[0 \ -5 \ -10] \ \text{dB}$. Emulated Fade Rates: $f_n=[1 \ 1 \ 1] \ \text{Hz}$. Estimated Fade Rates: $f_n=[1.98 \ 1.80 \ 2.15] \ \text{Hz}$.

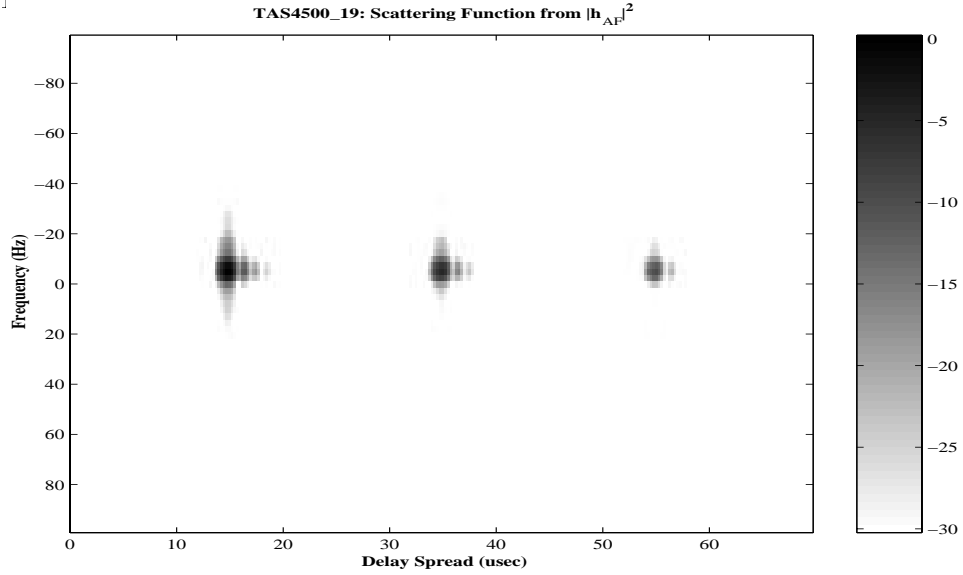


Figure 8.27: AF estimate of the scattering function for tas4500_19.snp. Emulated Delays: $\tau_n=[0 \ 20 \ 40] \ \mu s$. Emulated Amplitudes: $a_n=[0 \ -5 \ -10] \ \text{dB}$. Emulated Fade Rates: $f_n=[1 \ 1 \ 1] \ \text{Hz}$.

8.8 TAS4500_24: Time-Variant Channel

This section records the performance of the channel estimators for another time-varying channel. The SNP `tas4500_24.snp` also is a 5.6-second dataset containing three Rayleigh fading paths: relative delays are $\tau_n=[0 \ 20 \ 40] \mu\text{s}$; powers are all equal; fade rates are $f_n=[10 \ 20 \ 40]$ Hertz. Figure 8.28 shows the h_{AF} estimate of the power delay profile averaged over the entire dataset. As in Section 8.7, excellent registration of the amplitudes is observed.

Figure 8.29 shows the estimated delay-spread function. The different fade rates register on each path as well as the relative amplitudes. The larger fade rates permit a more accurate level-crossing estimate in comparison to Section 8.7. The increased bandwidths are seen in the estimated scattering function of Figure 8.30.

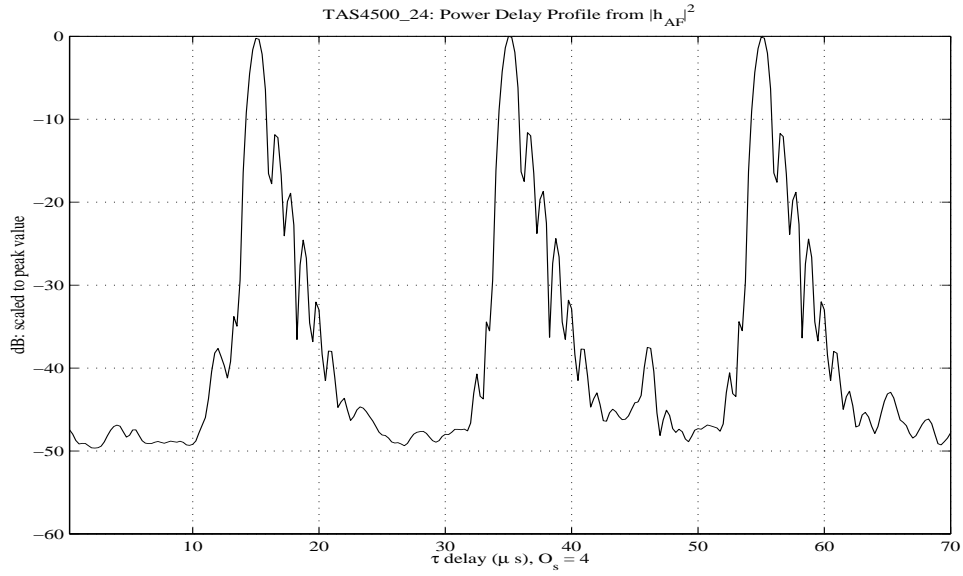


Figure 8.28: AF estimate of the power delay profile for `tas4500_24.snp`. Emulated Delays: $\tau_n=[0 \ 20 \ 40] \mu\text{s}$; Emulated Amplitudes: $a_n=[0 \ 0 \ 0] \text{ dB}$; Estimated amplitudes: $[-0.24 \ 0 \ -0.10] \text{ dB}$.

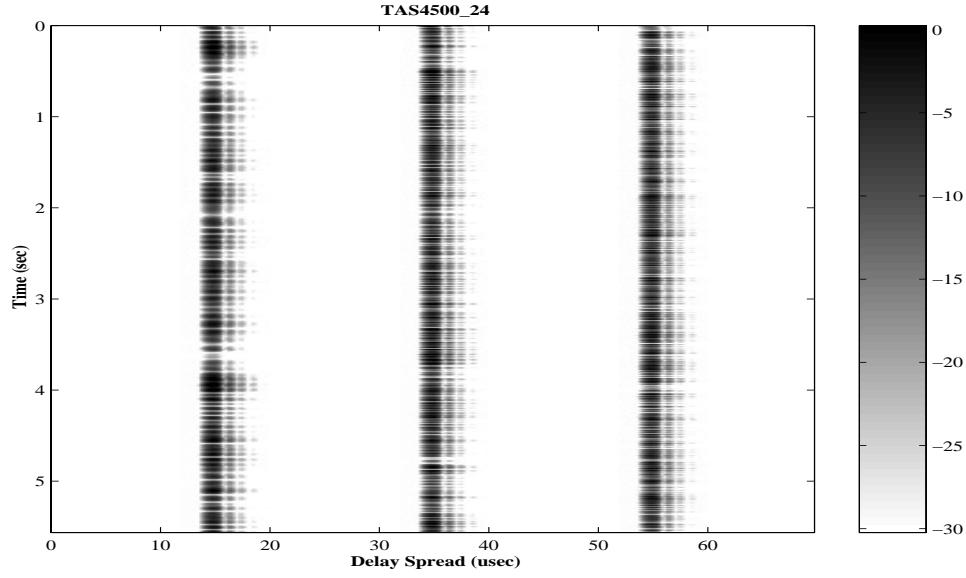


Figure 8.29: AF estimate of the delay-spread function for tas4500_24.snp. Emulated Delays: $\tau_n=[0 \ 20 \ 40] \ \mu s$. Emulated Fade Rates: $f_n=[10 \ 20 \ 40] \text{ Hz}$. Estimated Fade Rates: $f_n=[10.80 \ 21.55 \ 40.59] \text{ Hz}$.

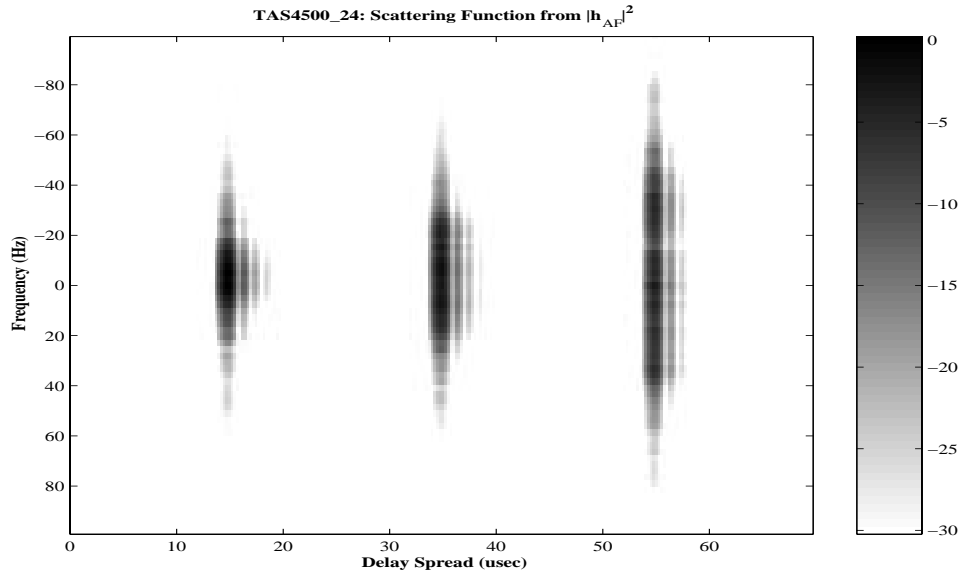


Figure 8.30: AF estimate of the scattering function for tas4500_24.snp. Emulated Delays: $\tau_n=[0 \ 20 \ 40] \ \mu s$. Emulated Amplitudes: $a_n=[0 \ 0 \ 0] \text{ dB}$. Emulated Fade Rates: $f_n=[10 \ 20 \ 40] \text{ Hz}$.

8.9 HMMWV

Section 7.2 describes the HMMWV data. The SNP file `hmmwv1325.snp` was collected on January 16, 1998 at 13:25 while the HMMWV was driving south on I-5 near the San Diego airport at approximately 55 mph. Figures 8.31 and 8.32 plot the estimated power delay profiles obtained from h_{AF} and h_{PN} . Section 8.6 shows h_{AF} resolves paths down to the -30 dB level with a SFDR=-40 dB. Likewise, h_{PN} resolves paths down to the -35 dB level with a SFDR=-35 dB. Both plots are in close agreement. They show a main lobe wider than that of the lab or ship data (Figure 8.35), and both register a secondary path at 17 μ s relative delay. Thus, this HMMWV channel is dispersive.

The delay-spread function reveals further details. Figure 8.33 plots the estimated delay-spread function. We see that the main path exhibits deep fades. Although the secondary path is at the -20 dB level in the PDP, this path contributes to the channel during deep fades of the main path. The scattering function gives insight regarding the modulations on these paths. Figure 8.34 plots the estimated scattering function. We see the secondary path is shifted by 10 Hertz. Moreover, the scattering function reveals several paths trailing the main path. Comparison with the power delay profile and the delay-spread function show that these paths contribute to the extra “width” of the main lobe. In contrast to the simple two-path model for the ship (Section 8.10), a multiple-path model is required to capture the features of this channel.

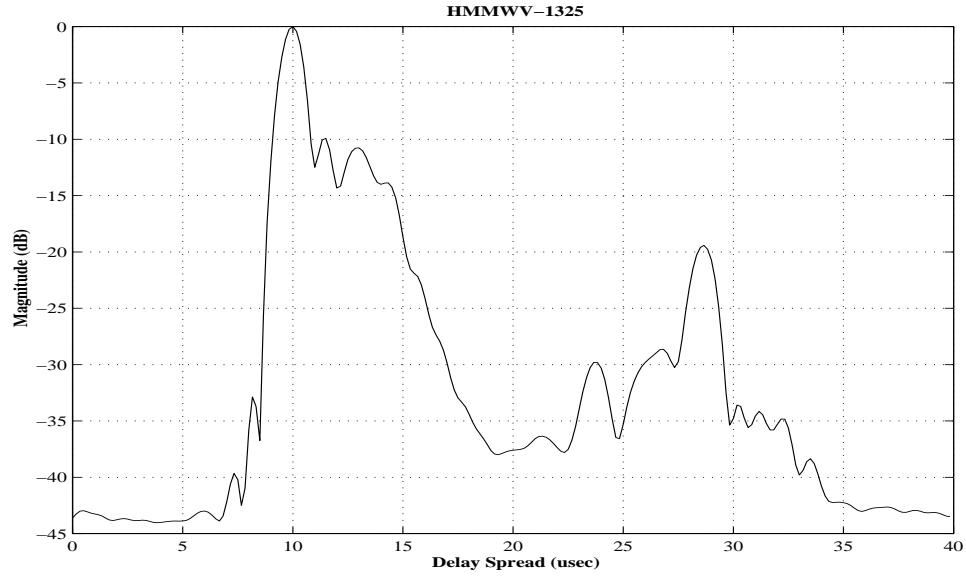


Figure 8.31: AF estimate of the power delay profile for hmmwv1325.snp.

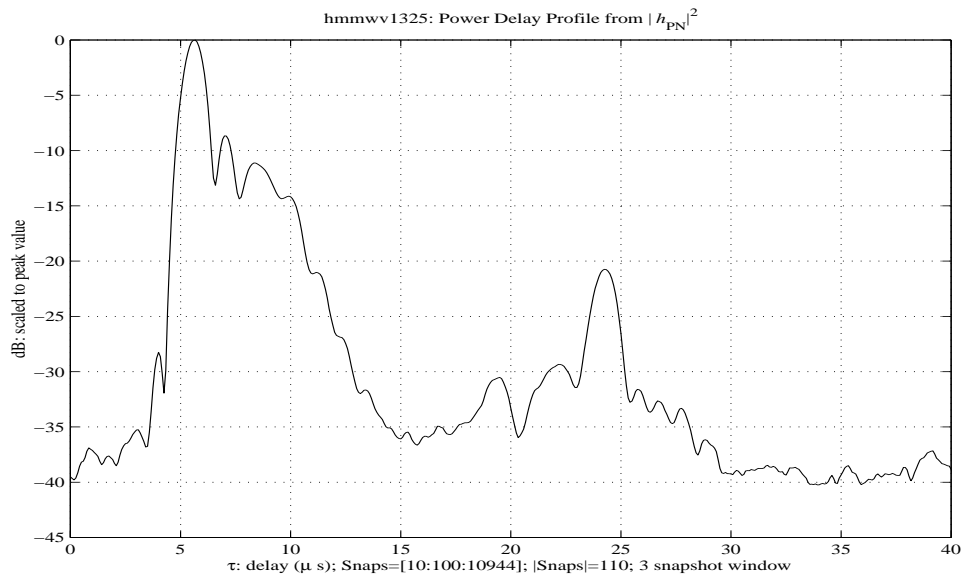


Figure 8.32: PN estimate of the power delay profile for hmmwv1325.snp.

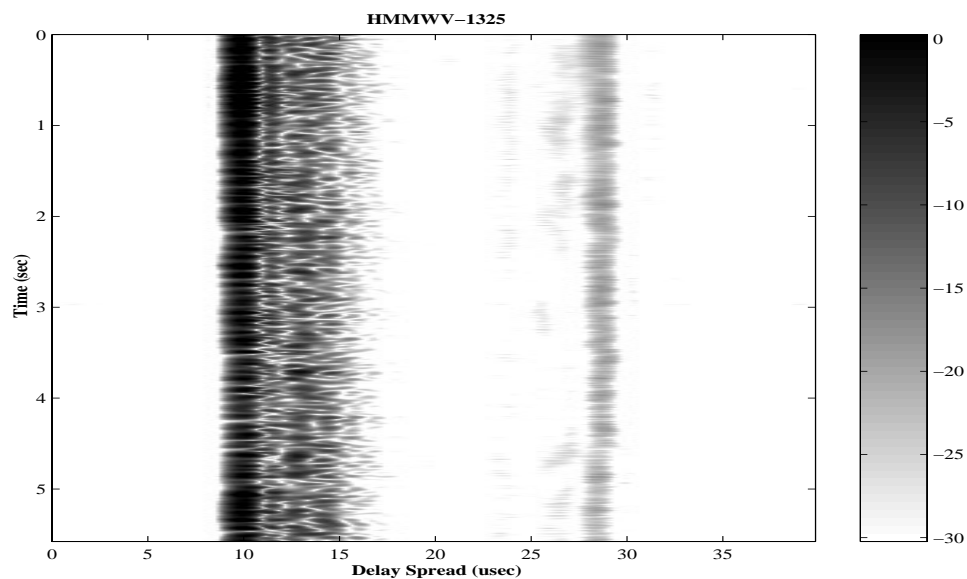


Figure 8.33: AF estimate of the delay-spread function for hmmwv1325.snp.

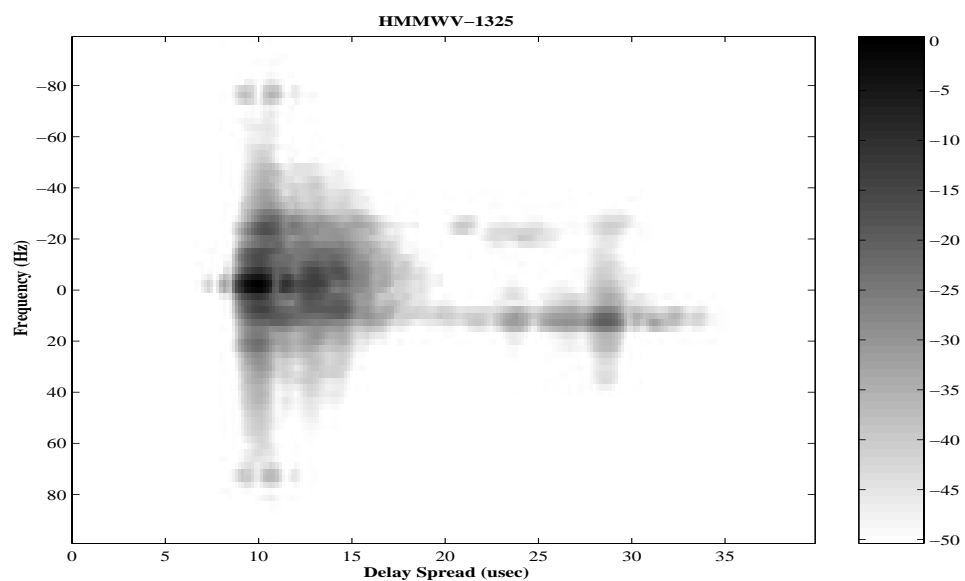


Figure 8.34: AF estimate of the scattering function for hmmwv1325.snp.

8.10 Ship-to-Shore

Section 7.3 describes the channel data collected from the USS Princeton. The SNP file ship12jan1459.snp was collected on January 12, 1998 at 14:59 while the USS Princeton was heading west under the Coronado bridge while steaming at approximately 10 to 15 knots. Figure 8.35 is the estimated power delay profile obtained from h_{AF} . The relevant question is: *How far down is the AF registering the channel?* Figure 8.13 showed that the SFDR for h_{AF} is at least -40 dB from the signal. More importantly, h_{AF} properly registers amplitudes at the -30 dB level (See Figure 8.24). Thus, Figure 8.35 is likely good to at least -30 dB and probably down to -40 dB.

Comparison of this ship's estimated power delay profile with the laboratory estimate (Figure 8.6) shows significant differences: the leading sidelobes are decreased; the first trailing sidelobe has increased; the trailing sidelobes have longer duration. Also, the delay spread σ_τ is approximately 27% larger (See Table 2.1). This is also validated by the PN estimate of this data (See Figure 8.36). From this larger view of the channel, the SFDR for h_{PN} is 32 dB. Both estimators are in close agreement above -30 dB. Thus, we conclude that channel dispersion is present. We turn to the delay-spread estimate to give more details of this channel.

Figure 8.37 is the estimated delay spread function for ship12Jan1459.snp. The first band of energy at 10 μ s delay has constant magnitude so is likely a specular path. The band of energy at 12 μ s delay is dynamic with both fast and slow modulation of its energy. Thus, the estimated delay-spread function suggests that two paths are present. The scattering function can further quantify this conjecture. Figure 8.38 presents the estimated scattering function computed over 14 averages. The 10 μ s delay shows spectrum centered at DC whereas the 12 μ s delay's spectrum is shifted by 5 Hertz. These plots suggest that a simple two-path model may capture the general features of this channel.

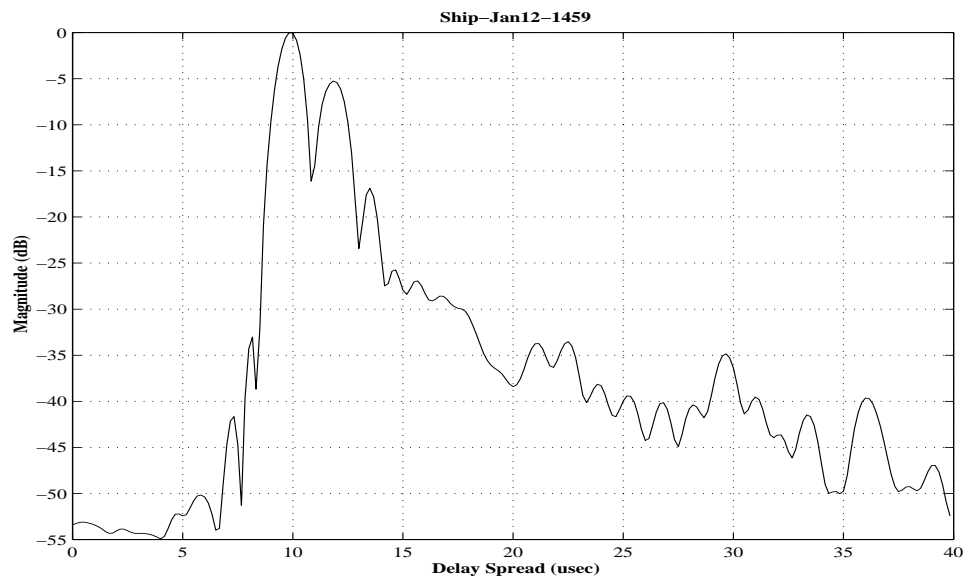


Figure 8.35: AF estimate of the power delay profile for ship12Jan1459.snp.

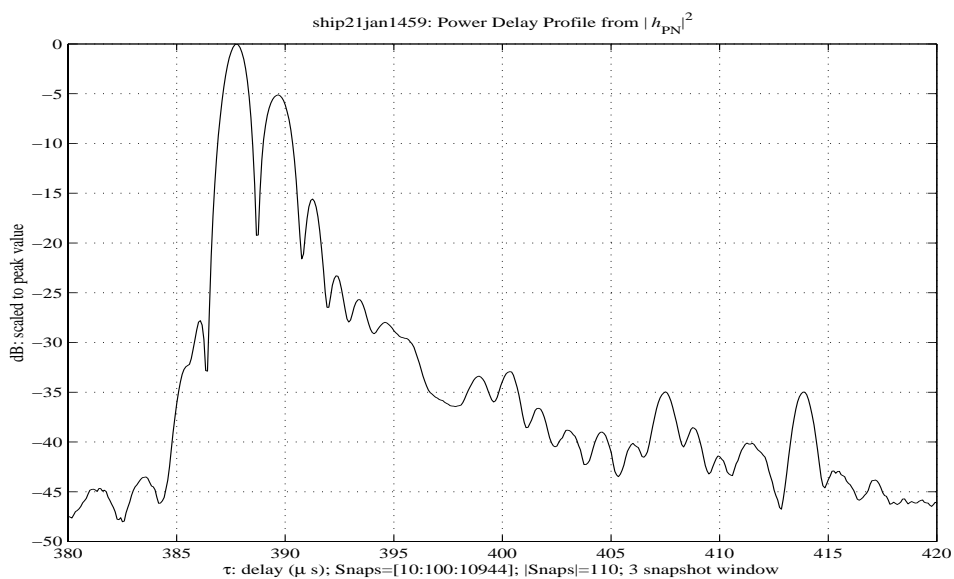


Figure 8.36: PN estimate of the power delay profile for ship12Jan1459.snp.

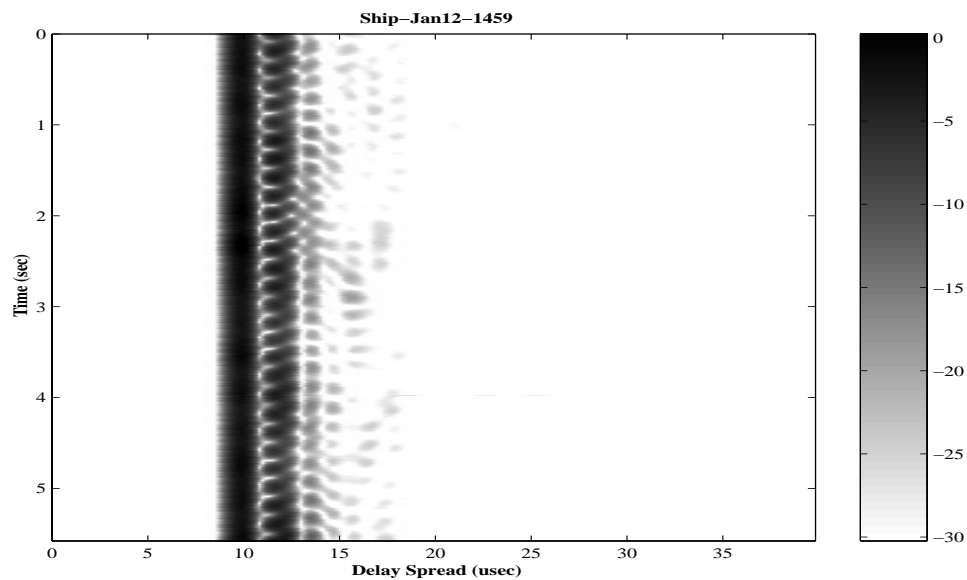


Figure 8.37: AF estimate of the delay-spread function for ship12Jan1459.snp.

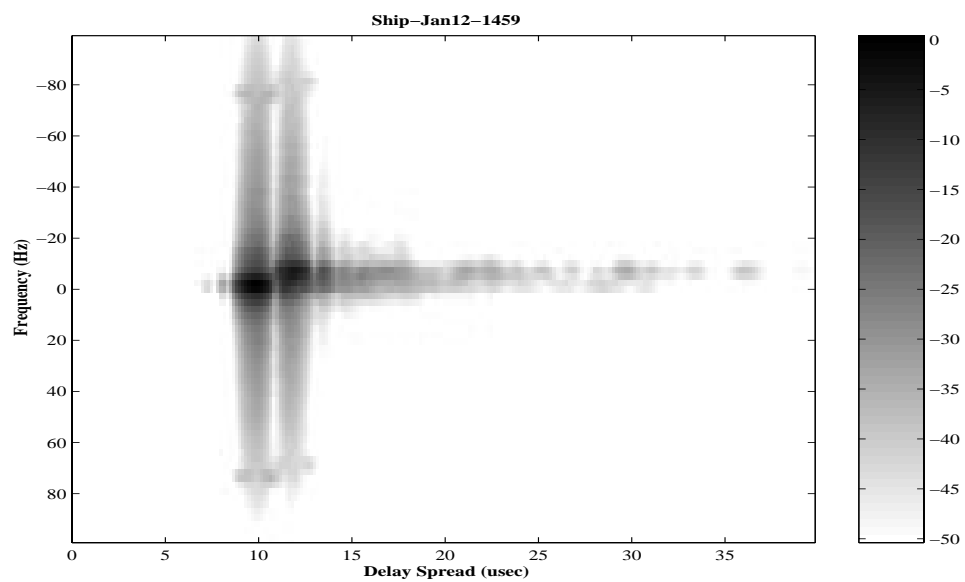


Figure 8.38: AF estimate of the scattering function for ship12Jan1459.snp. Estimated from 14 averages.

Chapter 9

Future Directions

Phase II of this effort should incorporate refinements to the channel estimation algorithms and extensions to the data analysis. These are listed as follows:

Demodulation must be part of a channel estimator: Chapter 8 demonstrated the importance of the demodulator to compensate for multipath fading to allow for accurate channel estimates. Indeed, the PN estimators were seen to be corrupted by errors in the carrier phase recovery. While the system identification channel estimation technique did provide for robust demodulation, it is an order of magnitude more computationally expensive. Most of the results described in this report using this technique were generated on a supercomputer. Thus, it is worthwhile to develop PN estimators that incorporate more robust carrier recovery and symbol timing to multipath fading.

Robustness must be part a channel estimator: Chapter 8 demonstrated that the raised cosine could be distorted. Likewise, the experiments were carefully designed to operate in the linear region of the amplifiers. Thus, it is not an academic question to ask: What is the effect of these distortions on a channel estimator? More generally, estimators must be developed that are robust with respect to model variations.

Statistical issues of the channel functions: Estimating the distribution and the temporal correlations of the Delay Spread function taps are valuable for characterizing RF propagation channels of interest to the Navy. For example,

these distributions and fade rates should be incorporated into realistic propagation simulations to assess military radio performance. This information is also vital for the initial design of radios. For example, channel dispersion is used to determine equalizer length, while fade rates are used to determine interleaver depth for channel codes and update rates in the adaptive equalizers.

Removing the raised channel functions: Chapter 2 showed that the channel estimators can only approximate the digital channel functions. These digital channel functions contain the channel function “smeared” by the raised cosine filter. For example, the digital baseband Input Delay-Spread function $h_B(m, k)$ is the convolution of the Input Delay-Spread function $h(t, \tau)$ along the lag τ with the raised cosine: $h_B(m, k) = h *_{\tau} x_{RC}(m\tilde{T}, k\tilde{T})$. This effect is graphically displayed in both the emulated and over-the-air channel soundings of Chapter 8. Thus, it is worthwhile to ask how cleanly the raised cosine filter can be deconvolved to reveal the underlying channel. Progress on this question is promising and forms a major area for Phase II.

Acquire air-to-ground RF channel data: An important extension to the RF channel data is an air-to-ground link. For example, UAVs extend the range of UHF radios beyond the horizon. This data will assist in measuring the performance of military radios in such an operation.

Propagation modeling: The propagation models of Chapter 4 may be coupled with the measured data to obtain realistic estimates of received power. This is used to determine transmit power levels that ensure adequate receiver performance and efficient use of the frequency spectrum in a cellular environment.

Bibliography

- [1] Beard, C. I. [1961] Coherent and Incoherent Scattering of Microwaves from the Ocean, *IRE Transactions on Antennas and Propagation*, Volume AP-9, pages 470–483.
- [2] Beard, C. I., I. Katz, L. M. Spetner [1956] Phenomenological Vector Model of Microwave Reflection from the Ocean, *IRE Transactions on Antennas and Propagation*, Volume AP-4, pages 162–167.
- [3] Bello, Philip A. [1963] Characterization of Randomly Time-Variant Linear Channels, *IEEE Transactions on Communications Systems*, Vol. CS-11, pages 360–393. Reprinted in [30].
- [4] Bello, Philip A. [1965] Some Techniques for the Instantaneous Real-Time Measurement of Multipath and Doppler Spread *IEEE Transactions on Communication Technology*, Vol. COM-13, pages 285–292. Reprinted in [30].
- [5] Bello, Philip A. [1969] A Troposcatter Channel Model, *IEEE Transactions on Communication Technology*, Vol. COM-17, pages 130–137. Reprinted in [30].
- [6] Bello, Phillip A. [1973] Aeronautical Channel Characterization, *IEEE Transaction on Communications*, Volume COM-21, pages 548–563. Reprinted in [30] and *Data Communications via Fading Channels*, edited by Kenneth Brayer, IEEE Press, New York, 1975.
- [7] Bensley, S.E.; Aazhang, B. [1996] Subspace-based channel estimation for code division multiple access communication systems, *IEEE Transactions on Communications*, vol.44, no.8 p.1009-20.

- [8] Biglieri, Ezio & Valerio Zingarelli [1994] Coded Modulation for Channels Affected by Noise, Correlated Rice Fading, and Doppler Frequency Shift, *IEEE International Conference on Communications ICC '94*, New Orleans, Louisiana, USA, pages 18–22.
- [9] Boithias, Lucien [1987] *Radio Wave Propagation*, McGraw-Hill Book Company, New York.
- [10] Brayer, Kenneth (editor) [1975] *Data Communications via Fading Channels*, IEEE Press, New York.
- [11] Brockwell, Peter J. & Richard A. Davis [1987] *Time Series: Theory and Methods*, Springer-Verlag, New York.
- [12] Bullington, Kenneth [1956] Radio Propagation Fundamentals, *Bell System Technical Journal*, Volume 36. Reprinted in *Data Communications via Fading Channels*, edited by Kenneth Brayer, IEEE Press, New York, 1975.
- [13] Cavers, James K. & Jaria Liao [1992] A Comparison of Pilot Tone and Pilot Symbol Techniques for Digital Mobile Communications, *Globe-com'92*, pages 915–921, Volume 2.
- [14] Crohn, Ilan & Ernst Bonek [1992] Modeling of Intersymbol-Interference in a Rayleigh Fast Fading Channel with Typical Delay Power Profiles, *IEEE Transactions on Vehicular Technology*, Volume 41, Number 4, pages 438–446.
- [15] Chu, David C. [1972] Polyphase Codes with Good Periodic Correlation Properties, *IEEE Transactions on Information Theory*, pages 531–532.
- [16] Cupo, R. L. & R. D. Gitlin [1989] Adaptive carrier recovery systems for digital data communications receivers, *IEEE Journal on Selected Areas in Communications*, Volume 7, Number 9, pages 1328–1339.
- [17] D'Andrea, A. N., A. Diglio, U. Mengali [1994] Symbol-Aided Channel Estimation With Nonselective Rayleigh Fading Channels, *IEEE International Conference on Communications ICC '94*, Volume 1, pages 316–320.

- [18] Davis, Linda M.; Iain B. Collings; Robin J. Evans [1997] Identification of Time-Varying Linear Channels, *ICCASP'97*.
- [19] Falconer, D. D. [1976] Jointly adaptive equalization and carrier recovery in two-dimensional digital communication systems, *Bell System Technical Journal*, Volume 55, Number 3, pages 317–34.
- [20] Fechtel, S.A.; Meyr, H. [1991] An investigation of channel estimation and equalization techniques for moderately rapid fading HF-channels *International Conference on Communications ICC'91*, p.768-72 vol.2
- [21] Felhauer, T. [1993] Digital signal processing for optimum wideband channel estimation in the presence of noise *IEE Proceedings F (Radar and Signal Processing)*, vol.140, no.3 p.179-86.
- [22] Felhauer, T. [1994] A new class of polyphase spreading codes for digital pulse compression radar systems, *Proceedings of IEEE 3rd International Symposium on Spread Spectrum Techniques and Applications (ISSSTA '94)*, Part vol.2 p.396-400 vol.2
- [23] Felhauer, T., P.W. Baier, W. Konig, W. Mohr [1993] Optimized wideband system for unbiased mobile radio channel sounding with periodic spread spectrum signals, *IEICE Transactions on Communications* vol.E76-B, no.8 p.1016-29.
- [24] Fleury, Benard Henri [1995] New Bounds for the Variation of Mean-Square-Continuous Wide-Sense-Stationary Processes, *IEEE Transactions on Information Theory*, Volume 41, Number 3, pages 849–852.
- [25] Fleury, Benard Henri [1996] An Uncertainty Relation for WSS Processes and Its Application to WSSUS Systems, *IEEE Transactions on Communications*, Volume 44, Number 12, pages 1632–1634.
- [26] Fleury, Benard Henri & Peter E. Leuthold [1996] Radiowave Propagation in Mobile Communications: An Overview of European Research, *IEEE Communications Magazine*, Volume 34, pages 70–81.
- [27] Flikkema, P.G.; Johnson, S.G. [1996] A comparison of time- and frequency-domain wireless channel sounding techniques, *Proceedings of SOUTHEASTCON '96* p.488-91.

- [28] Gans, Michael J. [1972] A Power-Spectral Theory of Propagation in the Mobile-Radio Environment, *IEEE Transactions on Vehicular Technology*, Volume VT-21, Number 1, pages 27–38.
- [29] Gel’fand, I. M. & N. Ya. Vilenken [1964] *Generalized Functions*, Volume 4, Academic Press, New York.
- [30] Goldberg, Bernard (editor) [1976] *Communications Channels: Characterization and Behavior*, IEEE Press, New York, 1976.
- [31] Guanghua Deng; Cavers, J.; Ho, P. [1995] A reduced dimensionality propagation model for frequency selective Rayleigh fading channels, *Proceedings IEEE International Conference on Communications ICC ‘95*, Part vol.2 p.1158-62 vol.2
- [32] Hansen, Per Christian [1990] The Discrete Picard Condition for Discrete Ill-Posed Problems, *BIT*, Volume 30, pages 658–672.
- [33] Hansen, Per Christian [1992] Analysis of Discrete Ill-Posed Problems by Means of the L-Curve, *SIAM Review*, Volume 34, Number 4, pages 561–580.
- [34] Hansen, Per Christian [1993] *Regularization Tools: A MATLAB Package for Analysis and Solution of Discrete Ill-Posed Problems*, `netlib@research.att.com`
- [35] Harris, R. M. [1990] Doppler-Multipath Tolerant Voice Communication *AGARD Conference Proceedings 486*, NATO, pages 31-1 to 34-10.
- [36] Hashemi, Homayoun [1979] Simulation of the Urban Radio Propagation Channel, *IEEE Transactions on Vehicular Technology*, Volume VT-28, Number 3, pages 213–225.
- [37] Haykin, S. [1996] *Adaptive Filter Theory*, third edition, Prentice-Hall, Englewood Cliffs, NJ.
- [38] Helleseth, Tor & P. Vijay Kumar [1997] Pseudonoise Sequences, in *The Communications Handbook*, Jerry D. Gibson (editor), CRC Press.

- [39] Hoeher, Peter [1992] A Statistical Discrete-Time Model for the WSSUS Multipath Channel, *IEEE Transactions on Vehicular Technology*, Vol 41, Number 4, pages 461–468.
- [40] Honig, Michael & Melbourne Barton [1996] Baseband Signaling and Pulse Shaping, in *The Mobile Communications Handbook*, Jerry D. Gibson (editor), CRC Press.
- [41] *Jane's Avionics* [1994] Thirteenth Edition, Edited by David Brinkman, International Thomson Publishing Company.
- [42] Katz, Isadore [1963] Radar Reflectivity of the Ocean for Circular Polarization, *IRE Transactions on Antennas and Propagation*, Volume AP-11, pages 451–453.
- [43] Kerr, Donald E. [1951] *Propagation of Short Radio Waves*, McGraw-Hill, New York.
- [44] Kim, John C. & Eugen I. Muehldorf [1995] *Naval Shipboard Communication Systems*, Prentice Hall PTR, Englewood, Cliffs, New Jersey.
- [45] Lam, W.K.; Wan, K.W.; Shen, X.; Austin, J.; Vilar, E. [1994] Wideband sounding of 11.6 GHz trans-horizon channel, *Electronics Letters*, v 30 n 9 Apr 28 1994. p 738-739.
- [46] Lau, W. H.; J. Austin; A. Hewitt; E. Vilar; L. Martin [1991] Analysis of the Time-Variant Structure of Microwave Line-of-Sight Multipath Phenomena, *IEEE Transactions on Communications*, Volume COM-39, Number 6, pages 847–855.
- [47] Long, Maurice W. [1983] *Radar Reflectivity of Land and Sea*, Second Edition, Artech House, Inc.
- [48] Loo, Chun & Norman Secord [1991] Computer Models for Fading Channels with Applications to Digital Transmission, *IEEE Transactions on Vehicular Technology*, Volume 40, Number 4, pages 700–707.
- [49] Lorenz, Rudolf W. [1987] Impact of Frequency-Selective Fading on Digital Land Mobile Radio Communication at Transmission Rates of Several Hundred kbit/s, *IEEE Transactions on Vehicular Technology*, Volume VT-35, Number 3, pages 122–128.

- [50] Luenberger, David G. [1969] *Optimization by Vector Space Methods*, John Wiley & Sons, Inc., New York.
- [51] Lutz, Erich & Ernst Plöchinger [1985] Generating Rice Processes with Given Spectral Properties, *IEEE Transactions on Vehicular Technology*, Volume VT-34, Number 4, pages 178–181.
- [52] Milewski, A. [1983] Periodic Sequences with Optimal Properties for Channel Estimation and Fast Start-Up Equalization, *IBM Journal of Research and Development*, Volume 27, Number 5, pages 426–431.
- [53] Miyagaki, Yoshiya, Norihiko Morinaga, Toshihiko Namekawa [1983] Double Symbol Error Rates of M -ary DPSK in a Satellite-Aircraft Multipath Channel, *IEEE Transactions on Communications*, Volume COM-31, Number 12, pages 1285–1289.
- [54] Mow, Wai Ho [1994] An Upper Bound on the Aperiodic Autocorrelation Function for a Maximal-Length Sequence, *Proceedings of the 1994 International Symposium on Information Theory*, page 75.
- [55] North, Richard C., Roy A. Axford, D. Bryan [1995] *Communications Toolbox Developed at NRaD*, Version 1.0, pre-print.
- [56] North, Richard C. [1996] *Broad Agency Announcement: High-Data-Rate, Line-of-Sight Digital Radio of Mobile Maritime Communications*, N66001-96-X6911, <http://www.nosc.mil/contract/baa/x6911>
- [57] North, R. C., R. A. Axford, D. Bryan [1993] *The Effects of a Multipath Channel on Interference on Coherent M-PSK Digital Communication Systems*, NRaD Technical Report 1636.
- [58] North, R. C., R. A. Axford, J. R. Zeidler [1993] The Performance of Adaptive Equalization for Digital Communication Systems, *Twenty-Seventh Asilomar Conference on Signals, Systems, & Computers*, pages 1548–1553.
- [59] North, Richard C. & James R. Zeidler [1994] Multichannel Adaptive Equalization for Improved Performance in LOS Digital Radio, *1994 IEEE Military Communications Conference*, Fort Monmouth, NJ.

- [60] Newhall, William G.; Kevin Saldanha; Theodore S. Rappaport [1996] Using RF Channel Sounding Measurements to Determine Delay Spread and Path Loss, *RF Design*, January 1996, pages 82–88,
- [61] Parsons, David [1992] *The Mobile Radio Propagation Channel*, Halstaed Press, New York.
- [62] Pritchard, Wilbur [1997] The Calculation of System Temperature for a Microwave Receiver, in *The Communications Handbook*, Jerry D. Gibson (editor), CRC Press.
- [63] Proakis, John G. [1995] *Digital Communications*, Third Edition, McGraw-Hill, New York.
- [64] Proakis, John G. [1996] Channel Equalization, in *The Mobile Communications Handbook*, Jerry D. Gibson (editor), CRC Press.
- [65] Proakis, John G. & Masoud Salehi [1994] *Communication Systems Engineering*, Prentice Hall, New Jersey.
- [66] Putnam, C. R. [1967] *Commutation Properties of Hilbert Space Operators*, Springer-Verlag, New York.
- [67] Röhrs, U. H. & L. P. Linde [1991] HF Channel Sounding with polyphase CAZAC Sequences, *South African Symposium on Communications and Signal Processing COMSIG'91*, IEEE Press.
- [68] Papoulis, A. [1984] *Probability, Random Variables, and Stochastic Processes*, (second edition), McGraw-Hill Book Company, New York
- [69] Popović, B. P. [1995] Class of Binary Sequences for Mobile Channel Estimation, *Electronics Letters*, Volume 31, Number 12, pages 944–945.
- [70] Ryan, Frank J. [1991] Analysis of Electromagnetic Propagation Over Variable Terrain Using the Parabolic Wave Equation, Technical Report 1453, Naval Ocean Systems Center, San Diego, CA 92152-5000.
- [71] Saleh, A. [1981] Frequency-Independent and Frequency-Dependent Non-linear Models of TWT amplifier, *IEEE Transactions on Communications*, Volume COM-29, pages 1715–1720.

- [72] Sandell, Magnus & Ove Edfors [1996] A Comparative Study of Pilot-Based Channel Estimators for Wireless OFDM, preprint.
- [73] Sakrion, D. J. [1968] *Communication Theory: Transmission of Waveforms and Digital Information*, John Wiley & Sons, Inc., New York.
- [74] Sailors, D. B. [1990] Techniques for Estimating the Effects of Man-Made Radio Noise on Distributed Military Systems, *NATO AGARD Conference Proceedings 486*, Rethymno, Crete.
- [75] Sarwate, Dilip V. [1984] An Upper Bound on the Aperiodic Autocorrelation Function for a Maximal-Length Sequence, *IEEE Transactions on Information Theory*, Volume IT-30, Number 4, pages 685–687.
- [76] Sarwate, Dilip V. & Michael B. Pursley [1980] Crosscorrelation Properties of Pseudorandom and Related Sequences, *Proceedings of the IEEE*, Volume 68, Number 5, pages 593–619.
- [77] Schwartz, Mischa; William R. Bennett; Seymour Stein [1966] *Communication Systems and Techniques*, McGraw-Hill, New York.
- [78] Scott, David W. [1992] *Multivariate Density Estimation*, John Wiley & Sons, Inc., New York.
- [79] Senadji, B.; Levy, A.J. [1994] Statistical model for the simulation of time-varying multipath mobile radio propagation channel, *Proceedings of the 1994 IEEE International Conference on Acoustics, Speech and Signal Processing*, Adelaide, Aust, part 6, pages VI-149–VI-152.
- [80] Sklar B. [1988] *Digital Communications*, Prentice-Hall, Englewood Cliffs, NJ.
- [81] Smith, David R. [1996] Channel Models, in *The Mobile Communications Handbook*, Jerry D. Gibson (editor), CRC Press.
- [82] Staley, Thomas L. [1997] *Channel Estimate-Based Performance Prediction for Coherent Linearly Modulated Wireless Communication Systems*, Ph.D. Thesis, UCSD.

- [83] Staley, Thomas L., R. C. North, W. H. Ku, J. R. Zeidler [1997] Performance of Coherent MPSK on Frequency-Selective Slowly-Fading Channels, *IEEE International Conference on Communications*.
- [84] Staley, Thomas L., R. C. North, W. H. Ku, J. R. Zeidler [1997] Probability of Error Evaluation for Multichannel Reception of Coherent MPSK Over Ricean Fading Channels, *IEEE International Conference on Communications*.
- [85] Stein, Seymour [1987] Fading Channel Issues in System Engineering, *IEEE Journal on Selected Areas in Communications*, Volume SAC-5, Number 2, pages 68–89.
- [86] Stüber, G. L.; M. D. Austin; E. Katz [1994] MMSE Sequences for Channel Estimation, *Electronics Letters*, Volume 30, Number 25, pages 2106–2107.
- [87] Tan, Zhenhui & I. F. Blake [1992] Multipath Diversity Reception of Hybrid DS-SFH Spread Spectrum Multiple Access Over Rician Multipath Fading Channels, *IEEE International Conference on Selected Topics in Wireless Communications*, Vancouver, B.C., Canada, pages 433–436.
- [88] Thompson, David J. [1982] Spectrum Estimation and Harmonic Analysis, *Proceedings of the IEEE*, Volume 70, Number 9, pages 1055–1096.
- [89] Vietta, Giorgio M. & Desmond P. Taylor [1994] Maximum Likelihood Sequence Estimation of Uncoded and Coded PSK Signals Transmitted over Rayleigh Flat-Fading Channels, *IEEE International Conference on Communications ICC '94*, Volume 1, pages 1–7.
- [90] Viterbi, Andrew J. [1995] *CDMA: Principles of Spread Spectrum Communication*, Addison-Wesley Publishing Company, Reading Massachusetts.
- [91] Wang, Weizheng [1996] *Communications Toolbox*, The MathWorks, Inc. 24 Prime Park Way, Natick, Mass.
- [92] Widrow, B. & S. D. Stearns [1985] *Adaptive Signal Processing*, Prentice-Hall, Englewood Cliffs, NJ.

- [93] Yacoub, Michel Daoud [1993] *Foundations of Mobile Radio Engineering*, CRC Press, Boca Raton.
- [94] Zha, Hongyuan & Per Christian Hansen [1990] Regularization and the General Gauss-Markov Linear Model, *Mathematics of Computation*, Volume 55, Number 192, pages 613–624.

Appendix A

Generalized Random Processes

Definition A.0.1 [29, pages 242-243] Let (Ω, P, \mathcal{F}) denote a probability space. A generalized random process Φ is a mapping $\Phi : \Omega \rightarrow \mathcal{D}'(\mathbb{R})$ which is weakly \mathcal{F} measurable.

Thus, for each $\omega \in \Omega$, $\Phi(\omega)$ belongs to $\mathcal{D}'(\mathbb{R})$ and, for all $\phi \in \mathcal{D}(\mathbb{R})$, the map $\omega \rightarrow \langle \Phi(\omega), \phi \rangle$ is \mathcal{F} measurable. The means, covariances, and derivatives of generalized random processes also are given as generalized functions.

Definition A.0.2 [29, page 246-247] Let Φ be a generalized random process.

- (a) The mean m of Φ , if it exists, is the functional $m \in \mathcal{D}'(\mathbb{R})$ for which $\langle m, \phi \rangle = E[\langle \Phi, \phi \rangle]$ holds for all $\phi \in \mathcal{D}(\mathbb{R})$.
- (b) The covariance R of Φ , if it exists, is the functional $R \in \mathcal{D}'(\mathbb{R}) \otimes \mathcal{D}'(\mathbb{R})$ given by $\langle R, \phi_1 \otimes \overline{\phi_2} \rangle = E[\langle \Phi, \phi_1 \rangle \langle \Phi, \phi_2 \rangle]$ for all $\phi_1, \phi_2 \in \mathcal{D}(\mathbb{R})$.
- (c) The derivative Φ' is the generalized random process given by $\langle \Phi', \phi \rangle = -\langle \Phi, \phi' \rangle$ for all $\phi \in \mathcal{D}(\mathbb{R})$.

Suppose τ is a real random variable with probability density function $p_\tau(\tau)$. What is $E[\delta(t - \tau)]$?

$$\langle E[\delta(t - \tau), \phi] \rangle = E[\langle \delta(t - \tau), \phi \rangle] = E[\phi(\tau)] = \int_{-\infty}^{\infty} \phi(u) p_\tau(u) du.$$

Thus,

$$E[\delta(t - \tau)] = p_\tau(t).$$

We compute $E[\delta(t - \tau)\delta(t' - \tau)]$ in a similar fashion:

$$\langle E[\delta(t - \tau)\delta(t' - \tau)], \phi \rangle = E[\langle \delta(t - \tau)\delta(t' - \tau), \phi \rangle] = E[\phi(\tau, \tau)].$$

Thus,

$$E[\delta(t - \tau)\delta(t' - \tau)] = p_\tau(t)\delta(t - t').$$

Appendix B

Baseband Error Bounds

This appendix derives error bounds for the slow-fading assumption B-4. Herein $g(t)$ and $p(t)$ are square-root raised cosine pulses corresponding to the receiver and transmitter, respectively. Then

$$\int_{-\infty}^{\infty} g(u) e^{+j2\pi f_n \{t-u\}} p(t-u) du \approx e^{+j2\pi f_n t} \int_{-\infty}^{\infty} g(u) p(t-u) du$$

with a L^2 error bounded by $\sqrt{6f_n T}$. But before grinding through the derivation, introduce the following operators to see what's really going on. For $s \in L^2(\mathbb{R})$,

Lag Operator $L_n s(t) = s(t - \tau_n)$.

Frequency-Shift Operator $F_n s(t) = \exp(+j2\pi f_n t) s(t)$.

Convolution Operator $C_g s(t) = g * s(t)$.

The channel function for the phase-modulation fading is, with a slight abuse of notation, the operator

$$h = \frac{1}{\sqrt{N}} \sum_{n=1}^N a_n F_n L_n.$$

The operator modeling the input to the detector is the convolution operator C_g composed with the channel function:

$$C_g h = \frac{1}{\sqrt{N}} \sum_{n=1}^N a_n C_g F_n L_n.$$

The slow-fading approximation is obtained by commuting the convolution and the frequency shift:

$$C_g h = \frac{1}{\sqrt{N}} \sum_{n=1}^N a_n C_g F_n L_n \approx \frac{1}{\sqrt{N}} \sum_{n=1}^N a_n F_n C_g L_n.$$

There is a huge literature on commuting operators [66] and we are looking for a slick approach to bound this commutant. In the meantime, the following lemma will have to suffice.

Lemma B.0.1 *Assume $g(t)$ and $p(t)$ are square-root raised cosine pulses [40, Eq. 4.18]*

$$\hat{g}(f)^2 = \begin{cases} T & 0 \leq |f| \leq \frac{1-\alpha}{2T} \\ \frac{T}{2} \left\{ 1 + \cos \left(\frac{\pi T}{\alpha} \left\{ |f| - \frac{1-\alpha}{2T} \right\} \right) \right\} & \frac{1-\alpha}{2T} < |f| < \frac{1+\alpha}{2T} \\ 0 & \text{otherwise} \end{cases}.$$

Let $\alpha \in [0, 1]$. If $|\pi f_n T| < 1$, there holds

$$\|C_g F_n p - F_n C_g p\|_2^2 \leq 6 f_n T^2. \quad (\text{B.1})$$

Proof: Set $e_n(t) = \exp(-j2\pi f_n t)$. It is no loss of generality to assume f_n is positive. Then

$$\begin{aligned} \|C_g F_n p - F_n C_g p\|_2 &= \|(g e_n) * p - g * p\|_2 \\ &= \|\widehat{g e_n} \hat{p} - \hat{g} \hat{p}\|_2 \\ &\leq \|\hat{p}\|_\infty \|\widehat{g e_n} - \hat{g}\|_2. \end{aligned}$$

But $\widehat{g e_n}(f) = \hat{g}(f + f_n)$. Whenever \hat{g} is flat, we get excellent cancellation. In fact, when $\alpha = 0$, we get the immediate bound

$$\|\widehat{g e_n} - \hat{g}\|_2^2 = 2T f_n.$$

When $\alpha > 0$, a plot of the integrand $\hat{g}(f + f_n) - \hat{g}(f)$ reveals the difference may be bounded by the Mean-Value Theorem — provided the difference does not straddle any of the “joints” of \hat{g} . That is,

$$\hat{g}(f + f_n) - \hat{g}(f) = \hat{g}'(\zeta) f_n$$

for some $\zeta \in f + [0, f_n]$ provided \hat{g} is differentiable on that interval. Summing over those frequencies where this applies gives the upper bound

$$\begin{aligned} 2 \int_{\frac{1-\alpha}{2T}+f_n}^{\frac{1+\alpha}{2T}-f_n} |\hat{g}(f+f_n) - \hat{g}(f)|^2 df &= 2 \int_{\frac{1-\alpha}{2T}+f_n}^{\frac{1+\alpha}{2T}-f_n} |\hat{g}'(\zeta(f)) f_n|^2 df \\ &\leq 2 \frac{\pi^2 T^3 f_n^2}{\alpha^2 8} \frac{1}{2T} \max \left\{ 0, \frac{\alpha}{T} - 2f_n \right\} \\ &\leq \frac{(\pi f_n T)^2}{4\alpha} \chi(\alpha - 2f_n T > 0) \end{aligned}$$

It remains to bound the contributions from the little regions where the Mean-Value Theorem does not apply. There are the two end-point regions whose contribution are bounded by:

$$2f_n |\hat{g}((1+\alpha)/(2T) - f_n)|^2 = f_n T \{1 - \cos(\pi f_n T)\} < 5f_n^3 T^3.$$

The last inequality requires $|\pi f_n T| < 1$. For $0 < \alpha < 1$, there are also contributions from the two interior regions at the break points which are bounded by:

$$2f_n |\sqrt{T} - \hat{g}((1-\alpha)/(2T) + f_n)|^2 = f_n T \{1 - \cos(\pi f_n T/\alpha)\} < 5f_n^3 T^3/\alpha.$$

The last inequality requires $|\pi f_n T| < 1$. Gathering the results:

$\alpha = 0$:

$$\|(ge_n) * p - g * p\|_2^2 \leq \|\hat{p}\|_\infty^2 \times 2f_n T = 2f_n T^2.$$

$\alpha = 1$: Assuming $|\pi f_n T| < 1$:

$$\begin{aligned} \|(ge_n) * p - g * p\|_2^2 &\leq \|\hat{p}\|_\infty^2 \{5f_n^3 T^3 + \pi^2 f_n^2 T^2/4\} \\ &\leq f_n^2 T^3 \{5f_n T + 3\} \\ &\leq 6f_n^2 T^3 \end{aligned}$$

$0 < \alpha < 1$: Assuming $|\pi f_n T| < 1$

$$\begin{aligned} \|(ge_n) * p - g * p\|_2^2 &\leq \|\hat{p}\|_\infty^2 \{5f_n^3 T^3/\alpha + 5f_n^3 T^3 + \pi^2 f_n^2 T^2/(4\alpha)\} \\ &\leq f_n^2 T^3 \{5f_n T/\alpha + 5f_n T + 3/\alpha\} \\ &\leq f_n^2 T^3 \{5/2 + 5/2 + 3/\alpha\} \\ &\leq f_n^2 T^3 \{5 + 3/\alpha\}. \end{aligned}$$

This bound agrees with the bound for $\alpha = 1$. To get the same order matching $\alpha = 0$, we use

$$\begin{aligned} f_n^2 T^3 \{5 + 3/\alpha\} &= f_n T^2 \{5 f_n T + 3 f_n T / \alpha\} \\ &\leq f_n T^2 \{5/2 + 3/2\} \\ &\leq 4 f_n T^2 \end{aligned}$$

Thus, the bound reported in this lemma is tight for small α 's but becomes way too large for α 's near 1. \square

Appendix C

Gauss-Markov Theorems

The following classical theorems provide a statistical framework for channel estimation and a context for the speedy understanding of conventional sequence processing.

Theorem C.0.1 (Gauss-Markov) [50, page 86] *Assume a linear system of the form*

$$\mathbf{y} = A\mathbf{x} + \mathbf{v},$$

where A is a known matrix, \mathbf{x} is an unknown but non-random vector, and the noise vector \mathbf{v} has first and second-order expectations:

GM-1 $E[\mathbf{v}] = 0,$

GM-2 $E[\mathbf{v}\mathbf{v}^H] = R_{\mathbf{v}\mathbf{v}}.$

A linear estimate of \mathbf{x} has the form $\hat{\mathbf{x}} = B\mathbf{y}$ for some matrix B . A linear estimate $\hat{\mathbf{x}}$ which is unbiased for all \mathbf{y} 's forces $BA = I$. The linear minimum-variance unbiased estimate (also called the Gauss-Markov estimate) is the linear estimate \mathbf{x}_{GM} which solves

$$\min\{E[\|\hat{\mathbf{x}} - \mathbf{x}\|_2^2] : BA = I\}.$$

It is given by

$$\mathbf{x}_{\text{GM}} = (A^H R_{\mathbf{v}\mathbf{v}}^{-1} A)^{-1} A^H R_{\mathbf{v}\mathbf{v}}^{-1} \mathbf{y}$$

and has error covariance

$$E[(\mathbf{x}_{\text{GM}} - \mathbf{x})(\mathbf{x}_{\text{GM}} - \mathbf{x})^H] = (A^H R_{\mathbf{v}\mathbf{v}}^{-1} A)^{-1}.$$

The Gauss-Markov estimate cannot adapt to varying noise levels nor can it adjust for those matrices A which are ill-conditioned. By trading bias for variance, a class of regularized estimators can be obtained which compensate for these deficiencies. There is an additional price to pay. For our case, it is the requirement that we know the covariance of the channel.

Theorem C.0.2 (Minimum-Variance) [50, page 87–90] *Assume a linear system of the form*

$$\mathbf{y} = A\mathbf{x} + \mathbf{v},$$

where A is a known matrix, \mathbf{x} is an unknown random vector uncorrelated with the random noise vector \mathbf{v} . The expectations are as follows:

MV-1 $E[\mathbf{v}] = 0,$

MV-2 $E[\mathbf{v}\mathbf{v}^H] = R_{\mathbf{v}\mathbf{v}},$

MV-3 $E[\mathbf{x}\mathbf{x}^H] = R_{\mathbf{x}\mathbf{x}},$

MV-4 $E[\mathbf{x}\mathbf{v}^H] = 0.$

Then the linear estimate \mathbf{x}_{MV} which solves $\min\{E[\|\hat{\mathbf{x}} - \mathbf{x}\|_2^2]\}$ is given by

$$\mathbf{x}_{\text{MV}} = (A^H R_{\mathbf{v}\mathbf{v}}^{-1} A + R_{\mathbf{x}\mathbf{x}}^{-1})^{-1} A^H R_{\mathbf{v}\mathbf{v}}^{-1} \mathbf{y}$$

with error covariance

$$E[(\mathbf{x}_{\text{MV}} - \mathbf{x})(\mathbf{x}_{\text{MV}} - \mathbf{x})^H] = (A^H R_{\mathbf{v}\mathbf{v}}^{-1} A + R_{\mathbf{x}\mathbf{x}}^{-1})^{-1}.$$

Appendix D

Receiver Noise Computations

This appendix collects the covariance computations for the receiver noise. We assume the baseband modeling assumptions B-1, B-2, B-3, B-4, and B-5 from Chapter 2 are in force. Recall the detector input $y(t)$ then has the form

$$y(t) = p_R * e(t) + p_R * \eta(t),$$

where $p_R(t)$ is the receiver's matched filter and $\{\eta(t)\}$ is the IF noise. This noise consists of the thermal noise of the system and the received RF noise. Typically, $\{\eta(t)\}$ is a complex-valued, zero-mean, Gaussian random process with a spectrum shaped by the IF filter. However, as long as we look at $\{\eta(t)\}$ through the receiver filter, it is no loss of generality to model $\{\eta(t)\}$ as Gaussian white noise [68]:

$$R_{\eta\eta}(t_1, t_2) = \sigma_\eta^2 \delta(t_1 - t_2).$$

It will be handy recall the next result:

Lemma D.0.2 [68, page 237] *If $\nu(t) = p_R * \eta(t)$ then*

$$R_{\nu\nu}(t_1, t_2) = p_R \otimes \overline{p_R} * R_{\eta\eta}(t_1, t_2).$$

Example D.0.1 *Suppose p_R is the square-root raised cosine filter ($p_R \star p_R = x_{RC}$). If $\{\eta(t)\}$ is white noise then $\{\nu(t)\}$ is WSS with covariance*

$$R_{\nu\nu}(t_1, t_2) = \sigma_\eta^2 p_R \star p_R(t_1 - t_2) = \sigma_\eta^2 x_{RC}(t_1 - t_2).$$

The Gauss-Markov Theorems of Chapter C make heavy use of the noise covariance matrix $Q = [R_{\nu\nu}(t_m, t_n)]$. Example D.0.1 shows that once-per-symbol sampling gives

$$Q = [R_{\nu\nu}(mT, nT)] = [x_{\text{RC}}((m - n)T)] = \sigma_\eta^2 I.$$

Because the noise covariance is used to form Q at the sampling instants, synchronized sampling has a profound effect on this matrix. So what are the effects of the non-synchronous sampling? The next result determines the covariance of the noise $\{\nu(t)\}$ when the sampling instants are subject to jitter.

Lemma D.0.3 *Suppose the sample times $t_m = m\tilde{T}$ are jittered:*

$$\nu_m = p_R * \eta(t_m + \Delta t_m),$$

where $\{\Delta t_m\}$ is a real-valued random process such that

J-1 *The Δt_m 's are IID.*

J-2 *The Δt_m 's are zero mean: $E[\Delta t_m] = 0$.*

J-3 *The distribution p_Δ is symmetric: $p_\Delta(t) = p_\Delta(-t)$.*

Then

$$R_{\nu\nu}(m_1, m_2) = \begin{cases} p_\Delta \otimes p_\Delta * p_R \otimes p_R * R_{\eta\eta}(t_{m_1}, t_{m_2}) & m_1 \neq m_2 \\ p_\Delta \otimes \delta * p_R \otimes p_R * R_{\eta\eta}(t_{m_1}, t_{m_2}) & m_1 = m_2 \end{cases}.$$

Example D.0.2 *Suppose p_R is the square-root raised cosine filter ($p_R * p_R = x_{\text{RC}}$) Suppose $\{\eta(t)\}$ is white noise. Then jittered sampling gives*

$$R_{\nu\nu}(m_1, m_2) = \sigma_\eta^2 p_\Delta * p_\Delta * x_{\text{RC}}(t_{m_1} - t_{m_2}).$$

Thus, jittered sampling smears the noise covariance by the distribution of the jitters.